FABRICATION AND CHARACTERISATION OF HIGH TEMPERATURE SUPERCONDUCTING BULK YBCO

STEPHEN JOHN MANTON

Doctor of Philosophy

Faculty of Mechanical Engineering
Institute of Cryogenics

Submitted September 2000

UNIVERSITY OF SOUTHAMPTON

ABSTRACT

FACULTY OF MECHANICAL ENGINEERING

INSTITUTE OF CRYOGENICS

Doctor of Philosophy

FABRICATION AND CHARACTERISATION OF HIGH TEMPERATURE SUPERCONDUCTING BULK YBCO.

By Stephen John Manton

The processing environment required for the manufacture of large, mono-domain specimens of bulk YBCO via the seeded melt textured growth technique has been developed. As a result of this it has been possible to examine in detail the growth morphology and crystal structure of samples prepared in this way.

A novel powder preparation technique involving the use of a high temperature plasma spray was employed to produce homogeneous YBCO powder suitable for melt texturing. It was found that the well mixed, un-reacted starting powder would produce material with a fine distribution of secondary phase inclusions. Melt textured samples were produced from this powder using differing thermal cycles in an attempt to ascertain the optimum conditions for producing the desired microstructure.

In an attempt to improve the flux pinning properties of single grain Y123 undoped and samples doped with lithium underwent irradiation with thermal neutrons. Magnetic measurements were then used to illustrate the enhancement due to this process.

In order to improve the electrical properties of Sm123 it is desirable to be able to control the amount of Sm/Ba substitution. Already grown samples of Sm123 were processed in a reduced oxygen atmosphere in a manner that was shown to control the degree of Sm/Ba substitution.

For many potential application large, shaped samples of YBCO are required. Due to the properties of the material this is very difficult. Using a liquid phase infiltration method single grain samples of YBCO have been re-joined without the introduction of a grain boundary.

R(T) and I-V dependencies close to Tc and in zero magnetic field were obtained from single grain samples of YBCO in the nV region. For $T < T_c$, the lower parts of the resulting curves were interpreted in the frame of the J-M model of current induced unbinding of thermally generated vortex/anti-vortex pairs, allowing us to obtain the temperature dependence of the characteristic current, $I_{c1}(T)$, close to T_c. In addition, the current value for a given temperature above which the J-M model becomes inadequate has been measured and interpreted.

Direct transport measurements for melt textured YBCO in an applied magnetic field have been taken. The angular dependence of the superconducting properties have been discussed in the context of sample morphology.

Contents

Chapter 10: Conclusion

Acknowledgement

I would like to thank both Dr. Y. Yang and Prof. C. Beduz for their patience and direction. I would also like to thank Mr. M. Webb for his technical assistance and can do attitude, and Markus, Stuart and Javier for being ideal colleagues.

My main debt of gratitude goes to my parents and Liz, without whom I would never have completed my study.

Chapter 1 : Introduction to the Superconducting Phenomenon.

1.1 Historical Background

In 1911 the successful liquefaction of helium[1] allowed Kamerlingh Onnes to investigate the resistive properties of elements at temperatures lower than ever previously possible. Famously, when he came to study mercury he observed an unexpected sharp transition from resistive behaviour to a state with no measurable d.c. resistance at all, as can be seen in Fig 1.1[2]. Rather than obeying Bloch's Law for the temperature dependence of resistivity, Onnes observed an entirely new thermodynamic state which exists in mercury at temperatures below 4.2K, which was later named superconductivity. The temperature at which the transition from a resistive to a superconducting state is known as the critical temperature (T_c). Following this, two other linked critical parameters were defined; the critical field (H_c) and the critical current (J_c).

The revolutionary nature of this discovery fuelled researchers to look for other materials which displayed this superconducting state. It was found that a number of metallic elements displayed a superconducting transition at temperatures ranging from 0.0154 K (the lowest T_c for an element corresponding to tungsten) to 9.25K (the highest T_c for an element measured in niobium). However, when engineers and physicists began to look for possible applications for these materials they found that despite the ideal mechanical properties of the elemental superconductors, the electrical properties were not suitable. The problem was not the low T_c's of these substances but rather the limits imposed by the low J_c's and H_c's, i.e. these materials could not remain superconducting when carrying modest currents or in the presence of small magnetic fields. Because of this, attention became focussed on finding alloys with superior superconducting properties, which resulted in the discovery of type II superconductivity and of the A_3B family of materials such as Nb_3Sn, Nb_3Ga and Nb_3Ge, the latter of

which has a T_c of 23.2K, which remained the highest T_c until the discovery of high temperature superconductors.

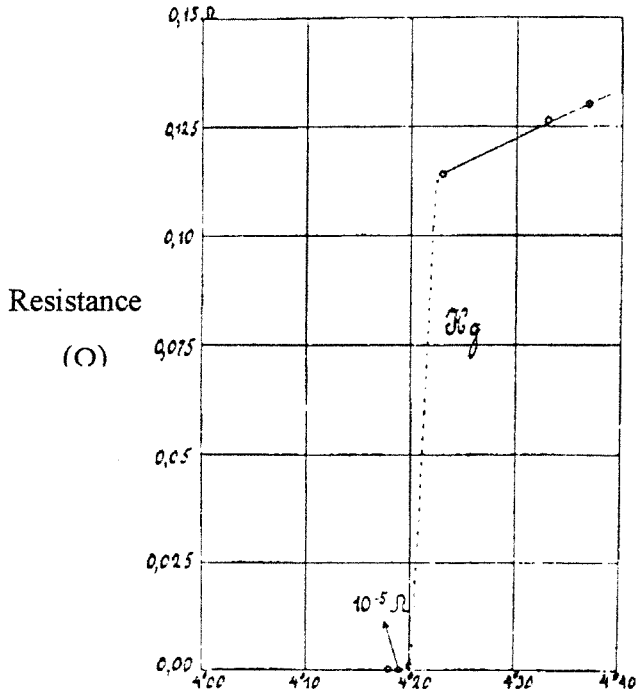

Fig.1.1 Temperature dependence of mercury, H. K. Onnes[2]

1.2 Type I Superconductivity : Zero Resistance and the Meissner State.

Measurements have shown that the resistance in the superconducting state is not just small but is in fact as close to zero as detectable. Persistent current measurements for superconducting rings have shown no decrease in current over a timescale of years, whilst nuclear resonance has been used to establish a lower bound for the characteristic decay time of 10^5 years for the field generated by a circulating current. As can bee seen in Fig 1.1, the transition from finite to zero resistance is very sharp. This true of most superconductors and indicates that what is observed is a phase transition in which electrons condense into an ordered, superconducting state. This phase transition has

been demonstrated experimentally by the observation of a discontinuity in the specific heat seen at T_c. The microscopic theories for low T_c superconductivity describe how electrons form pairs, known as Cooper pairs, when the material is cooled to below T_c. It is this phenomenon that allows the resistance to fall to zero.

Meissner and Ochsenfeld[3] were the first to observe perfect diamagnetism in a superconductor. Diamagnetism is the condition where the magnetisation of the sample is in perfect opposition to the applied field, as is written in eq 1.1.

$$H = -M \qquad \text{eq 1.1}$$

This condition cannot be explained by perfect conductivity and is what differentiates superconductivity from perfect conductivity. Fig 1.2 illustrates the behaviour of a perfect conductor and a superconductor under zero field cooled (ZFC) and field cooled (FC) conditions. ZFC relates to the superconductor being cooled through T_c with no applied field whilst FC corresponds to the superconductor being cooled through T_c in the presence of an applied field. It is apparent that in the ZFC instance the behaviour of the two is identical[4], with the electromagnetic flux remaining excluded from the bulk as long as the applied field remains lower than H_c. However, in the field FC situation the superconductor actually expels the field from within the bulk, a phenomena not mirrored by the perfect conductor which traps the field, as can be seen when the field is switched off. The existence of the reversible Meissner effect implies that H_c, the critical field at which flux will penetrate the superconductor and superconductivity is destroyed, is related to the free energy difference between the normal and the superconducting state, or more precisely the condensation energy of the cooper pairs.

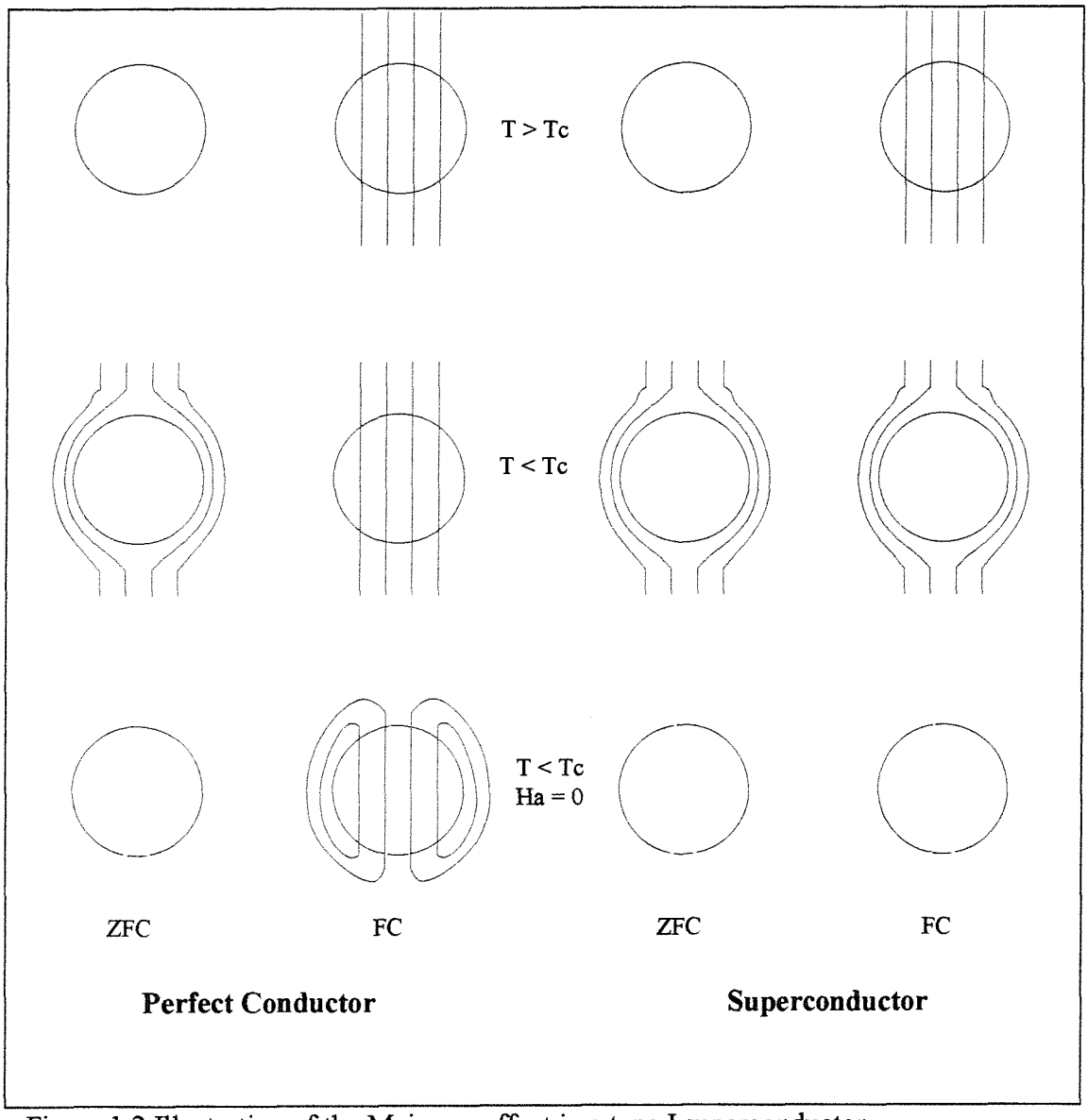

Figure 1.2 Illustration of the Meissner effect in a type I superconductor.

1.3 Introduction to Type II Superconductors.

In the previous section elemental superconductors were described. With the exception of Nb, these superconductors display properties characterised as type I superconductors. They exhibit zero resistance at temperatures below T_c and fields

below H_c. Until H_c is reached all electromagnetic flux is excluded from the bulk, but once this limit is exceeded flux penetrates into the material and superconductivity is destroyed.

As a by-product of the effort to produce superconductors with critical fields and currents suitable for applications a second family of low temperature (LTC) superconductors, type II superconductors, were discovered. These materials, of which niobium-3-tin (Nb_3Sn) is the most famous, display radically different properties when compared to the elemental type I superconductors. Not only do these materials carry far higher currents but they are also able to remain superconducting in the presence of much larger magnetic fields. The development of substances witch display the same beneficial mechanical properties as type I superconductors whilst having the capacity to carry large currents and produce large fields allowed the production of useful superconducting devices such as high field magnets. However, these devices still needed to be cooled by expensive liquid helium, a fact that restricted the industrial interest in superconductivity.

This remained the situation until 1986, when Muller and Bednorz[5] discovered the first rare earth barium cuprate ceramic superconductor. Although this oxide compound (La-Ba-Cu-O) displayed a Tc of only around 35K, it led quickly to the discovery by Chu et al[6] of superconductivity in Y-Ba-Cu-O at temperatures in excess of 90 K. This exceeded the critical 77 K boundary, which is the temperature at which devices may be cooled by low cost liquid nitrogen. Soon after this, other oxide compounds were discovered with T_c's in excess of 125 K, suggesting the limit of superconductivity has yet to be reached. This class of superconductors has been classified as High T_c (HTC) in order to differentiate them from other type II superconductors.

1.4 Research Objectives

Primarily due to T_c being greater than the boiling point of liquid nitrogen, rare earth 123 (RE123) materials such as YBCO show great promise as candidates for utilising the superconducting phenomenon in real applications. Thus, in this work, the conditions necessary for the production of RE123 material of high quality are investigated and the characteristics of the material examined.

The small coherence length found in RE123 material results in any large angle grain boundaries or weakly linked regions having a disastrous effect on the superconducting properties of the material as a whole. With this in mind the procedure for producing large samples of single grain material of good quality using the seeded melt textured growth technique is presented and discussed (chapter 3). As an alternative/enhancement to producing large samples of single domain material, chapter 7 presents an infiltration technique used to join already grown monoliths of Y123 material with a composite formed of Er/Y123, avoiding the creation of a grain boundary.

A further consideration when producing RE123 materials intended for any application is that the superconducting properties are highly dependant on the microstructure/composition of the material, hence control of these factors is essential. Chapters 4, 5 and 6 present various methods for modifying and controlling the microstructure/composition of melt grown RE123 material with the intent of enhancing the flux pinning within the bulk. In chapter 4 a novel powder preparation technique is used to improve the topology/distribution of Y211 inclusions (which act as pinning centres) within the Y123 bulk. Chapter 5 demonstrates how artificial defects introduced via neutron irradiation act as effective pinning sites and also shows that the use of Li as dopant does not increase the benefit gained from the irradiation process. Presented in chapter 7 is a technique for post processing already grown melt textured Sm123 material in a reduced oxygen atmosphere with the intention of reducing the

amount of Sm/Ba substitution which takes place on the Ba site within the crystal structure. Controlling the degree of substitution within Sm123 and Nd123 materials allows the T_c of the materials to be enhanced, making their high field pinning properties exploitable.

Both chapters 8 and 9 focus on the current transport properties of YBCO. From a theoretical and an engineering design perspective it is essential the current carrying characteristics of high temperature superconductors are fully understood. Chapter 8 examines in detail the IV characteristics of a single grain sample of melt textured YBCO close to T_c and with no applied magnetic field, demonstrating a good match with the Jensen-Minnhagen model. The objective in chapter 9 is to present and interpret the dependence of the IV characteristics of a single grain sample of Y123 on the angle of the applied magnetic field at an operating temperature of 77K.

1.5 Fundamental Theory

Unlike type I superconductors, type II materials do not display perfect diamagnetism at all fields until superconductivity is destroyed. At a certain thermodynamically defined field (H_{c1}) it becomes energetically favourable for individual quanta of electromagnetic flux to penetrate into the superconductor. Superconductivity may be sustained in this way up to fields much larger than the thermodynamic critical field (H_c), up to a field given as H_{c2}. This may bee seen in Fig 1.3 where equilibrium magnetisation curves for type I and type II superconductors are illustrated.

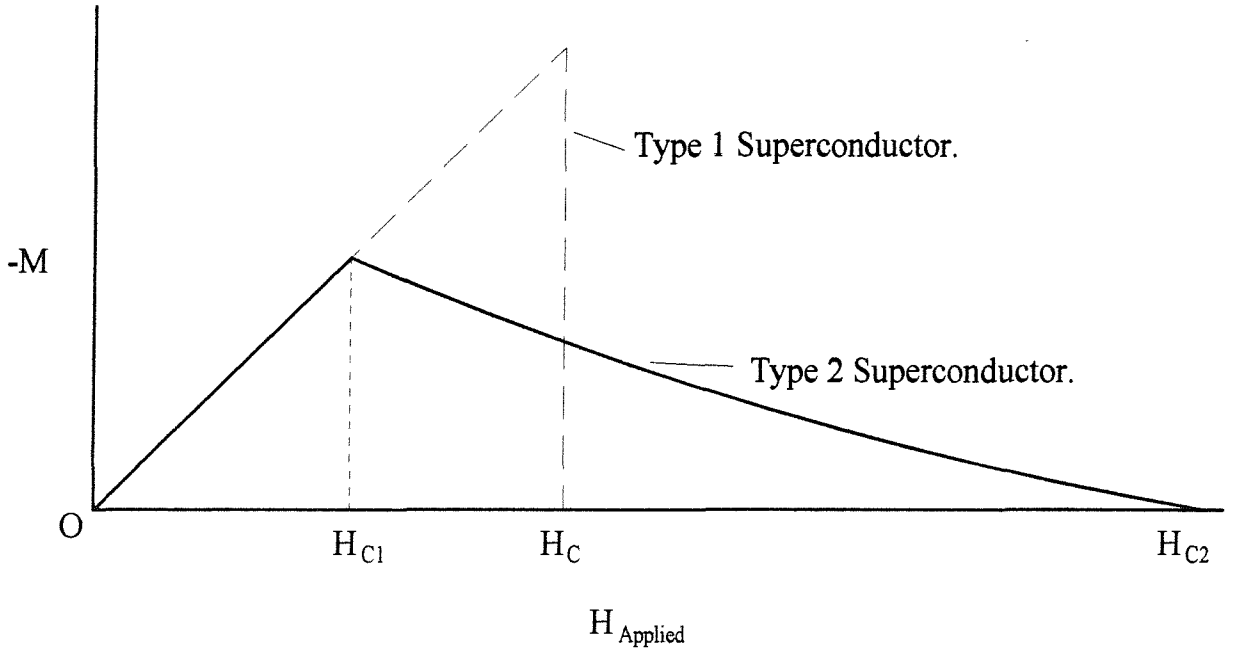

Fig 1.3 Equilibrium Magnetisation Curve for Type I and II Superconductors

In order to further understand the properties of type I and II superconductors it is necessary to look at the underlying physics.

There are two important lengths associated with superconductors. The first is the coherence length, ξ. This is the minimum distance over which it is permissible for the superconducting wave function, φ, to change. The other important length is the penetration depth, λ. This represents how far into the bulk of the superconductor a magnetic field will penetrate. There seems little value in deriving these quantities here as detailed derivations are easily accessible in many texts[7, 8, 9]. More useful is the knowledge that whether a material is type I or type II is dependent on the relationship between these two quantities. The Ginzburg-Landau parameter, κ, is defined as:

$$\kappa = \left(\frac{\lambda}{\xi}\right) \qquad \text{eq 1.2}$$

Now, if $\kappa < 1/\sqrt{2}$ the material is type I, and conversely, if $\kappa > 1/\sqrt{2}$ then the superconductor is type II. From the London equation, which is a solution of the Ginzburg-Landau equation, λ may be defined as:

$$\lambda = \left(\frac{m'}{\mu_0 n_s e'^2} \right) \qquad \text{eq 1.3}$$

Where m′ is the mass of two electrons (the Cooper pair), n_s is the number of cooper pairs (the number of electrons divided by two) and e′ is the charge of a Cooper pair (2e). It has been found that n_s is small in HTSC's, therefore λ is large. The coherence length may be given as:

$$\xi_0 = \frac{0.18\hbar v_f}{k_B T_c} \qquad \text{eq 1.4}$$

where v_f is the fermi velocity and k_b is the Boltzman constant. Obviously T_c is high for a HTSC and also v_f is small, so it follows that ξ is small.

Why should a short coherence length combined with a long penetration depth lead to the flux penetration and high field tolerances associated with type II superconductors? The surface energy associated with a normal-superconducting boundary is give by:

$$\alpha_s = \frac{1}{2\mu_0}\left(\underline{B_c}^2 \xi_0 - \underline{B_a}^2 \lambda\right) \qquad \text{eq 1.5}$$

$$= \frac{1}{2}\mu_0(\underline{H_c}^2 \xi_0 - \underline{H_a}^2 \lambda) \qquad \text{eq 1.6}$$

So for a type II superconductor, where λ is larger than ξ, it is energetically favourable to create new surfaces whilst H_a is still below H_c. The energy will be zero when H_a is equal to H_{c1} because up to this point it has not been energetically favourable to have more normal-superconducting boundaries. Therefore:

$$\underline{H_{c1}} = \sqrt{\frac{\xi}{\lambda}}\underline{H_c} \qquad \text{eq 1.7}$$

Once H_{c1} has been exceeded the superconductor enters Shubnikov phase, mixed state or vortex state. It is in this state that individual flux quanta penetrate the superconductor and form a triangular vortex lattice. This ordered structure is formed in order to minimise energy and is called the Abrikosov[10,11] lattice, with length of side given by:

$$a_0 = 1.075\sqrt{\frac{\phi_0}{B}} \qquad \text{eq 1.8}$$

where ϕ_0 is the flux quantum. H_{c2} may also be found using the Ginzburg-Landau theory and is given by:

$$H_{c2} = \sqrt{2}\frac{\lambda}{\xi}H_c \qquad \text{eq 1.9}$$

The three critical parameters of a superconductor, if exceeded, result in the collapse of the superconducting state. The relationship between these parameters is shown schematically in fig 1.4.

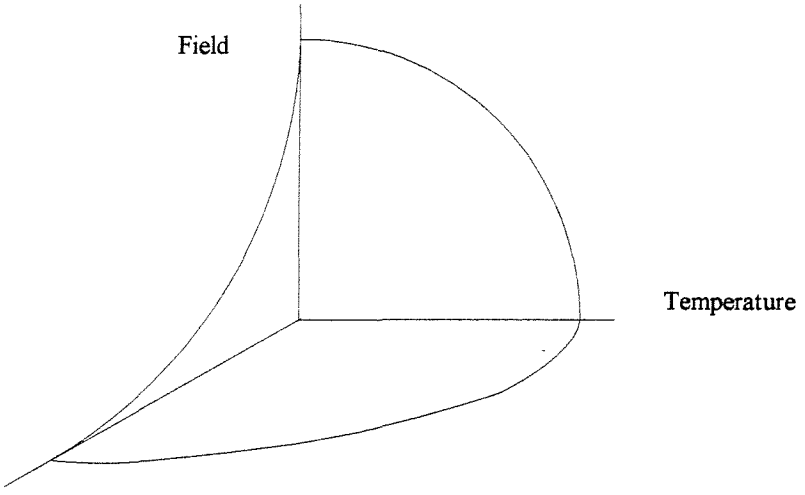

Fig 1.4 Schematic of relationship between H_c, T_c and J_c.

The dependence of the critical field upon the temperature may be expressed in the Tuyn's Law[12]:

$$\mathbf{H_c=H_0(1-(T/T_c)^2)} \qquad \text{eq 1.10}$$

1.6 The Critical State Model

A flux line in a superconductor is subject to a Lorentz force:

$$\mathbf{F}_l = \mathbf{J} \times \mathbf{B} \qquad \text{eq 1.11}$$

If uninhibited, the Lorentz force would cause motion of the flux lines. In order for the flux lines to be moved work would be done and so resistive losses would result. In reality, the flux lines are held in place by a pinning potential that opposes the Lorentz force. As long as the pinning force is stronger than the Lorentz force there will be no flux motion and therefore no losses. F_p, the pinning force, is dependent on the structure of the sample and may take contributions from features such as, non-superconducting 211 inclusions, twin planes, oxygen deficient regions and stacking faults.

The Bean model, proposed by Charles Bean[13, 14], describes a critical, non-equilibrium state which is supported by the pinning force and the critical current. Bean postulates that the current inside a superconductor is either the maximum value possible, J_c, or zero. This creates a field gradient $\partial \mathbf{B}/\partial x$, which the Lorentz force tries to reduce and hence restore equilibrium. Fig 1.5 shows field profiles for an infinite slab geometry at various applied fields.

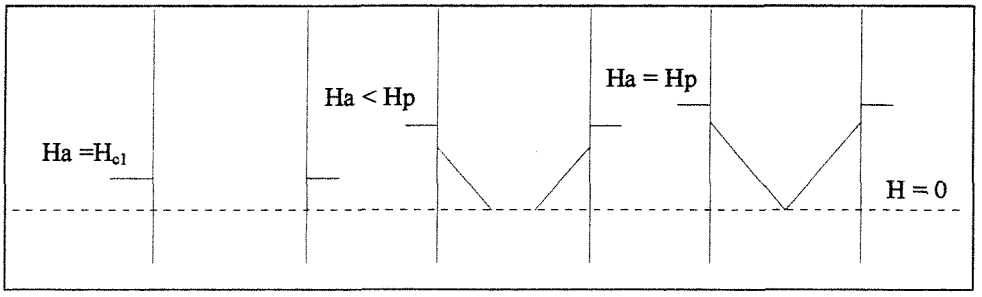

Fig 1.5 Field in an infinite slab by the Bean model.

This illustrates how the Meisner state is retained until H_{c1} is reached. This is then followed by partial penetration where $H_a < H_p$, and then full penetration at H_p. At $2H_p$ the field inside the superconducting slab will reach $\mu_0 H_p$, which is the maximum field the pinning force is able to retain once the applied field has been reduced to zero.

Bean assumes that $\mathbf{F_p}$ is proportional to $\mathbf{B}$;

$$\mathbf{F_p} = c\mathbf{B} \qquad \text{eq1.12}$$

where c is a constant. The critical current can then be defined as when:

$$\mathbf{F_l} = -\mathbf{F_p} \qquad \text{eq 1.13}$$

So by combining eq 1.12 and eq 1.13 we get:

$$\mathbf{J_c} = \mathbf{F_p}/\mathbf{B} = c \qquad \text{eq 1.14}$$

Using the one dimensional Maxwell equation we may obtain an expression for the field gradient:

$$\partial B_z/\partial x = -\mu_0 J_c \qquad \text{eq 1.15}$$

This can be integrated to an expression for the field inside the slab:

$$B_z = -(\mu_0 J_c)x + B_{z0} \qquad \text{eq 1.16}$$

Thus it can be said that the angle α (as shown in fig 1.6) is given by:

$$\tan \alpha = \mu_0 J_c \qquad \text{eq 1.17}$$

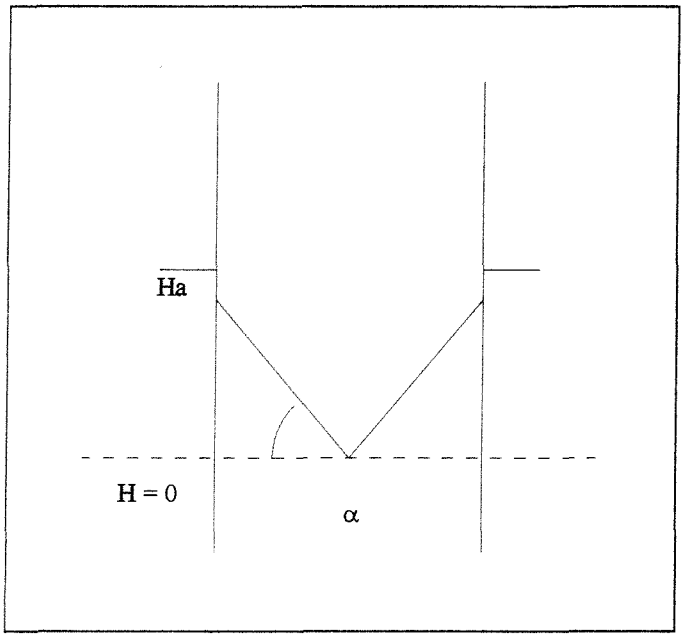

Fig 1.6 Angle α of the field gradient.

Kim et al[15] take the critical state model one step further by incorporating the dependence of J_c on the magnitude of the magnetic field.

$$J_c = J_{co} B_o / (B_o + B) \qquad \text{eq 1.18}$$

These changes result in a field profile which takes the form;

$$B_z = \theta x^{1/2} + \gamma \qquad \text{eq 1.19}$$

where θ and γ are constants.

Due to the anisotropic nature of YBCO, the critical current value in the ab plane is larger than that in the c direction. Fortunately, the Bean model is able to take account

of this rather inconvenient property. If we view from above the field profile of an infinite square rod which has no anisotropy and with maximum field trapped inside it in a direction perpendicular to the page, we will see the picture illustrated in Fig 1.7. The cross represents the places in which the contributions from two of the surfaces meet, and where all four meet in the centre. Because the angle α is the same perpendicular to all four of the surfaces, the maximum field will be found at a point in the centre. However, if the c axis is in a horizontal direction as in Fig 1.8, then α is smaller in this direction than in the vertical direction. As a result, the maximum field is no longer a point but a line perpendicular to the c axis.

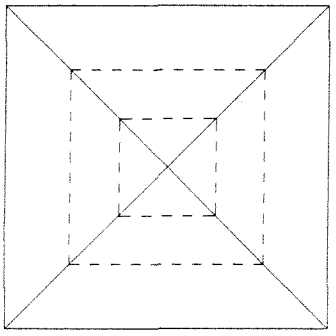

Fig 1.7 Isotropic Bean model.

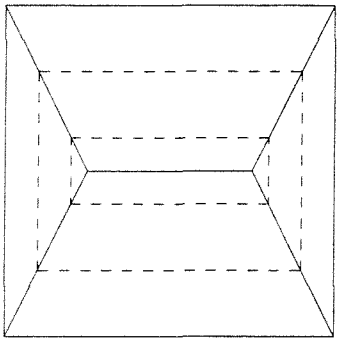

Fig 1.8 Anisotropic Bean model.

This may be more clearly understood by looking at the equations. Let us consider a rectangle of side length l and t. From eq 1.16 we can write:

$$B_t = -(\mu_o J_{ct})x + B_o \qquad \text{eq 1.19}$$

and

$$B_l = -(\mu_o J_{cl})y + B_o \qquad \text{eq 1.20}$$

At the points marked A on Fig 1.9, B_t is equal to B_l. From this we can say that:

$$J_{ct} \times k = J_{cl} \times t/2 \qquad \text{eq 1.21}$$

and so it follows that:

$$k = (J_{cl}/J_{ct}) \times (t/2) \qquad \text{eq 1.22}$$

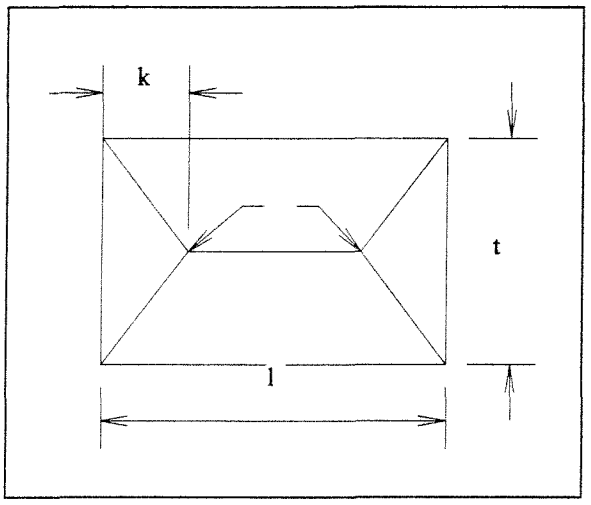

Fig 1.9

This is only true for the case when $J_{cl}/J_{ct} < l/t$. The other two cases, when the two quantities are equal and when $l/t < J_{cl}/J_{ct}$, are shown in Fig 1.11 and Fig 1.10 respectively. In this model we have assumed full penetration and ignored edge effects to avoid over complication.

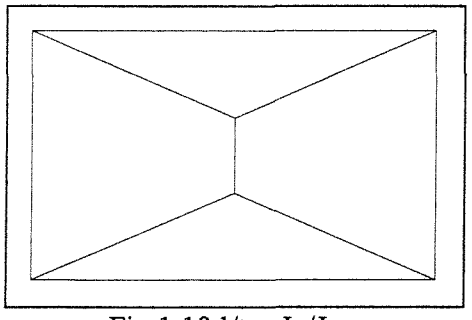

Fig 1.10 $l/t < J_{cl}/J_{ct}$

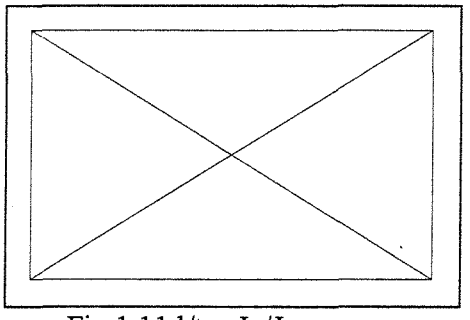

Fig 1.11 $l/t = J_{cl}/J_{ct}$

1.7 Flux Creep.

As previously stated, the critical state is a state of non-equilibrium. Flux creep is the process by which thermally activated flux hopping, aided by the Lorentz force, tries to re-establish equilibrium by reducing the field gradient to zero[16,17]. Fig 1.13 shows how the flux gradient relaxes over time when the temperature is non-zero, for an external field and for a trapped field. Flux creep is the mechanism responsible for the relaxation of magnetisation, making it necessary to 're-charge' or 'pump' HTSC magnets as time passes. This is a particularly undesirable feature of HTSC magnets, making them a less proposition for many applications.

The rate of flux creep is given by;

$$\frac{d\phi}{dt} = \phi_o a_o \nu_o \exp\left(\frac{-U}{k_B T}\right) \qquad \text{eq 1.23}$$

where ϕ_o is the flux quantum, a_o is the vortex lattice spacing, ν_o is the attempt frequency and U is the pinning energy. This rate is strongly temperature dependent, so for HTSC's at liquid nitrogen temperatures it is especially important that U, the pinning potential, be high.

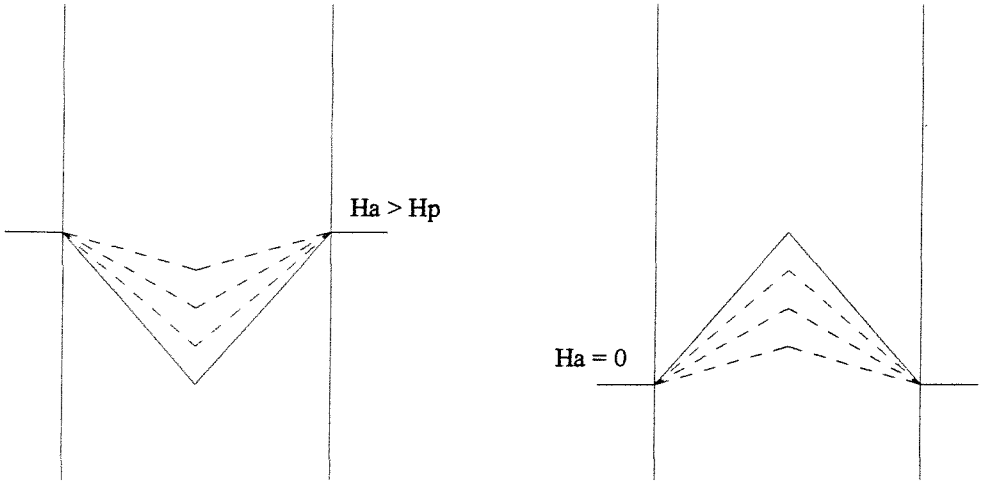

Fig 1.12 Field Relaxation Due to Flux Creep.

A method of reducing the effects of flux creep is to 'freeze' the flux inside by lowering the temperature further after magnetisation is complete. This reproduces the effect of having left a more highly magnetised sample to relax under flux creep for a long period of time. This makes such a large difference because the amount of flux changes with time in a logarithmic fashion. This has been shown, for a cylindrical geometry, by Beasley et al[18];

$$\phi(t) = \phi(t_o) \pm \alpha\varphi(r)\ln\left(\frac{t}{t'}\right) \qquad \text{eq 1.24}$$

where α is a constant, $\varphi(r)$ is a function of the sample radius and t' is an arbitrary reference time. Wienstien et al[19] have reported a reduction in creep rate by a factor of 1000, using a method called PAC (post activation cooling), over a temperature reduction of only 6K. This type of reduction in relaxation makes re-powering unnecessary, and increases the attractiveness of HTSC for practical uses.

1.8 References

1. H. Kammerlingh-Onnes, *Comm. Leiden Nr.*, **108** *Proc. R Acad. Amsterdam* **11**, 168 (1908)

2. H. Kammerlingh-Onnes, *Akad. van Wettenschappen*, **14**, 113, 818 (1911)

3. J. Bardeen, L.N.Cooper and J.R Schrieffer, *Phys. Rev.*, **106**, 162-164 (1957)

4. A. C. Rose-Innes and E. H. Rhoderick, *Introduction to Superconductivity.* Pergamon Press (1978)

5. J. G. Bednorz and K. A. Muller, *Z. Phys.* B, **64**, 189-193 (1986)

6. B. Dunn, C. T. Chu, L. W. Zhou, J. R. Gruner, *Adv. Ceram Mat.*, **2**, (1987)

7. C. Kittel, *Introduction to Solid State Physics*, J. Wily and Sons Inc. (1995)

8. M. Tinkham, *Introduction to Superconductivity*, J. McGraw-Hill. (1996)

9. D. R. Tilley and J. Tilley, *Superfluidity and Superconductivity*, Graduate Student Series in Physics, Adam Hilger (1990)

10. A. L. Abrikosov, *Zh Eksp. Teor. Fiz.* **32,** 1442

11. W. H. Kleiner, L. M. Roth and S. H. Autler, *Phys Rev.* **133**, A1226 (1964)

12. W. Tuyn, *Comm. Leiden*, **198** (1929)

13. C.P. Bean, *Phys. Rev. Lett.*, **8**, 250-253 (1963)

14. C.P. Bean, *Rev. Mod. Phys*, **36**, 31-39 (1964)

15 K. No, D. Chung and J.Kim, *J. Mater. Res.*, **4**, 28 (1990)

16. Y. B. Kim, C. F. Hempstead and A. R. Strand, *Phys. Rev.*, **129**, 528 (1963)

17. P. W. Anderson, *Phys. Rev. Lett.* **9**,309 (1962)

18. M.R. Beasley, R. Labusch and W. W. Webb, *Phys. Rev.*, **181**, 682-700 (1969)

19. R. Weinstein et al, *Supercond. Week IPD Report*, (1995)

Chapter 2: Introduction to the Processing of Bulk RE123 Materials

2.1 Introduction

YBCO is an anisotropic crystalline ceramic and as such poses many problems when considering its production and its application. The mechanical properties of YBCO do not allow it to be easily worked or shaped[1-4]. More importantly however, is the fact that the critical current of the bulk is not an intrinsic property of the material, but rather is dependent on the microstructure of the given sample. The value of the engineering critical current in multi-granular YBCO is in fact formed from two other currents, the inter and the intra granular currents. The intra-granular current flows in a single grain and so defines the limiting value of J_c. The inter-granular currents are flow across grain boundaries. There are often non-superconducting phases present at grain boundaries, which combine with factors such as poor grain alignment to result in poor coupling between grains. Currents pass between the grains in the same way as through a Josephson junction, making the inter-granular current much weaker than the intra-granular current. This is particularly problematic for high temperature superconductors as the coherence lengths (ξ) of these materials are considerably shorter than those of low temperature superconductors, meaning that the superconducting wave function will attenuate greatly due to the presence of almost any type of grain boundary.

Another factor to be considered when processing YBCO is that to be useful in any applications the material must remain superconducting in the presence of high magnetic fields. For this reason the small flux pinning force within the grains must be increased. As well as reducing the field dependence of J_c, increasing pinning forces will also reduce the effects of thermally activated flux creep upon pseudo-permanently magnetised samples.

In this chapter the various methods developed for the production of bulk YBCO shall described and discussed. In addition, the structure of this material shall be presented and explained in detail.

2.2 Sintering

Sintering processes are commonly used in ceramic processing as they allow the precise shaping necessary for many applications. Also, compounds may be produced at relatively low temperatures via solid-state reactions, allowing characteristics such as grain size to be controlled by heat treatment conditions. However, although sintered bulk YBCO may be produced to exhibit high values for the critical temperature, values of the critical current are not high enough to be useful in many applications.

Sintered materials are no exception in that J_c is dependent on several factors; homogeneity, density, oxygen content, pinning forces, cracks and coupling. All of these factors are dependent on the processing conditions. When YBCO is sintered it is heated up to just below its melting temperature at a rate limited by the effects of superheating. During sintering small particles form larger grains and hence reduce surface energy. As temperature increases, the equilibrium grain size increases accordingly[5]. If the heating rate is too high there is not enough time for this equilibrium size to be reached and so superheating will occur, causing melting and the formation of non-superconducting liquid phases. Density also increases with temperature and thus porosity is reduced.

Although the increase in density caused by increased temperature would seem beneficial with respect to the value of J_c, the increase in the amount of liquid phase to be found at grain boundaries due the increase in temperature causes a reduction of connectivity (i.e. poor coupling) of the grains, and in so doing, reduces J_c. Ideally, one would wish to be sintering a densely packed mixture of very fine powders, which would allow the production of a dense material that would not suffer from the effects associated with liquid and which could be sintered at 925°C. The small initial particle size allows

sintering to occur at a low temperature, i.e. sintering cannot take place unless the initial particle size is smaller than the equilibrium size at that temperature. The low temperature makes for good coupling and reduces the stresses that may cause cracks. Also, the increased surface area created by reducing the size of the particles allows a greater reduction in the surface energy during sintering, making the process more efficient with fine powders.

Despite all of these measures critical current values are still low in sintered materials. This is partly due to the anisotropic structure of YBCO, which manifests itself in the anisotropic nature of its coefficients of expansion. This inequality in expansion and contraction causes large stresses to build along grain boundaries and so cracks form under thermal cycling. The tetragonal to orthorhombic transition which occurs during oxygenation also contributes to these stresses as the c axis shrinks during the transformation and so loads more stresses onto the randomly orientated grains. In addition, the low value of ξ intrinsic to YBCO means that the miss-alignment present at grain boundaries will result in the inter-granular current being far less then the intra-granular current.

In conclusion, sintered materials have not reached a high enough standard to be used for most prospective applications, with the possible exception of current fault limiters.

2.3 Melt Growth Processes

As a result of work carried out to reduce the effects of weak links on the current carrying capacity of bulk YBCO Jin et al[6, 7] developed the melt textured growth process (MTG). This reduces the number of grain boundaries, and hence weak links, by growing larger grains.

In the MTG process, sintered or pressed pellets of calcined powder are melted and then slowly cooled in a temperature gradient. Preferred orientation for grain growth is in the

ab plane and so the effects of poor grain alignment can be reduced by using a temperature gradient to select grains orientated in the desired direction. Critical currents in excess of 10^4 Acm^{-2} have been achieved with samples prepared in this manner. In order to more clearly understand the phase relationships and the processes taking place during the heating cycle, it is useful to have a pseudo-binary phase diagram as shown in Fig 2.1. Above approximately 1200°C, Y_2O_3 plus liquid (L) are stable. When cooled the following peritectic reaction takes place:

$$Y_2O_3 + L(BaO + CuO) \rightarrow Y_2BaCuO_5(211) \qquad \text{eq 1.1}$$

Upon further cooling to around 1000°C, the 211 reacts with the liquid to produce the 123 phase:

$$Y_2BaCuO_5 + L(3BaCuO_2 + 2CuO) \rightarrow 2YBa_2Cu_3O_{7-\delta} \qquad \text{eq 1.2}$$

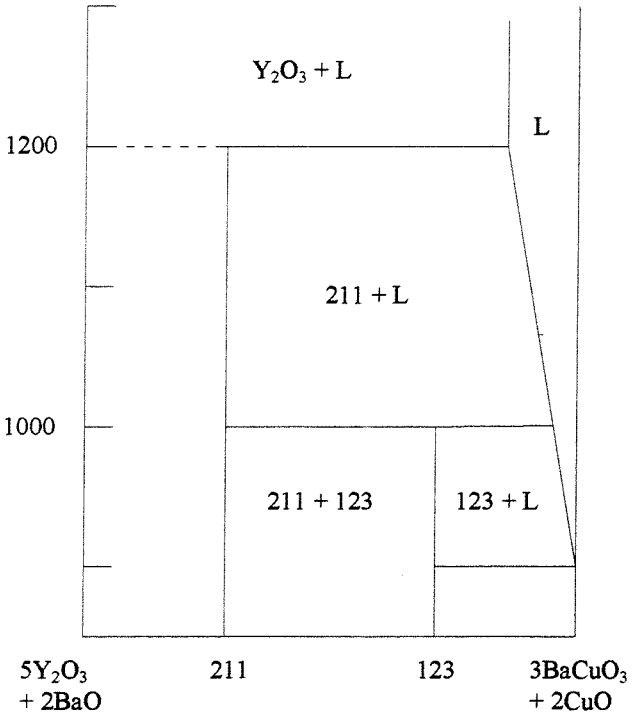

Fig 2.1 Pseudo-binary phase diagram for YBCO.

Shown in Fig 2.2 is a schematic illustration of the heating cycle used to produce a MTG sample. By comparing the two figures one can see how the phase changes taking place during sample preparation.

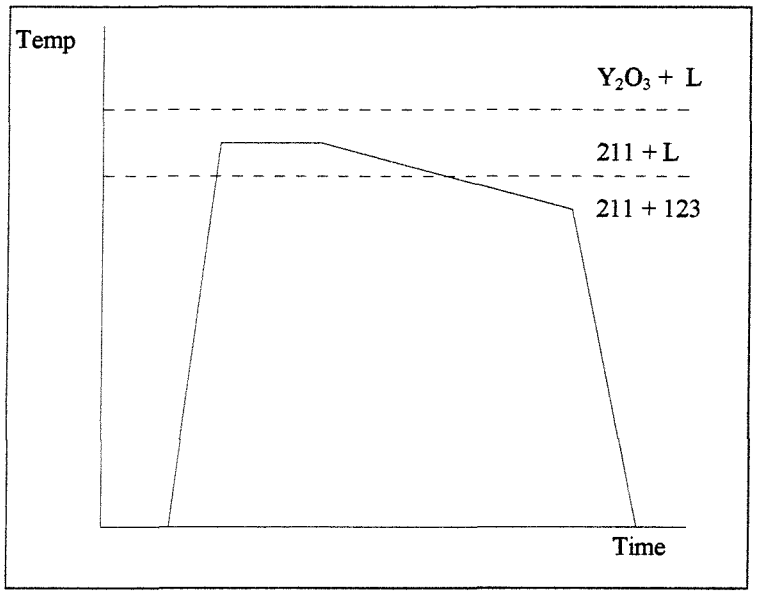

Fig 2.2 Schematic MTG heating cycle.

As can be seen in Fig 2.2, in the MTG process the sample is slowly cooled through the peritectic temperature in order to attain a highly textured material. However, this also causes 211 inclusions to become large and grow in a non-uniform manner. For the reaction to precede continuously it is necessary to provide a uniform distribution of 211 and liquid. As a result of this not being the case bad connectivity and poor microstructure result. In an attempt to bypass this coarsening of the 211, the MTG has been modified[8-10]. This modified process (MMTG) is shown in Fig 2.3.

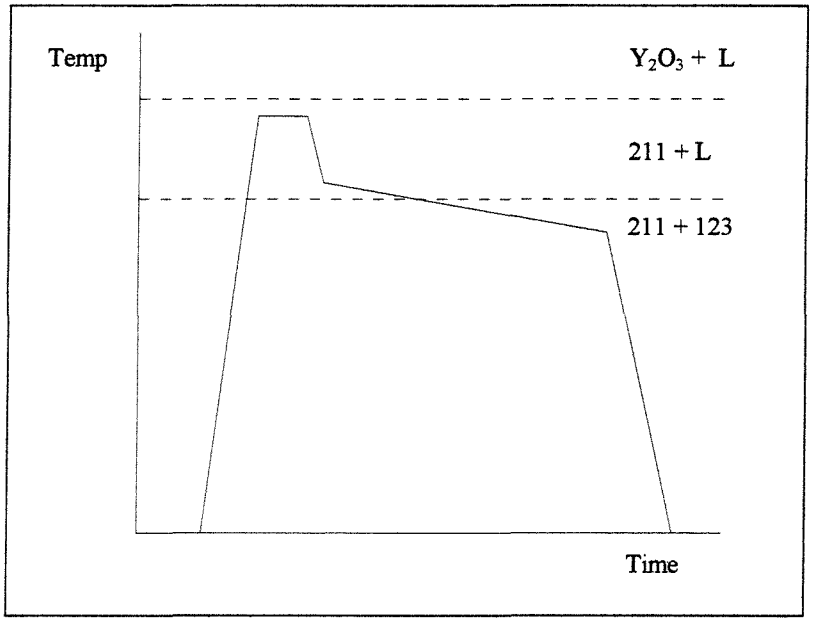

Fig 2.3 Schematic MMTG heating cycle.

Fig 2.3 shows how in the MMTG process, after heating, the sample is rapidly cooled to the peritectic temperature and then slowly cooled. The result of this modification is a large reduction in the coarsening of the 211 which in turn results in a considerable improvement in pinning properties and a reduction of liquid phases present at grain boundaries.

By modifying these heating cycles we are demonstrating the control we may exert on the microstructure of our samples. In order to further improve the distribution of the 211, that is to say create a finer, more uniform distribution, the quench melt growth process (QMG) is the next step, as shown in Fig 2.4.

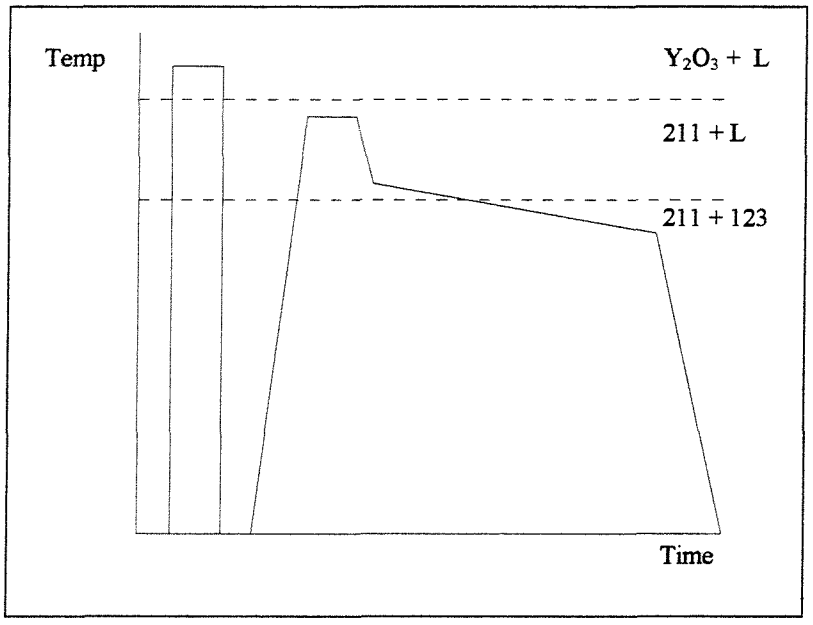

Fig 2.4 Schematic QMG heating cycle[8] .

In the first part of the cycle the mixture of calcined powders is heated into the Y_2O_3 + L region and then splat quenched using cold copper plates. The resulting mixture of Y_2O_3 and solidified liquid phase is then ground up to produce a powder with a uniform distribution of fine Y_2O_3 particles. The second part of the cycle is identical to the MMTG with the exception that, as the distribution of Y_2O_3 is uniform, the resulting distribution of 211 will also be uniform, creating a much-improved grain. Unfortunately, unlike the MTG process there is little residual 211 phase left after the slow cooling through the peritectic region. This lack of 211 results in a poor flux pinning force and so gives a low value of Jc. This problem may be overcome by shifting the starting composition towards the 211 rich region. This appreciably increases J_c to a useful level.

An alternative to using melt quench powders is to use a mixture of 211 and others as starting materials[11-13] , i.e. mixing Y_2BaCuO_5(211) with $BaCuO_2$(011) and CuO(001). In this way this way the size and distribution of 211 particles may be controlled before heat processing begins. Using these powders in conjunction with the MMTG process has been shown to yield high quality samples.

Research has shown[14-17] that doping with Pt, $BaSnO_3$, CeO_2 or Rh is effective in reducing the size of the 211 inclusions and thereby increasing J_c values. These dopants are able to this as they act as nucleation sites for the 211 inclusions without poisoning the superconducting bulk. In addition, U^{235} has been used very successfully as a dopant. Not only is uranium successful at forming an excellent distribution of pinning centres but, in addition, doped material may be irradiated with thermal neutron resulting in the fission of the uranium. The fission fragments are emitted in opposite directions and in so doing cause the formation of straight, columnar pinning centres. Previously, pinning centres had been created by irradiating the sample with protons of an energy around 200 Mev, but the pinning centres created do not display such a favourable geometry.

A method for ensuring grain orientation and also of creating a preferential nucleation site for the initiation of crystal growth is to use a seed. $SmBa_2Cu_3O_{7-\delta}$ has the same structure as Y123 but has a slightly higher melting point (~1040°C). If a seed of Sm123 is placed on the top surface of an YBCO pellet, as the sample is heated some of the Sm123 will be taken into the YBCO by solid-state diffusion. Thus, as cooling begins, the area around the seed which will contain some Sm123, will nucleate first, as the mixture of Sm123 and Y123 will have a higher melting point than pure Y123. In most instances it is necessary to provide additional cooling around the area of the seed so as to ensure preferential nucleation. In this way it is possible to produce large, single grain samples and thus eliminate the problems associated with grain boundaries. This seeding process has been used throughout this work in combination with various melt textured growth cycles to produce high quality single grain material suitable for study.

The processes such as phase migration and crystal growth kinetics have been modelled by several authors. These models all implicate the necessity of having Y211 inclusions present along the liquid phase growth front. The presence of the 211 inclusions allows phase migration to take place and so facilitates the solidification of the 123 phase from the melt. It can be concluded from this that distribution of the 211 particulates is important not only for the distribution of pinning centres in the solidified post processed

123 bulk but also for the kinetics of the growth process itself. Direct observations of the rate of crystal formation have clearly demonstrated this to be the case.

2.4 Powder Preparation

Generally, starting powders are prepared from high purity Y_2O_3, $BaCuO_3$ and CuO. It is important that the starting materials be pure as contaminants such as Fe, Ni and Co have a disastrous effect on T_c. The powders are measured out to give the correct proportions of Y, Ba and Cu, and then thoroughly mixed. The well mixed powders are then calcined in flowing oxygen at 850-950°C for 1 to 24 hours. Once the powder has cooled it re-ground. This process is repeated several times, as the more times it is repeated, the better the homogeneity of the final powder.

Alternately, one could decide to use a solution technique[18] to prepare powders. The most common forms in use are the sol-gel techniques[19] and co-precipitation[20] methods. Co-precipitation has been successful using citrates, oxalates, carbonates and freeze drying processes. The sol-gel process derives materials from alkoxides, nitrates, acetates, hydroxides, emulsions and organically bridged polymers. The advantage of these processes is the production of powders at a level of homogeneity and fineness unobtainable by solid state mixing. A review of these and other precursor powder preparation methods has been produced by Roa et al[21].

2.5 Structure of YBCO

Based on the evidence of X-ray and neutron diffraction, a structure composed of a stack of 3 perovskite-like cubes has been revealed. It has been recognised that Y123 crystallises in two forms; the tetragonal form at high temperatures, which then changes to

the orthorhombic form on cooling because of oxygen ordering. The two structures are shown in fig 2.5.

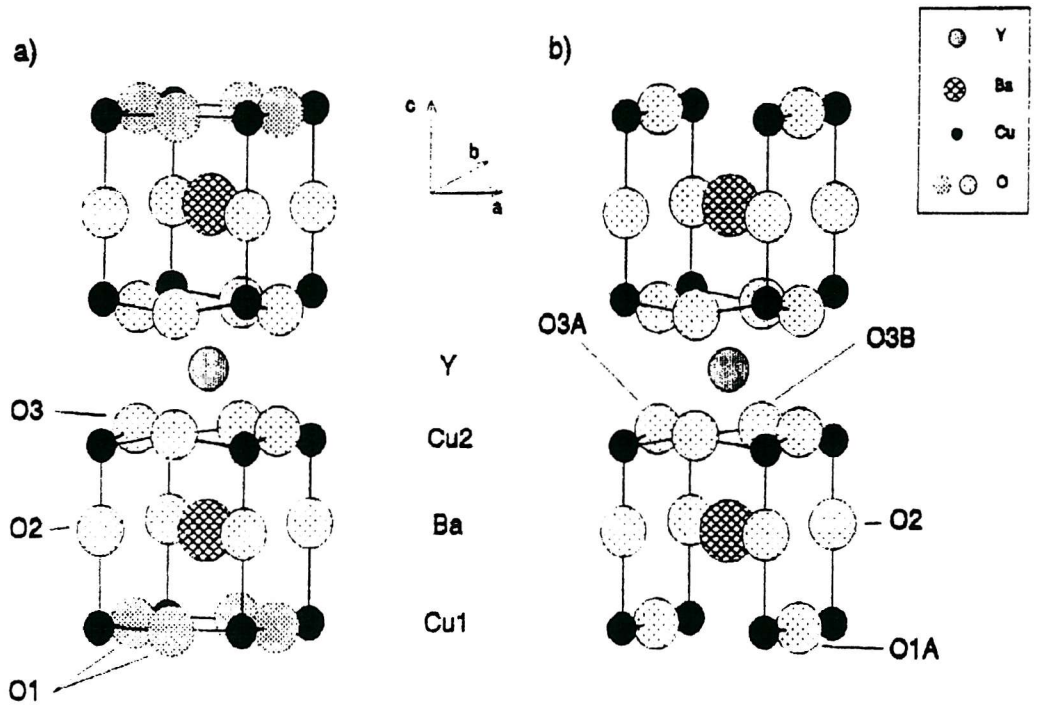

Fig. 2.5 Tetragonal and orthorhombic structures of YBCO

Fig 2.5a shows the tetragonal structure of Y123. Its cell dimensions, 3.9×3.9×11.7 Å, demonstrate how its built from three almost perfect cubes. As can be seen above, all O oxygen atoms occupy perovskite-like anion positions halfway between copper atoms along cube edges. The O2 oxygens in the Ba-O plane and the O3 oxygens at the level of Cu2 are fully occupied which gives six oxygen atoms per unit cell. However, there are no oxygens at the Y level, giving slabs of $BaO/CuO_2/Y/CuO_2/BaO$ (1-2-2 repeat blocks). This is a common feature in high T_c superconductors. Therefore copper adopts a linear two co-ordination with two Cu1-O2 bonds at 1.8Å. The Y is in an eight fold cube co-ordination, with eight equivalent Y-O3 bonds at 2.4Å. The eight co-ordinated Ba site has four Ba-O2 bonds at 2.7Å and four Ba-O3 bonds at 2.8Å. Each Cu2 has four bonds to O3

oxygens at 1.94Å and a fifth weakly bound apical O2 at 2.45Å. The Cu2-O3 are buckled, with the O3 displacement along the c axis towards the Y site (Cu2-O3-Cu2 angle ~167°). The O2 and O3 oxygens are in a distorted octahedral co-ordination. The O2 is co-ordinated with one short Cu1-O2 bond, and a longer Cu2-O2 bond at around 2.45Å. This suggests that there is little interaction between the Cu2-O layers and the Cu1 in $YBa_2Cu_3O_6$. Oxygen content may exceed six, depending on the temperature and the annealing conditions. Excess oxygen occupies the O1 site, which is able to accommodate up to two oxygens per unit cell.

The orthorhombic form of Y123 (Fig 2.5b) is almost identical to its tetragonal form. It's a and b axis differ by ~2%, giving cell parameters of 3.82×3.88×11.65Å. The positions of the Y, Ba, Cu1 and Cu2 cations and O2 oxygens are identical to those in the tetragonal structure. However, the O3 site splits into two fully occupied sites, O3A (0, 1/2, .38) and O3B (1/2, 0, 0.38). Also the partially occupied tetragonal O1 site splits into O1A (0, 1/2,0) and O1B (1/2,0,0). The co-ordinate of the Y and Cu differ only fractional between the two structures. In the orthorhombic structure Y is co-ordinated to eight oxygens in a distorted cube with O3A and B giving an average Y-O bond of 2.4Å. Cu2-O3A and Cu2-O3B form sheets of square planar Cu-O ~1.9Å, and an apical O2 bond at 2.3Å. The Cu2-O3 bond angles are ~165°. With Y123O, the oxygen concentrates in O1A, which causes an enlargement of the b axis relative to the a axis. Therefore, in ideal $YBa_2Cu_3O_7$ the O1A is fully occupied whilst the O1B site is vacant, giving chains of CuO_3 parallel to the b axis. Oxygen in the O1A site is linked to two Cu1 atoms (~1.94Å) and four Ba atoms (~2.9Å). The Ba has a co-ordination of ten if O1A is fully occupied. It ca be seen that the O2 oxygen is more equidistant between Cu1 and Cu2 in the orthorhombic case, which suggests that interaction between Cu2-O planes is enhanced in Y123O. Relative amounts of O1A and O1B vary according to synthesis conditions, and more than seven oxygens may be accommodated under high oxygen pressure[22] .

Many attempts have been made to produce compositional variants of Y123. A review of the structural aspects of extensive substitution studies has been produced by Beyers and

Shaw[23]. Cu has been partially replaced by Fe, Co, Ni, Zn, Ga, Mg and Al, but no advancement of T_c has resulted. All lanthanide elements, except for Ce and Tb can be fully substituted in Y123 but again with little effect on T_c.

The tetragonal structure described above exists above 900°C. As the material cools it takes up oxygen between approximately 800 and 700°C and the structure transforms to orthorhombic. Generally the formula of YBCO is written as $YBa_2Cu_3O_{7-\delta}$. For $0.1< \delta <0.5$ the structure of YBCO is orthorhombic and superconducting. During the tetragonal-orthorhombic transition shrinking occurs, particularly along the c axis. This causes stresses throughout the material which can result in cracks. The orthorhombic structure allows for the formation of twinning planes, which form along the {110} plane and act to relieve stress. Y211[24] inclusions and a dispersion of Ag[25, 26, 27] particles have also been shown to reduce cracking. As is clear from the structure described above, YBCO is highly anisotropic, especially when comparing the ab to the c plane. This, combined with a high coefficient of thermal expansion which is correspondingly anisotropic, induces an even greater tendency to crack. Combined with the low values of fracture strength, ductility and toughness, all together this is a very difficult material to work with.

References

1. T. M. Shaw, S. L. Shinde, D. Dimos, R. F. Cook, P. R. Duncombe and C. Kroll, *J. Mater. Res.*, **4** (1989)

2. A. S. Raynes, S. W. Freiman, F. W. Gayle and D. L. Kaiser, *J. Appl. Phys.* Vol.**70** (1991)

3. T. Oka, Y. Itoh, Y. Yanagi, H. Tanaka, S. Takashima, Y. Yamada and U. Mizutani, *Physica C*, vol. **200** (1992)

4. A. Goyal, P. D. Funchenbush, D. M. Kroeger and S. J. Burns, *J. Appl. Phys.* Vol.**71** (1992)

5. T.J. Rand, Z. Yi, C. Beduz, K. Pham and R. Riddle, *Presented at EUCAS '93, Ocober 1993,* Gottingen, Germany

6. S. Jin, T.H. Tiefal, R.C. Sherwood, M.E. Davis, R.B Van Dover, G.W. Kammlott, R.A. Fastnacht and H.D. Kieth, *Appl. Phys. Lett.*, **52**, 2074 (1988)

7. S. Jin, T.H. Tiefal, R.C. Sherwood, M.E. Davis, R.B Van Dover, G.W. Kammlott, R.A. Fastnacht and H.D. Kieth, *Phys. Rev.*, B**37**, 7850 (1988)

8. M. Murikami, M. Morita, K. Doi and M. Miyamoto, *Japan. J. Appl. Phys*, **28**, 1189 (1989)

9. H. Hojaji, K.A. Micheal, A. Barkatt, A.N. Thorpe, F.W. Matthew, I.G. Talmy, D.A. Haught and S. Alteruescu, *J. Mater. Res.*, **4**, 28 (1989)

10. R. J. Polland, D. G. McCartney, N. McN. Alford and T. Button, *Suppercond. Sci. Tchnol.*, **2**, 169 (1989)

11. Z. Lian, Z. Pingzian, J. Ping, W. Keguang, W. Jingrong and W Xiaozu, *Suppercond. Sci. Tchnol.*, **3**, 490 (1990)

12. Z. Lian, Z. Pingzian, J. Ping, W. Keguang, W. Jingrong and W Xiaozu, *IEEE Trans. Mag.* MAG-**27**, 912 (1991)

13. K. No, D. Chung and J.Kim, *J. Mater. Res.*, **4**, 28 (1990)

14. N. Ogowa, I. Hirabiashi and S. Tanaka, Physica C, **177**, 101 (1991)

15. P. McGinn, W. Chen, N. Zhu, L, Tan, C. Varanasi and S. Segupta, *Appl. Phys. Lett.*, **59**, 120 (1991)

16. N. Ogowa, and H. Yoshida, Adv. Supercond., **4**, 132 (1992)

17. N. Ogowa, I. Hirabiashi and S. Tanaka, *Physica C*, 185-189, 2409 (1991)

18. E. A Hayri, M. Greenblatt, K. V. Ramanujachary, M. Nagano, J. Oliver, M. J. Miceli and R. Gehrhart, *J. Mater. Res.*, **4**, 1099 (1989)

19. B. Dunn, C. T. Chu, L. W. Zhou, J. R. Cooper and G. Gruner, *Adv. Ceram. Mat.*, **2**, 343 (1987)

20. M. R. Zacharia and S. Huzarewicz, *J. Mater. Res.*, **2**, 343 (1987)

21. C. N. R. Rao, R. Nagarajan, R. Vijayaraghavan, Supercond. Sci, Technol., 6, 1-22 (1933)

22. Q.W. Yan, P.L. Zhang, Z.G. Shen, J.K. Zhao, Y. Ren, Y.N. Wei, T. D. Mao,C.X. Lui, T.S. Ning, K. Sun and Q.S. Yang, *Phys. Rev.*, B**36**, 8810 (1987)

23. R. Beyers and T.M. Shaw, *Sol. State Phys.*, **42**, 135 (1989)

24. H. Fujimoto, M. Murikami, T. Oyama, Y. Shiohara, Koshizuka and S. Tanaka, *Japan J. Appl. Phys.*, **29**, L1793 (1990)

25. A. Goyal, W. C. Oliver, P. D. Frunkenbush, M. D. Kroeger and S. J. Burns, *Physica* C, **183**, 221 (1991)

26. C. Y. Huang, H. H. Tai and M. K. Wu, *Mod. Phys. Lett.*, B**3**, 525 (1989)

27. H. Fujimoto, M. Murikami, T. Oyama, S. Gotoh, Y. Shiohara, Koshizuka and S. Tanaka, *Japan J. Appl. Phys.*, **29**, L1991 (1990)

Chapter 3: Processing of Single Grain Melt Textured Bulk YBCO

3.1 Introduction

In order for the superconducting properties of bulk YBCO to match the needs of possible applications and research it is necessary that a method for reliably producing large, single grain monoliths of the material be developed. The melt textured growth (MTG)[1,2] approach described in chapter 2 modified to include seeding[3-9] has shown a high degree of success with respect to achieving this. In this chapter, the procedure evolved for implementing the seeded MTG process is described, the nature of the formation of single grain YBCO investigated and the quality of the resultant material assessed.

3.2 Processing Configuration

Although the general processing conditions necessary for the seeded melt growth of single grain YBCO are well known, the development of a working system for the production of high quality material is still a lengthy, complex problem. For example, although many authors acknowledge the need for temperature gradients during processing, the method by which these temperature gradients are obtained is for the individual to ascertain. In this section the development of a successful system for the production of large grain YBCO is described.

Melt texturing of RE123 materials takes place in a temperature range which varies between approximately 930°C and 1100°C, therefore the development of a high temperature furnace is the first priority. This furnace must be able to provide a variable vertical temperature gradient and allow provision for other devices to be used to apply a horizontal temperature gradient. Moreover, in order to prevent damage to the furnace from liquid phases produced by the pellet during processing, the furnace must be

configured so as to allow the pellet to be supported in a standalone manner. For these reasons the standard, horizontal tube furnaces used for tape processing were not suitable.

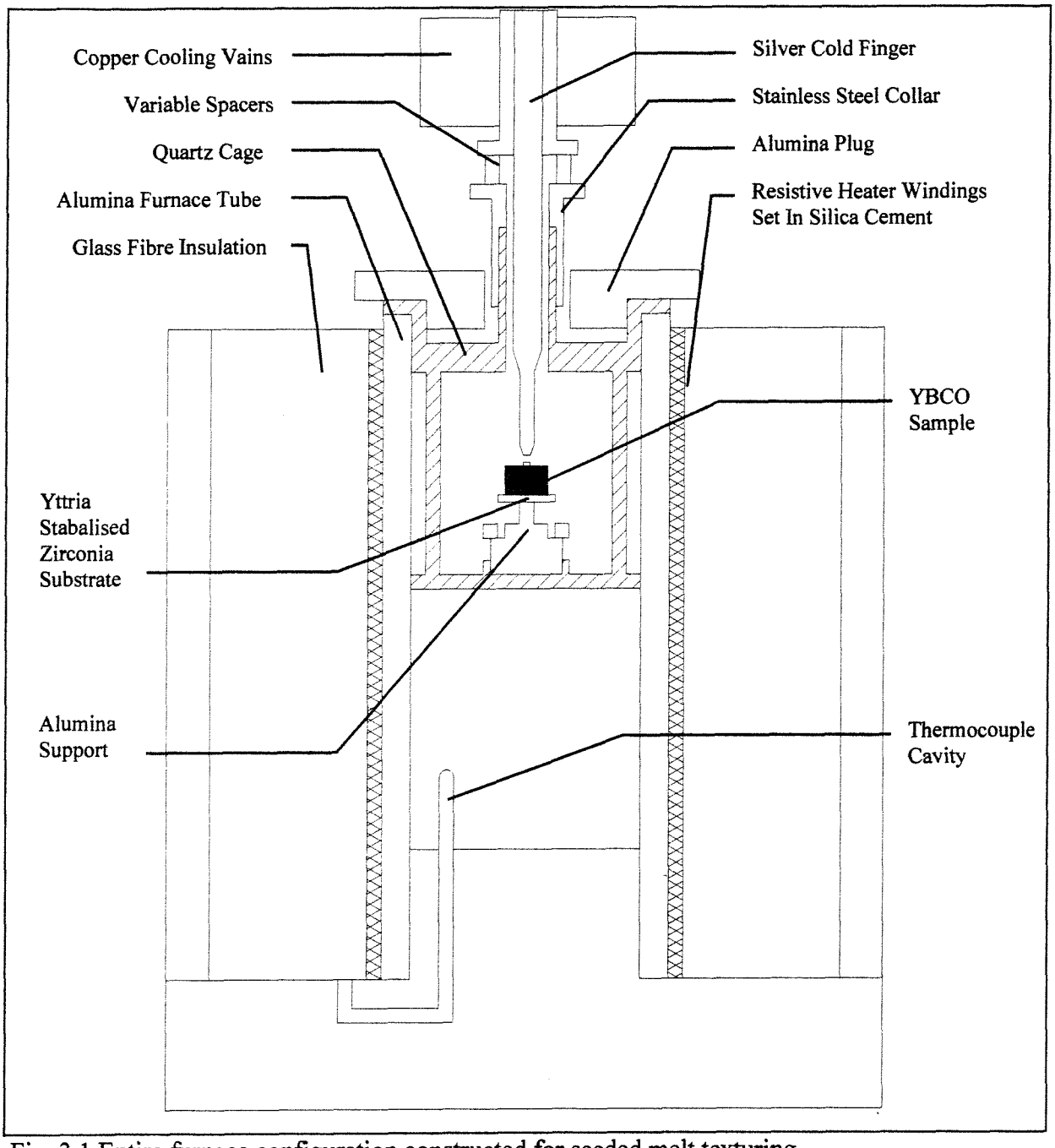

Fig. 3.1 Entire furnace configuration constructed for seeded melt texturing.

The furnace configuration chosen was a vertical tube furnace, shown in Fig. 3.1. In this design a high tolerance alumina tube is used as the mandrel around which furnace wire is wound. This wire is then secured in place using silica cement which becomes a hard, temperature resistant ceramic when fired. This whole arrangement is then insulated using fibre glass wool high temperature insulation. The bottom of the furnace sits on an alumina brick base, which provides insulation and stability whilst allowing a thermocouple, used as a reference for the furnace controller, free access to the furnace cavity. The top of the furnace is closed off using a range of small plugs fashioned from alumina brick. The furnace wire is uniformly wound along the length of the tube with a spacing of 1.5mm, except for the first 16 turns, which are wound with no spacing. This is done so as to prevent the temperature gradient near the top of the furnace from being excessively large.

The vertical design instantly provides a vertical temperature gradient which varies considerably along the vertical axis, ideal for the development of a melt processing system. This is illustrated in Fig 3.2, which is a plot of the temperature-position calibration data taken using a standard J-type thermocouple at a set controller temperature of 1000°C. Two of the plots shown in this figure illustrate how the gradient may be controlled using alumina of varying thickness placed at the top of the tube. Also Fig 3.2 shows how different tubes wound at different times show very little variation in temperature profiles. This is important as the lifetime of a furnace tube is likely to be relatively short due to the high temperature of operation.

Fig.3.2 is useful in that it gives an approximate guide to the temperatures and gradients one would expect when processing a pellet. However, due to the nature of the radiative heat transfer process which takes place in this kind of system, the real temperatures on the surface of the sample being processed will be considerably different and highly dependent on geometry. For this reason more realistic calibrations are necessary for each specific configuration.

Illustrated in Fig 3.3 is the design of support cage/cold finger system. It can be seen in Fig 3.1 that the cage has been designed so as to fit into the furnace tube and hold itself in place with a rim which is wider than the diameter of the furnace tube. This cage serves several purposes. Firstly it provides a platform on which the pellet may be mounted without being in contact with the furnace tube and secondly the cage holds in position a "cold finger", the function and operation of which will be discussed later.

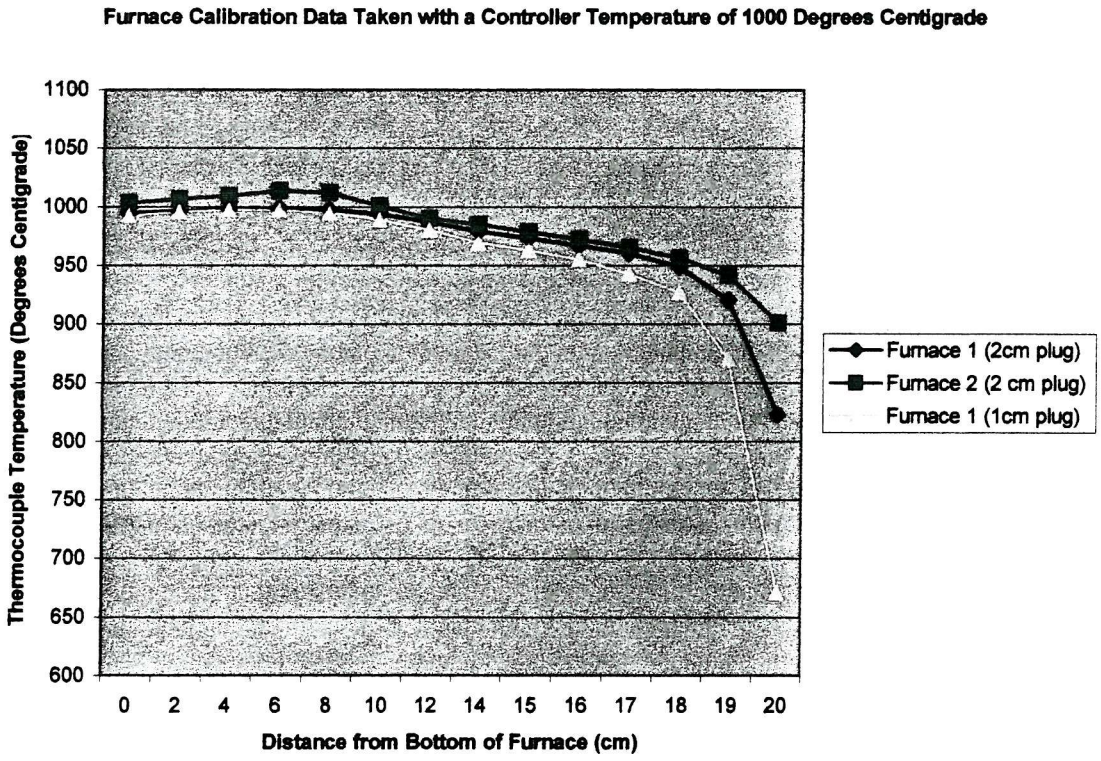

Fig 3.2 Calibration data for vertical tube furnace.

The cage is constructed from quartz, a resilient material which has a melting point in excess of 1500°C, a temperature far in excess of that needed for processing RE123 materials. It's transparency is also a useful feature as opaque materials such as alumina have a larger effect on the radiative transfer processes. With heat transfer in mind, the cage has been designed so that the platform is attached with three thin rods, thus minimising any effects on the temperature distributions throughout the furnace or the

pellet. The quartz spout at the top of the cage serves to position and support the cold finger.

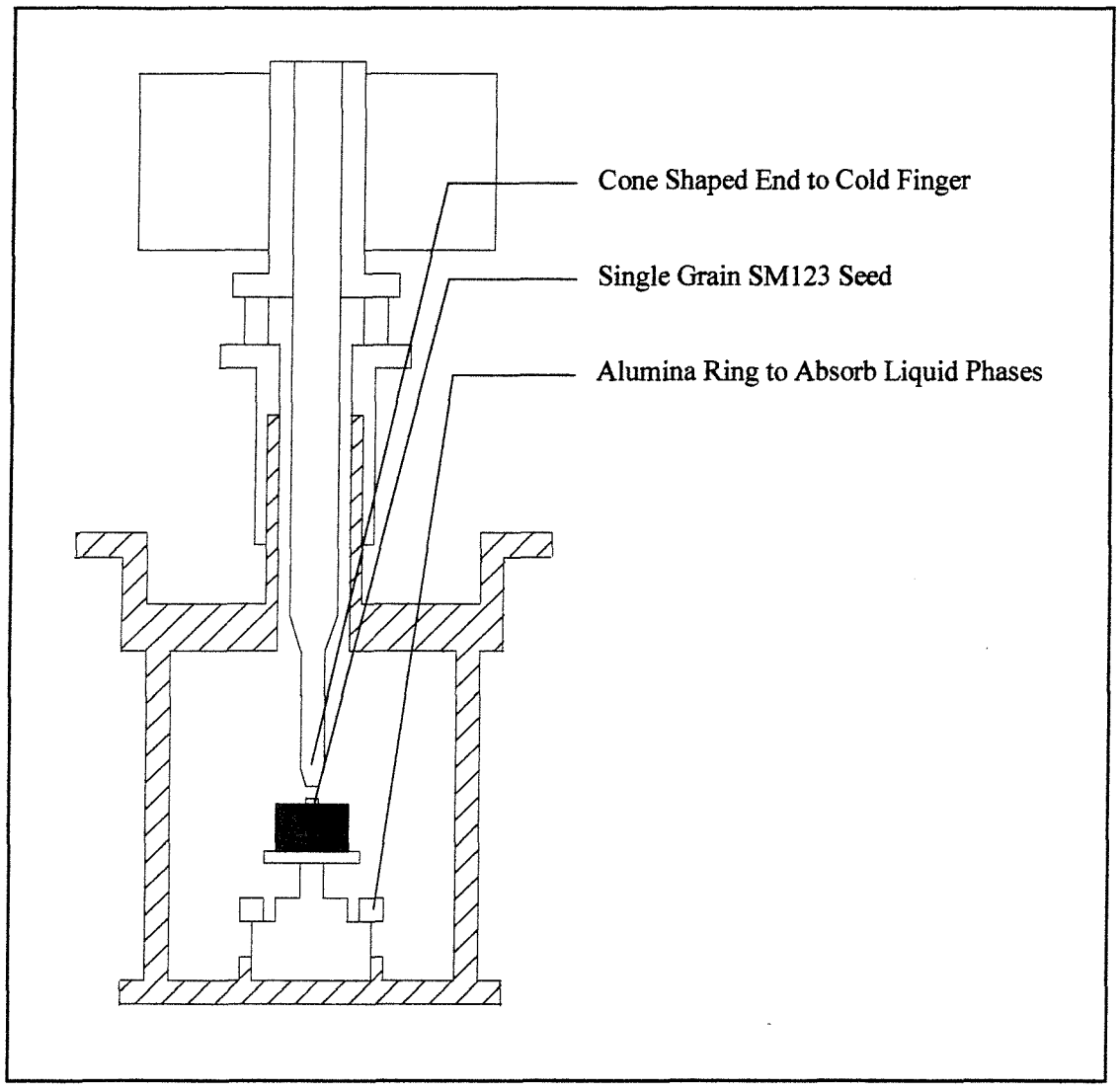

Fig 3.3 Illustration of quartz cage, cold finger and pellet support design.

For the production of large, single grain bulk material it is essential that nucleation takes place at the position of the seed. For this reason it is imperative that the cold finger is positioned accurately above the seed region, as the purpose of the cold fingers is to provide the additional cooling that determines the point where nucleation is initiated. The main body of the cold finger is made from silver because of its high conductivity, low rate

of oxidation and fairly high melting point. The top region is constructed from copper with many fins incorporated into the design. Outside the furnace at lower temperatures we are able to take advantage of copper's superior thermal conductivity and so provide more efficient cooling. The cold finger sits on top of a stainless steel collar which fits around the quartz spout, thus minimising the amount of horizontal motion of the cold finger once in place. Alumina spacers are placed in between the collar and the corresponding section of the cold finger, allowing the vertical position to be altered with a high degree of accuracy. Setting the separation between the pellet and the cold finger within the reference frame of the quartz cage allows the positioning of all the components on the bench, prior to placing the set up into the furnace. This is advantageous as it allows all criteria to be checked visually before processing.

The pellet itself rests on a substrate made from yttria stabilized zirconia, which in turn is supported by an alumina piece. This alumina piece is made so that the smallest possible area is in contact with the substrate thus reducing the amount of liquid phases able to flow away from the pellet during thermal processing. Some liquid loss in this manner is unavoidable however, so a ring of less dense, more porous alumina is placed further down the alumina support, the function of which is to absorb any liquid and prevent contamination of the quartz platform.

As stated previously, the temperature profiles to be found inside the furnace during pellet processing will differ considerably to the data gathered using a simple single thermocouple set up. For this reason it was necessary to simulate the processing configuration whilst carrying out calibration. This was essential not only to establish the correct horizontal temperature gradient and absolute temperatures on the surface of the sample, but also to calibrate the effects of the cold finger and ascertain the ideal distance between seed and cold finger. This calibration was carried out using the experimental set up shown in Fig 3.3 but with several modifications. A pellet of identical dimensions to real samples was pressed from CeO_2 powder and sintered. Three small indentations were made using a diamond drill, allowing welded differential thermocouples to be embedded

into these indentations using silica cement. The voltages from these welded contacts could then be measured against a reference thermocouple which was held at 0°C by iced water. The thermocouples were fed out of the furnace through holes in the top of the quartz cage and so in no way affected the temperature profiles within the furnace.

In the original design, a cartridge heater with an integrated thermometer was incorporated into the top of the cold finger. This was intended to allow control of the heat transfer by modifying the end temperature of the cold finger. However, calibration using the process described above quickly showed that this was not viable. The increase in temperature resulting from the use of the heater caused thermal expansion along the length of the cold finger. This would then effect the amount of cooling which took place at the seed in an extremely unpredictable manner, so much so that this method was abandoned.

The data gathered in this manner allowed the optimum arrangement for processing to be devised. It quickly became apparent from this kind of calibration that the thermal expansion of the cold finger during thermal cycling and the gap between the cold finger and the centre of the pellet were critical factors in determining the temperature gradient across the top of the sample. In order to reduce the extreme dependence of the amount of cooling on the separation it was necessary to shape the end of the cold finger into a flattened cone, which is illustrated in Fig 3.3. In this way, the dependence on separation of the solid angle available for radiative transfer is reduced.

3.3 Sample Preparation

Once the furnace configuration necessary for the thermal processing of seeded melt textured YBCO was constructed, the next step is to develop and perfect a procedure which could be used to manufacture high quality single grains. During this procedure much was learnt about the practicalities involved whilst at the same time considerable insight was gained into the growth kinetics of these materials.

The effects of the starting powders, dopants and stoichiometric ratios on the material produced are discussed in detail in chapters 2 and 4. As the focus in this chapter is on the techniques and mechanisms involved the growth process rather than on the resulting microstructure, the reader may assume that all samples are prepared from powders mixed with a stoichiometry of 0.85Y123 + 0.12Y211 (mol ratio) doped with 0.5%wt. 4 μm platinum powder. The Y123 powders used were commercially available Merck powders. The Y211 phase was mixed from Goodfellow's high purity chemicals and again repeatedly ground and calcined.

The technique for the preparation of the YBCO powder used for the manufacture of all the samples discussed in this chapter is described in detail below. This process was chosen based on the work carried out by Mr. D. Neat and may be found in his Msc. thesis produced at Southampton University.

Process Cycle	Ramp Rate	Temperature	Dwell Time
	°C/hr	°C	Min
1	96	750	0
	12	860	1000
2	120	600	360
	30	900	1000
3	96	700	900
	12	930	1000
4	96	750	900
	12	950	1000

Fig 3.4 Heating cycle used to prepare YBCO powder.

The cycle shown in Fig 3.4 was carried in flowing O_2 in a horizontal furnace. Between each cycle the product was removed from the furnace and ground up. It was then returned to the same alumina dish ready for the next stage in the cycle. The final product was a fine, charcoal coloured powder suitable for pressing into pellets.

When processing bulk YBCO it is desirable to have a fine powder, packed as densely as possible, as small particles in good contact will grow more efficiently with less chance of gas being trapped and voids forming. In order to achieve this end, pellets are cold pressed in a die at a high pressure using the following procedure, illustrated in Fig 3.5. Firstly, the calcined powder is ground for upwards of 10 minutes in order to remove any agglomerations which may have formed. Next, the powder is transferred by small quantities at a time into a die, which has already been plugged and placed into a holder. At several stages during this process the die is "banged down" and turned. This ensures

an even distribution of powder within the die. If this were not the case then an uneven stress distribution would result during pressing, which would lead to cracking and a non-uniform sample. The powder is tamped down before allowing the pressure rod to slide home under its own weight. The die and its holder are then transferred to the press. A cap is placed on the pressure rod to ensure good contact with the press and to protect the rod from damage. The press is then initialised and the pressure slowly increased to 380 Mpa inside the bore of the 0.5 inch die. For the 1 inch die it would be desirable to use the same pressure, but unfortunately 250 bar is the limit of the compressor, hence the pressure within the 1 inch die is greatly reduced. This pressure is held for 1.5 minutes and then gradually reduced to zero. Once the pressing is finished, the die is transferred to a different holder that allows the plug and the pellet to be pushed through it and to drop out from the die. It was necessary to coat the inside of the die with liquid soap in order to prevent damage to the pellet during this stage. The soap used was an organic mixture which burns off during thermal processing and so no contamination results. The average pellet density attained by this method was found to be 1.21 gcm^{-3} for a 0.5 inch pellet.

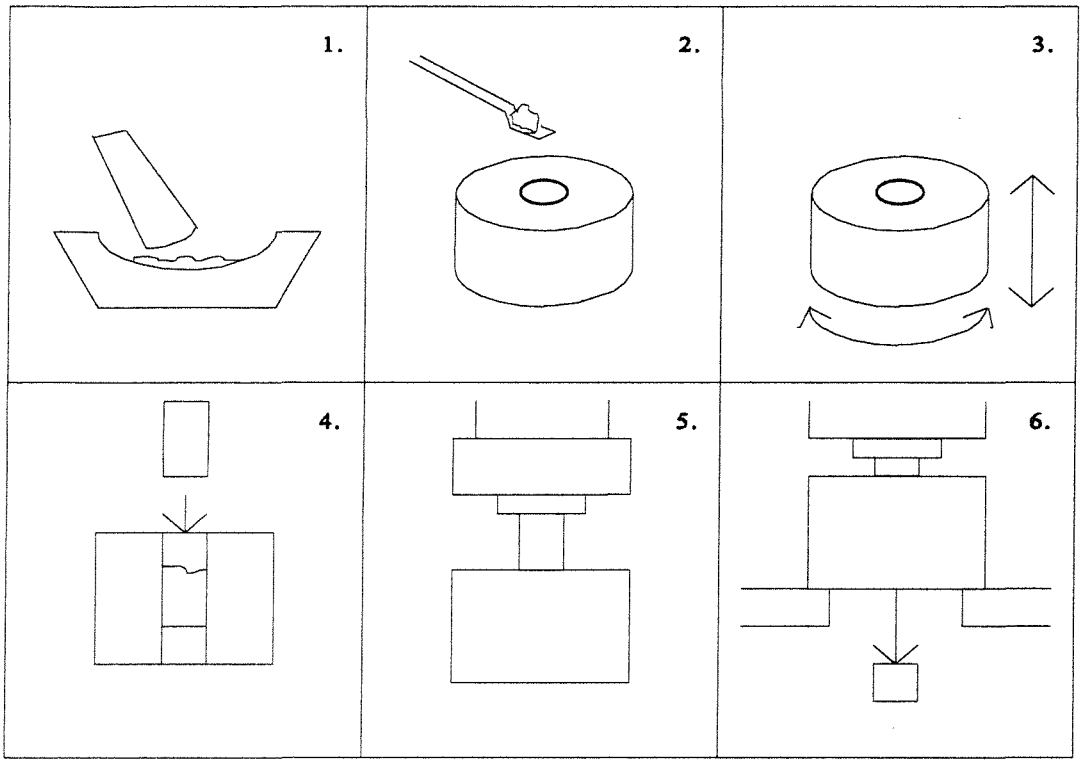

Fig. 3.5 Illustration showing the steps taken during pellet pressing.

3.4 Seed Preparation

Seeds were prepared from a shattered pellet of $SmBa_2Cu_3O_x$ (Sm123). The pellet was produced using an adjusted MTG heating cycle in the same way as a pellet of un-seeded melt textured YBCO would be prepared. Sm123 is ideal as a seed for Y123 because as it has an almost identical perovskite structure and as well as having a slightly higher melting point. This allows the seed to retain its structure whilst the pellet forms a melt. Some Sm123 will be dissolved into the YBCO. When combined with the effects of the cold finger, this results in the region in contact with the seed nucleating first. Thus the grain nucleation and orientation site may be controlled.

Seeds were formed from single grains of Sm123 that had cleaved along their crystal axis (ab plane) when the larger pellet was crushed. Cleaving ensures that there is one flat

surface parallel to the ab plane. The seeds were polished to provide two parallel ab plane surfaces suitable to act as orientated nucleation sites. Sharp edges or protruding features were rounded off. Some seeds were completely rounded off and reduced to a uniform diameter. Before processing, all seeds were cleaned in toluene to ensure that no impurities were present in the interfacial region.

3.5 Melt Textured Growth Process

In order to produce high quality single grains of bulk YBCO it was necessary to find the ideal thermal processing conditions suitable for use with the furnace configuration detailed above. During the development of this procedure, a great deal was learnt about the crystal formation mechanisms and the growth kinetics of this material.

In order to ascertain the ideal temperature at which to initiate melt growth a systematic study was undertaken. In this process 0.5 inch pellets manufactured using the method described above were heated above their peritectic in the furnace configuration illustrated in Fig. 3.3. The samples were then furnace cooled to various temperatures in the region of the peritectic and held there for varying amounts of time. Following this, the samples were quenched i.e. furnace cooled to room temperature. Once cooled the samples were cut from the substrate with a wafering diamond saw and examined. Fig 3.7 shows photographs taken with a low magnification microscope of a sample prepared in this manner.

Before discussing in detail what these examples demonstrate with respect to the nature of the growth process, a few of the more obvious, practical considerations revealed by this study should be examined. Firstly, it was immediately apparent that liquid phase losses which take place during the molten stage of the process, irrespective of the effect this has on sample morphology, cause considerable problems with respect to the re-use of the experimental equipment. During processing the sample would become attached to the

substrate and the substrate would sometimes become attached to the alumina support because of liquid phase migration. If the alumina used to make the support is not dense, high quality material then absorption/reaction with the liquid phase can result in swelling or deformation of the support, resulting in motion of the pellet relative to the cold finger.

Another extremely important consideration is the deformation which takes place during melt texturing of the pellet itself, which can be seen in Fig 3.6. Although the term "melt texturing" is used to describe this process, the sample is never in an entirely molten state i.e. all the compounds present do not become liquid phases. Rather, the system is similar to a weak, water soaked sponge which deforms due to the weight of the liquid it holds. This must be considered when assessing the position and the amount of cooling available from the cold finger. This problem lead to later pellets being sintered at 930°C in air prior to processing. The advantage of sintering prior to processing is that the pellet densifies somewhat and so becomes a stronger sponge, deforming less during processing. The disadvantage of sintering is that, as grains of Y123 with inclusions of Y211 are formed prior to melt growth, there is a tendency for increased ripening of the Y211 inclusions to take place during melt texturing. A similar effect may be achieved by increasing the volume fraction of Y211 phase as this has a higher melting point. However, this would also shift the peritectic of the melt and shift the composition away from the optimal.

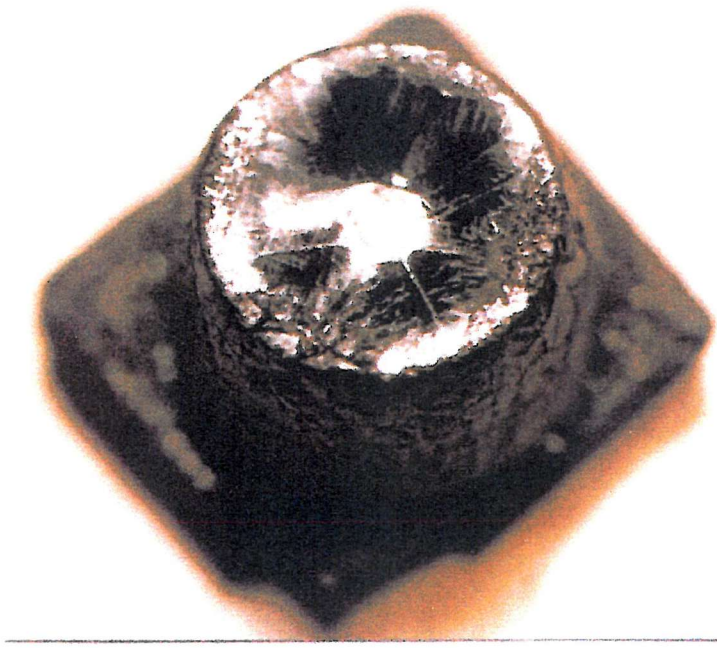

Fig 3.6 Melt grown YBCO pellet illustrating the deformation which can take place during thermal processing.

As described earlier, as part of the investigation into the environment necessary for the production of large, single grain samples of YBCO using the MTG process it was useful to carry out a study which would give us information about the rate of crystal growth at a suitable temperature. With this in mind it was undertaken to produce a range of samples using the following technique:

- First heat the pellets to a temperature in excess of the peritectic to allow the formation of liquid phases.

- Then drop the temperature to an arbitrary temperature in the range of the believed nucleation temperature.

- Next, holding the temperature at this level for various lengths of time to allow for crystal growth to take place.

- Finally, cool the sample at the maximum rate possible to effectively quench any further crystal growth.

This procedure allowed us to find the temperature range suitable as a starting point for growth and facilitated the production samples similar to the one shown in Fig 3.7. This sample clearly illustrates nucleation taking place around the seed area and then crystal growth continuing outward at a uniform rate in all directions. Information gained from these samples allowed the calculation of a perpendicular growth rate of 0.57 mm/hr and a diagonal rate of 0.81 mm/hr. It should be noted that these figures are only really useful in the context of furnace the design being employed here, as the temperature gradients which are applied to the sample will mean that the growth rate will vary throughout the sample.

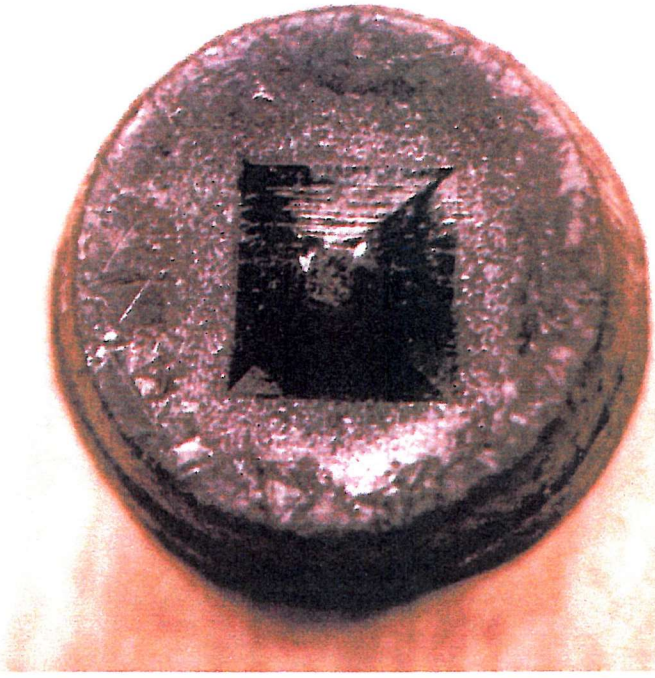

Fig 3.7 0.5 inch diameter quenched YBCO sample illustrating crystal growth rate.

The effects of seed geometry and size were also examined. It became apparent fairly quickly that the larger seeds were more effective than smaller seeds. This could be attributed to the cooling induced by the cold finger having an effect on an area larger than the seed, and so generating independent, randomly orientated nucleation sites. Moreover, observations with extremely small seeds have revealed that the amount of liquid phases absorbed from the molten pellet into the seed is sufficient to dissolve the Sm123 single grain and thus destroy the structure of the seed[10]. This can be seen in Fig 3.8. Whilst the crystal growth does radiate from the seed area, the orientation of the grains is different in each region. It would appear that the temperature gradients across the sample and the thermal cycle were correct but seeding had not forced the growth to occur along the ab plane. As growth started at the seed, this would imply that the ab orientation of the seed had been lost, a fact which was proved when the seed area was polished.

It was also found that the geometry of the Sm123 seeds seemed to have little to no bearing on the success of the process. Since, as previously stated, success was more dependent on the size of the seed, shaping was kept to a minimum so that the dimensions of the SM123 single grain used were as large as possible.

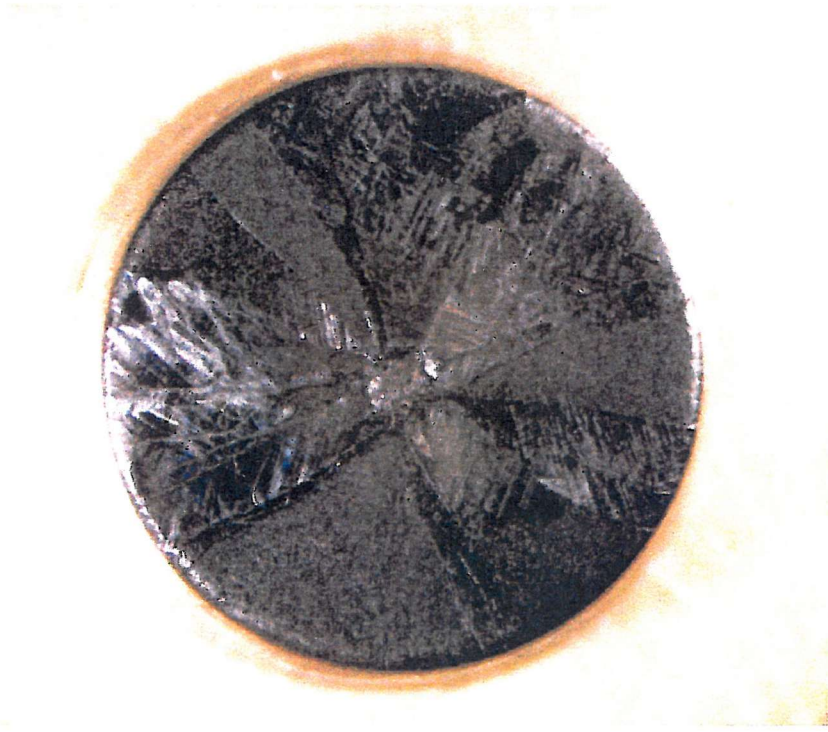

Fig 3.8 0.5 inch diameter YBCO sample illustrating the effect of seed dissolution.

Once the correct temperature region and seeding conditions had been found it was decided to no longer quench the samples, but rather slowly cool them to allow the crystal growth to continue down the sample. One of the problems observed when producing large single grains of YBCO in this way was that during thermal processing the material densifies and gas is evolved. A particularly critical example of this is reproduced in Fig 3.9. It can be seen from the way in which the light is being reflected from the crystal layers that this sample is dominated by a single large grain. However, a large cavity can be observed at the centre of the picture, which has caused the grain to buckle and cracks to form, thus ruining the sample with respect to using the material for experimental measurements.

Modifications to the thermal cycle employed to produce these samples allowed the frequency of this occurrence to be reduced to acceptable levels. It was found that reducing the ramp rate through the region of the phase diagram where the sample first becomes molten allows any gasses to escape and prevents any large voids from being

formed. The rationale behind this is that slowing the ramp rate to 30°C/hr will allow any trapped gas to escape upwards through material which has yet to become molten due to there being a vertical temperature gradient along the length of the pellet.

Another approach which was successful in alleviating this problem but not chosen as a solution was to increase the maximum temperature of the first dwell. This has the effect of reducing the viscosity of the liquid phases, thus easing the process of void filling within the sample. However, it also causes an increase in the amount of liquid phases lost from within the sample during processing, thus shifting the stoichiometry and reducing the amount of good quality material produced [11].

The third approach, not chosen for the same reasons, was to increase the amount of time spent at the first dwell. This allows more time for the liquid to permeate fully throughout the sample, but also allows a greater volume of liquid to be lost.

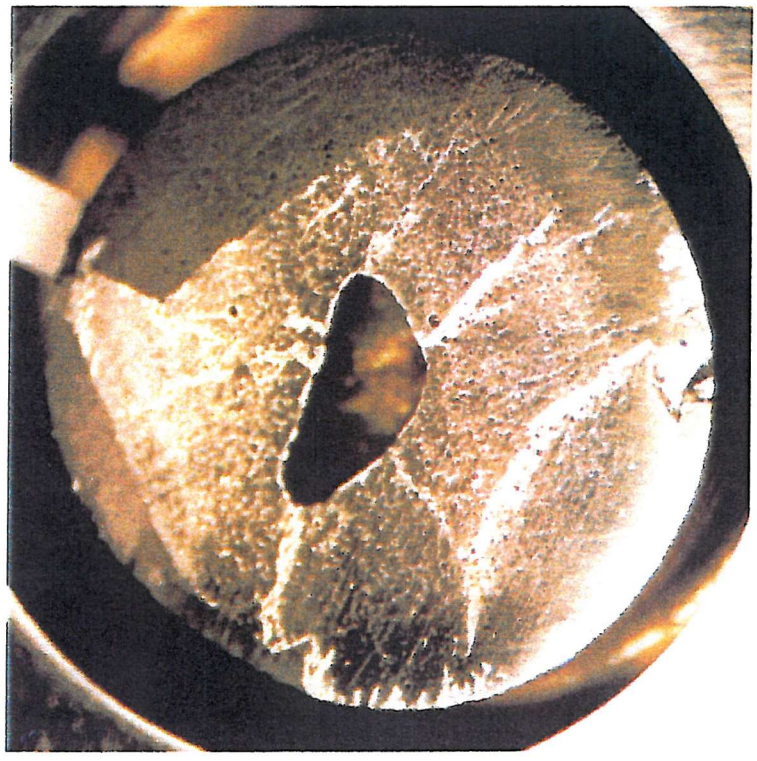

Fig 3.9 0.5 inch diameter YBCO sample illustrating the effects of a cavity.

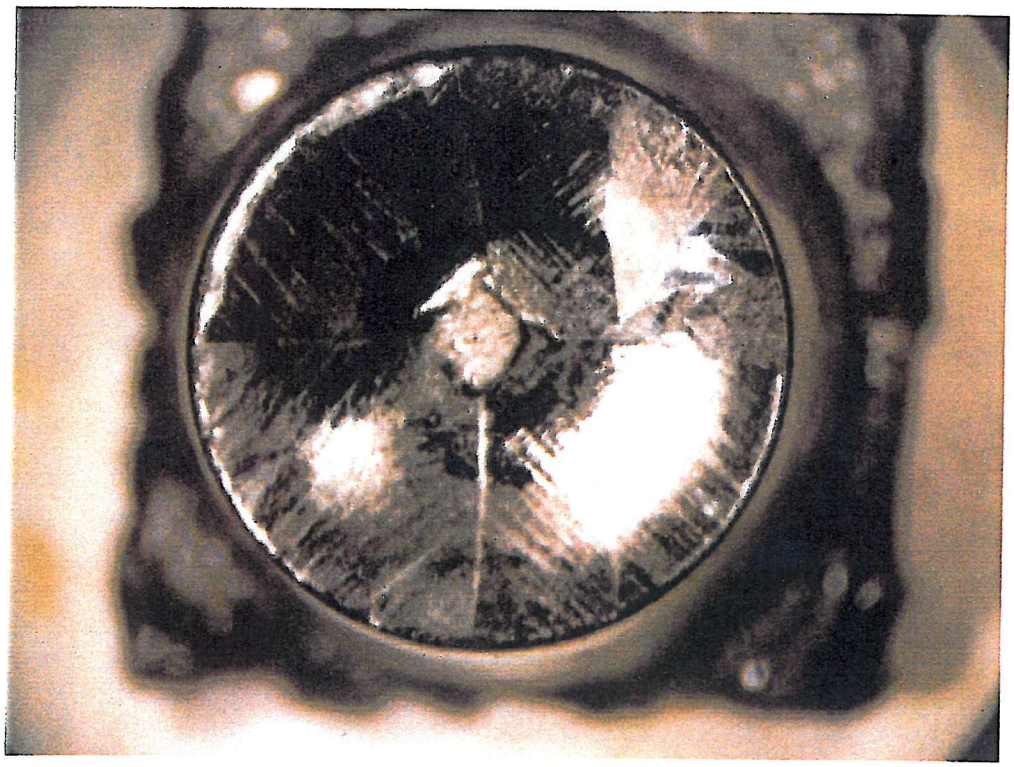

Fig 3.10 0.5 inch diameter MTG YBCO sample with one site of secondary nucleation.

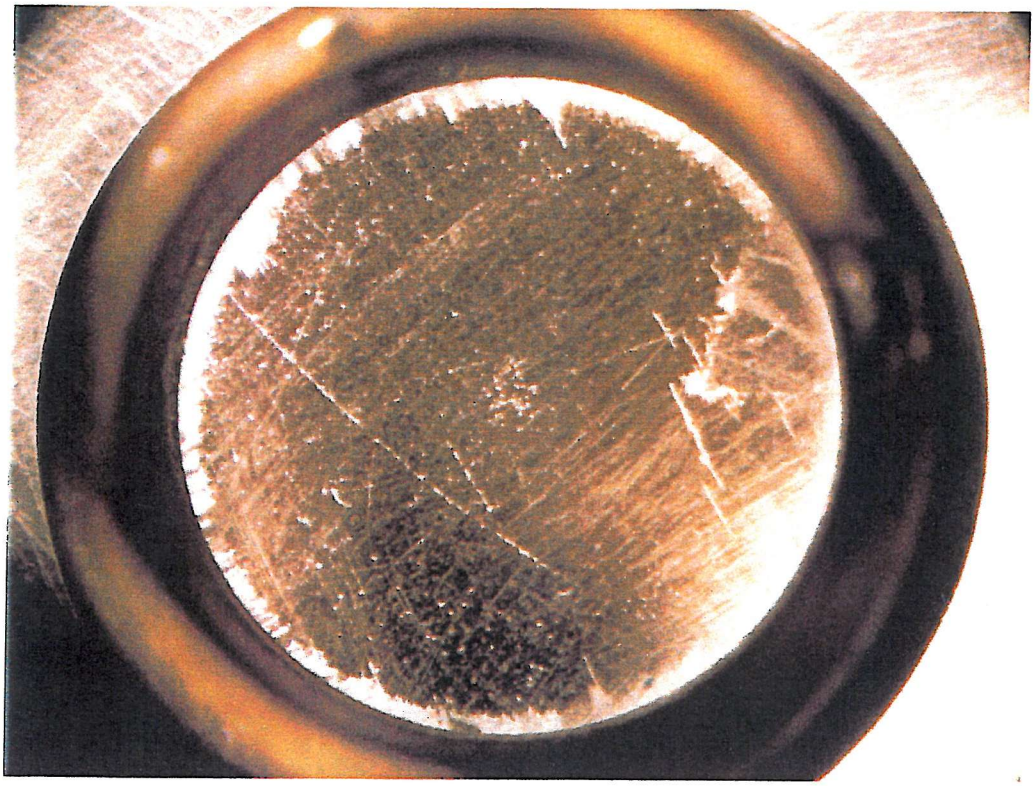

Fig 3.11 Roughly polished surface of the sample shown in Fig 3.10.

Shown in Fig 3.10 is the unpolished surface of pressed, unsintered pellet of MTG YBCO. This pellet displays nearly all of the characteristics one would expect to see in a successfully processed single grain sample of YBCO. Observe the four quadrants corresponding to the a and b lattice directions for solidification radiating from the seeded region at the centre of the pellet. However, as reported earlier, the top surface of the sample has deformed considerably during thermal processing and there appears to be a secondary site of nucleation present in the upper right hand quadrant of the sample.

The effect of these imperfections in the sample can be seen more clearly in Fig 3.11, a photograph of the sample after it has been roughly polished flat. Polishing the sample using a rough abrasive has the effect of tearing away the layers of material allowing the orientation of the crystal structure to be observed with the aid of a light source. In Fig 3.11 the region around the outer edge of the sample and also the region surrounding the secondary grain show up brightly. This illustrates the way in which the layers of the crystal have been deformed or bowed. This phenomenon can be explained around the edges because of the way the top surface of the pellet became curved during processing. The area around the secondary grain will be under considerable strain due to the anisotropic coefficient of thermal expansion present in the YBCO crystal, explaining why the structure displays evidence of deformation. If this sample were to be thermally cycled i.e. during oxygenation or during cooling in liquid nitrogen to below Tc, it would be essential to remove the secondary grain. The forces induced by the expansion/contraction of the misaligned grains would cause cracks to appear, thus ruining the sample and illustrating the importance to any bulk YBCO applications of having single grain material.

It is not immediately apparent why the secondary grain was formed. There may have been an impurity of some sort on the surface of the pellet which acted as a nucleation site. More likely however, is that the curvature of the surface of the pellet was sufficient to distort the temperature gradient across the top surface of the sample to a degree where

nucleation was able to take place away from the seed. It was decided from this and similar results that the uncertainty introduced by the deformation of the pellets was unacceptable. The introduction of the sinter prior to melt growth eliminated this uncertainty.

It is interesting to note that generally the quality of the material in the centre of a pellet is of higher density that that near the edge. This is logical as less liquid phases should have been lost at the centre of the pellet during processing. The exception to this however is the region just below the seed. As can be seen from Fig 3.11, this region shows a noticeably larger degree of porosity even at this low magnification. Fig 3.12 shows a higher magnification polarised optical micrograph of this region after further polishing.

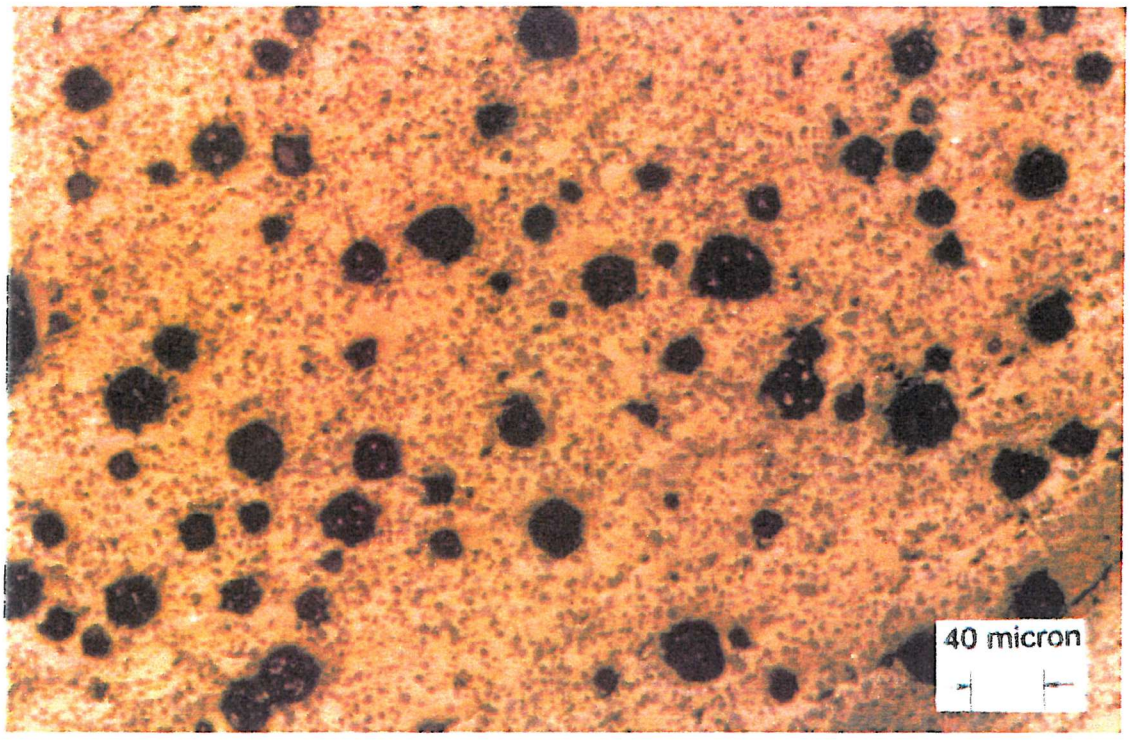

Fig 3.12 Polarised optical micrograph of the region directly under the Sm123 seed of the MTG Y123 sample shown in Fig 3.10.

It has been shown in other studies that the region below the seed displays a reduction in Jc/Tc which has been attributed to diffusion of Sm away from the seed into the YBCO

pellet. Jc will also be reduced in this region because of the increased proportion of Y211 phase present and the higher level of porosity.

The mechanism which causes the increase in porosity is not fully understood but it could be attributed the nature of the seed. The SM123 seeds used in this study were quite porous, as large amounts of liquid phases were lost during the production of the SM123 MTG pellet. It is therefore expected that some liquid phases be absorbed from the molten pellet into the seed.

Shown in Fig 3.13 is a photograph of the top surface of a single grain pellet of YBCO which was successfully produced from a sintered pressed pellet using the furnace design shown above. Again the sample clearly shows the four quadrants formed by the crystal growth fronts and no secondary sites of nucleation can be seen. Also, as a result of pre-sintering the pellet, the top surface shows none of the deformation seen in Fig 3.10.

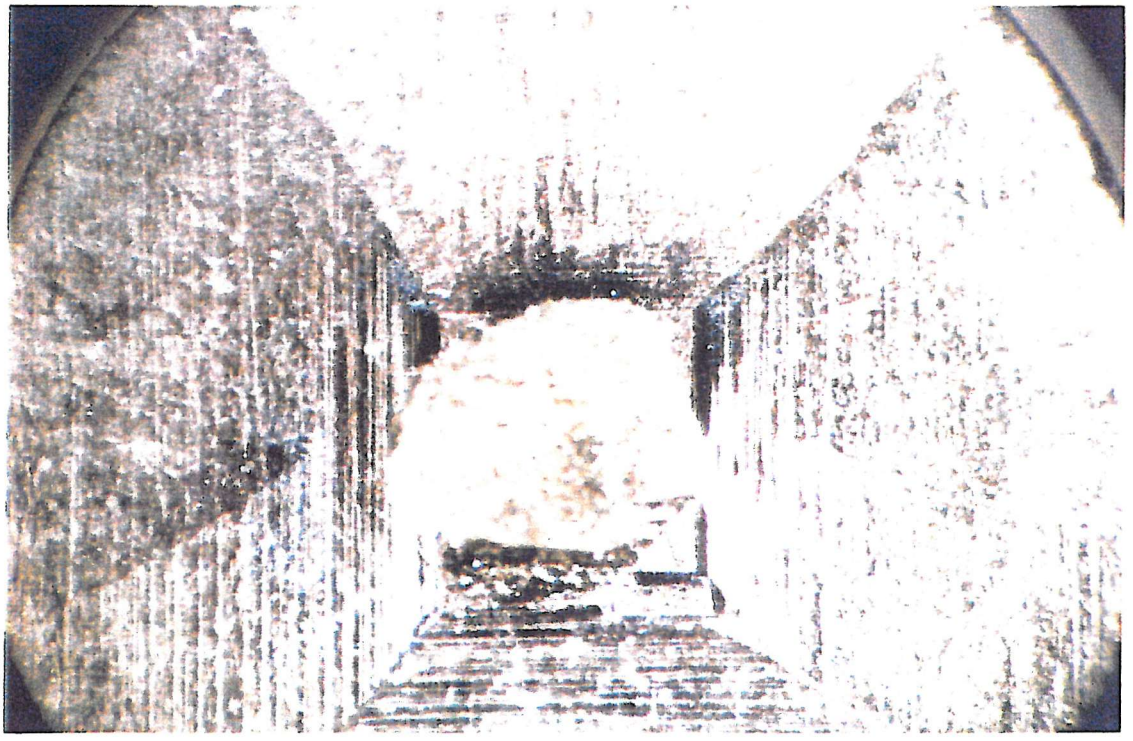

Fig 3.13 Top surface of 0.5 inch diameter single grain YBCO pellet.

The seed used was relatively large and has obviously retained it structure throughout processing. Due to the large size of the seed, the square region which forms around the seed can be clearly seen.

Fig 3.14 is a close up photograph of the region in which one corner of the central square meets one of the outwardly radiating lines which divide the quadrants of the top surface. Although the focus is not uniform due the nature of the surface, it is apparent that the line is in fact a sunken region corresponding to where the two growth fronts meet. The rows of perpendicular lines which meet in this region are also visible variations in the level of the surface. The occurrence of this can be explained in terms of crystal growth process.

The material we see when we examine the surface of an unpolished MTG YBCO sample is a solidified mixture of barium cuprates i.e. the constituents of the liquid phase which reacts with the Y211 to become Y123. When the material is forming, crystallisation will take place in layers, as shown by the different colours in Fig 3.15. As the layers form, the liquid phases will be used up to produce the Y123 bulk It is believed that this is the cause of the striping on the top surface. The square domain surrounding the seed arises from the maximum growth rate being in the a and b directions.

Shown in Fig 3.16 is micrograph of one of the shiny, interfacial regions between the central square and one of the outer quadrants. Just visible on the smooth layers of material are the twin lines. These form in the [100] and [010] directions and so provide verification of the crystal orientation[12].

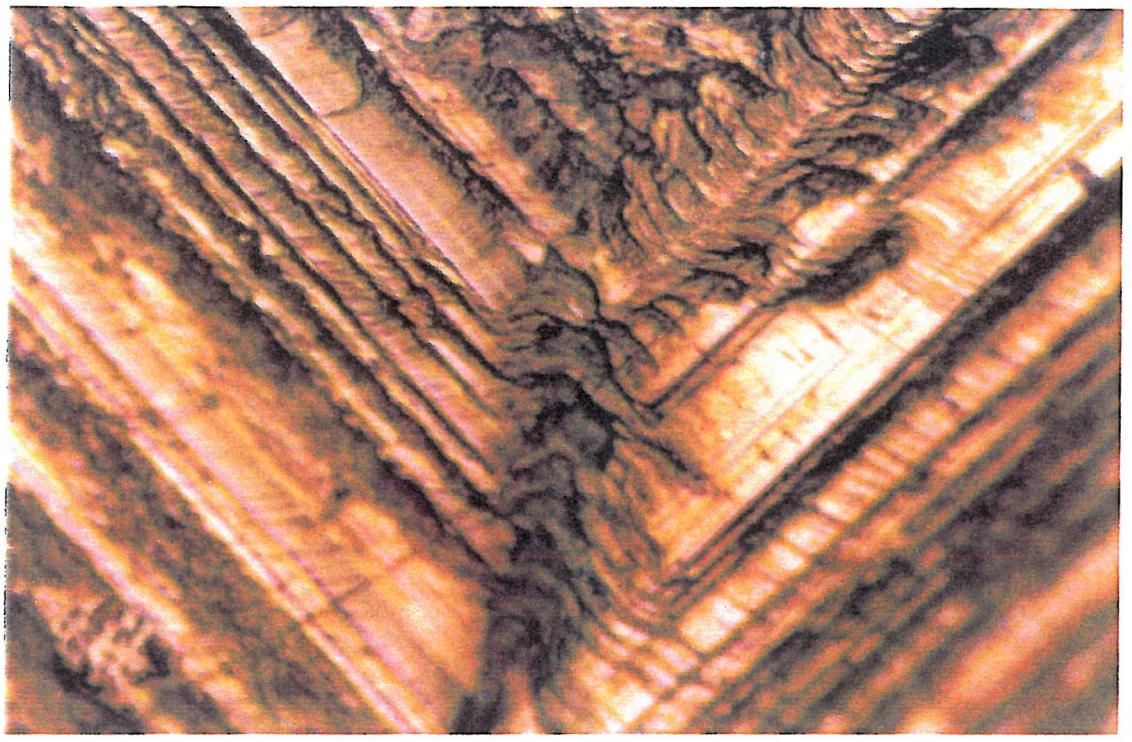

Fig 3.14 Intermediate magnification micrograph showing one of the indentations which divide up the quadrants on the top surface of a seeded MTG YBCO pellet.

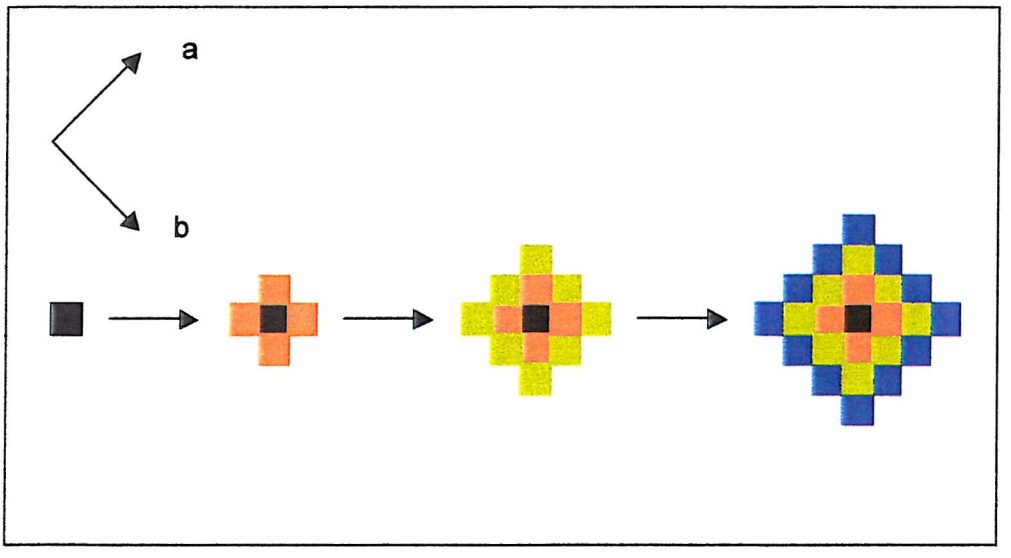

Fig 3.15 Diagram illustrating crystal growth mechanism.

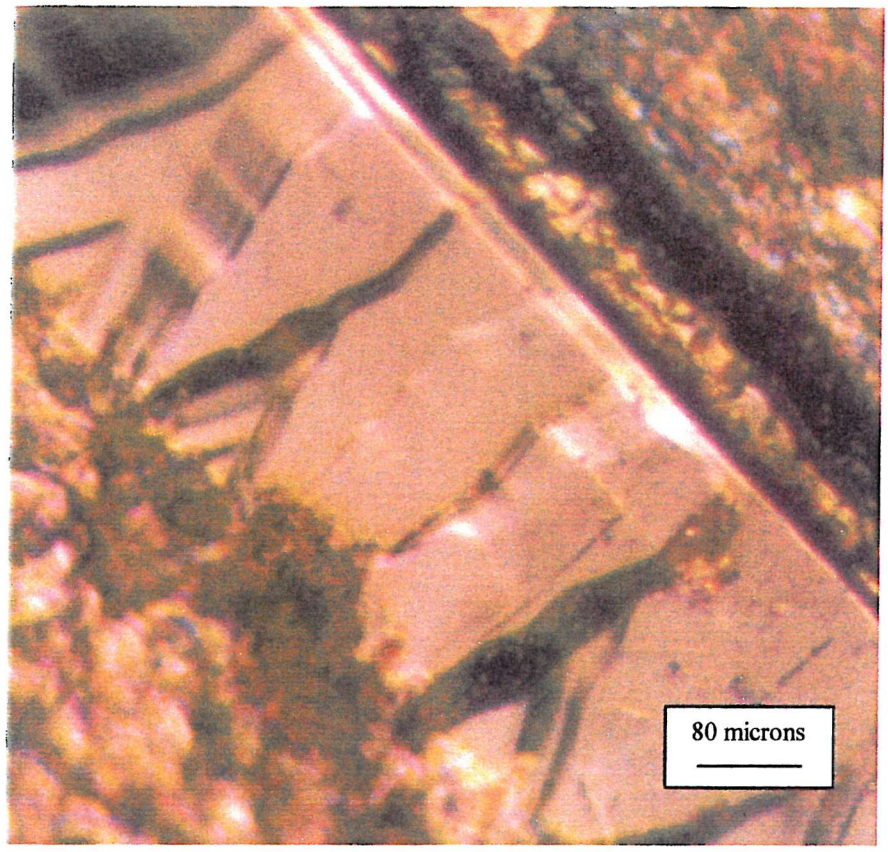

Fig 3.16 Region illustrating orientation of twins.

Shown in Fig 3.17 is a photograph of the outer region of one of the quadrants of the pellet shown in Fig 3.13. The light source has been angled to show a feather like pattern which exists on the surface of the pellet and becomes more prominent as one moves further away from the seed. This feature is still visible after polishing and corresponds to the angle of the ab plane rocking slightly. One inch diameter samples show this characteristic to a higher degree. Literature suggests that this effect becomes more acute in still larger pellets and has the effect of reducing the obtainable critical currents.

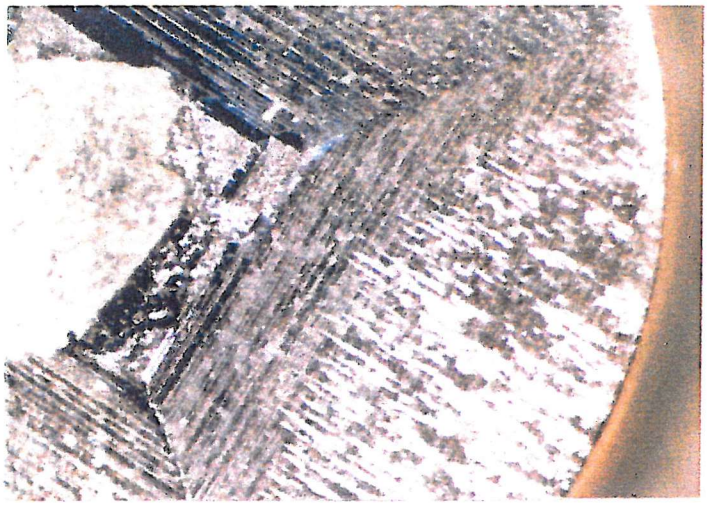

Fig 3.17 Photograph illustrating sample degradation away from the seed.

3.6 Quality Assessment: Observations Using a Scanning Hall Probe

In order to illustrate the absence of any weak links or grain boundaries present in the single grain material prepared in the manner described above trapped field measurements were made using a scanning hall probe assembly in conjunction with the department of Physics, Southampton University. The experimental set-up used to scan the samples is shown schematically in Fig 3.18.

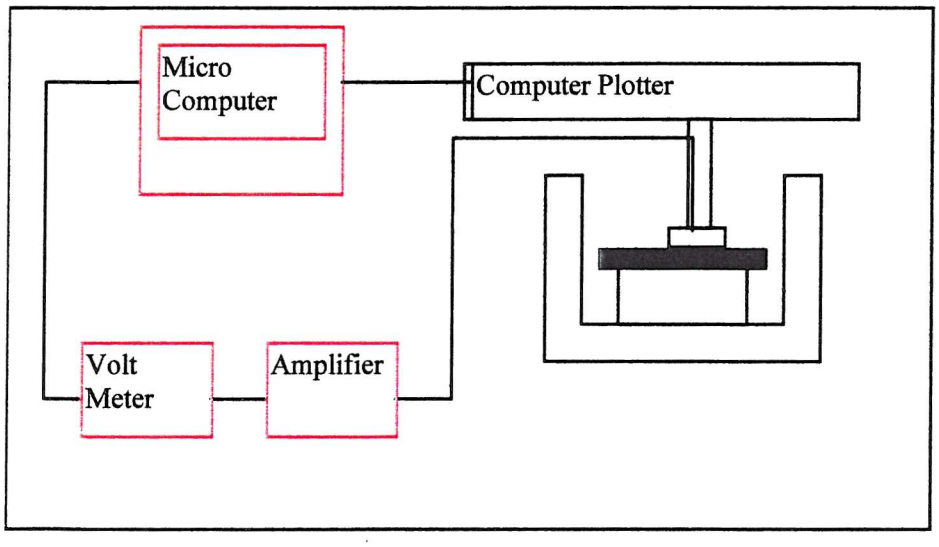

Fig 3.18 Schematic of scanning Hall probe experimental apparatus.

Fig 3.18 illustrates how the sample (shown in black) is kept in a nitrogen bath whilst an inverted computer plotter moves a Hall probe across its surface. The Hall probe used has a spatial resolution of 0.1 mm and a sensitivity of 10^{-5} T. Its response is 53 μV/mT at a current of 100 mA. The active area is 0.1×0.1 mm^2. Samples were field-cooled in an applied field of 0.24 T. The hall probe was then lowered to a distance of approximately 0.4 mm above the surface of the sample. Scans took between 2 to 3 hours depending on the size of the sample.

Due to the long duration of the experiment a control measurement was carried out so that the effects of flux creep during the scan could be accounted for[13,14]. The plot shown in Fig 3.19 shows the amount of relaxation along one path across the ab surface. It is apparent from this that there is minimal loss in magnetisation. If the Gaussian spread one would expect from a repeated measurement like this is ignored then there is a maximum of an 8% reduction in the measured field over 3 hours. The real figure is likely to be considerably less than that and so for the qualitative nature of this experiment, the relaxation is not a factor which needs addressing.

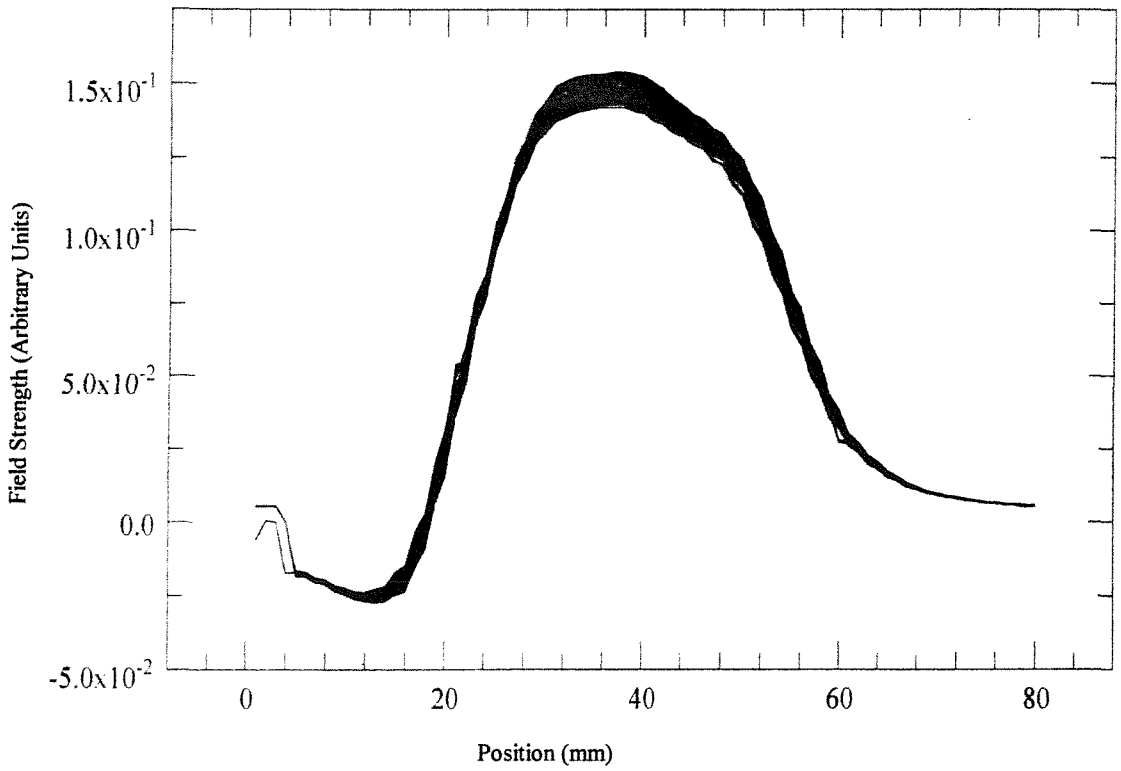

Fig. 3.19 Plot to illustrate the consistent nature of the measurement over a 3 hour period.

Fig 3.20 is a plot of the MTG pellet photographed in Fig 3.21. It is obvious from the photo that this pellet is multi-grain. From the field scan it is immediately apparent that the grain boundaries do not allow large inter-granular currents and so the single pellet is acting like several smaller pellets, each of which is separately magnetised and obeys the Bean model. Fig 3.22 is a contour field plot of a pellet which, from optical observations, would appear to be single grain. The field scan reveals no weak links or grain boundaries and illustrates beautifully the way a single grain sample differs in characteristics from a multi-granular sample. It is obvious from the number of field contours that the single grain sample is capable of trapping a much larger field than the multi-grain sample. In this instance the single grain sample displays a maximum field of almost four times that of the multi-grain pellet, even though the single grain sample is half as thick If we use the standard Bean model and only use the steepest region of field gradient in the calculation we get J_c equal to 3.64×10^4 Acm^{-2}.

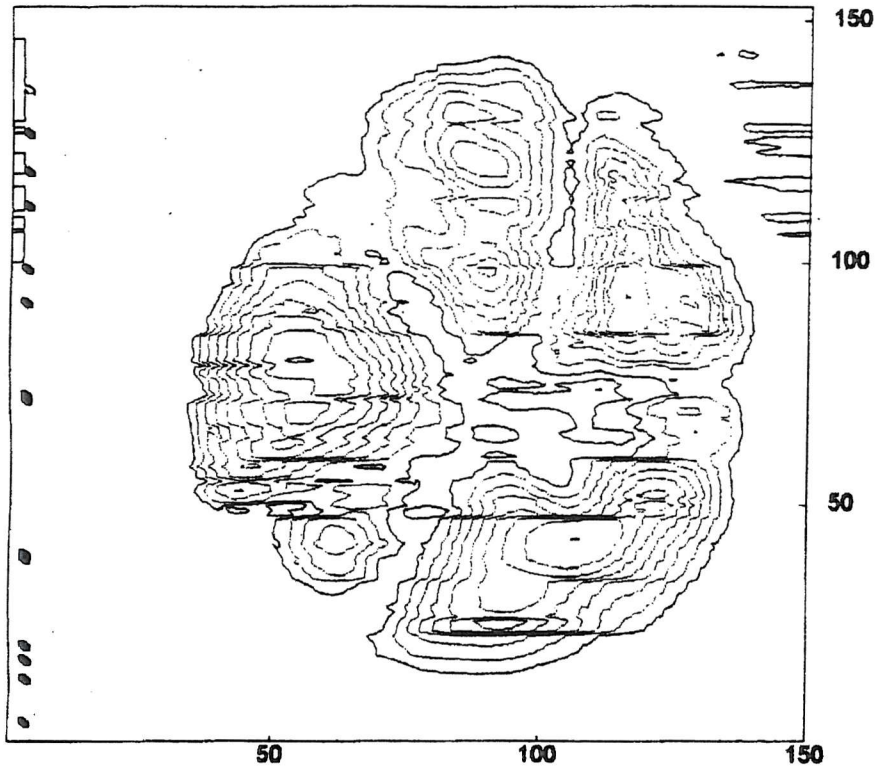

Fig 3.20 Hall probe scan of multi granular sample.

Fig 3.21 Photograph of the polished multi grain sample used in Fig 3.19

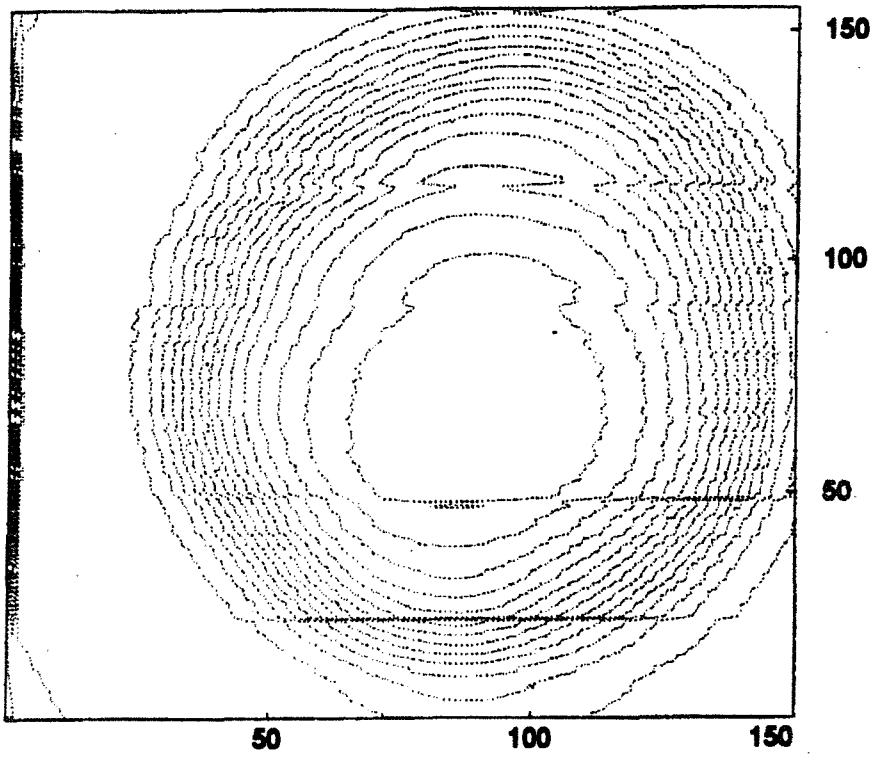

Fig 3.22 Scanning Hall probe measurement of single grain YBCO pellet.

3.7 Conclusion

A system has been constructed to produce large, single grain monoliths of YBCO using the seeded MTG method. The development of this processing environment has provided a great deal of information pertinent to the crystal growth of bulk YBCO. The evidence indicating the successful production of single grain material has been presented and the absence of weak links in the material has been proved using scanning Hall Probe measurements.

Single grain samples of up to one inch in diameter were successfully produced using this furnace design and processing technique. There is no reason why larger samples could not be produced using a similar configuration to this. However, as the quality of the

sample seems to degrade relative to the distance away from the seeded region due to the rocking effect discussed above, the value of producing ever larger samples in this way is questionable. An alternative to growing larger monoliths of YBCO is presented in Chapter 7.

3.8 References

1. S. Jin, T.H. Tiefal, R.C. Sherwood, M.E. Davis, R.B Van Dover, G.W. Kammlott, R.A. Fastnacht and H.D. Kieth, *Appl. Phys. Lett.*, **52**, 2074 (1988)

2. S. Jin, T.H. Tiefal, R.C. Sherwood, M.E. Davis, R.B Van Dover, G.W. Kammlott, R.A. Fastnacht and H.D. Kieth, *Phys. Rev.*, B**37**, 7850 (1988)

3. M. Morita, S. Takebayashi, M. Tanaka, K. Kimura, K. Miyamoto and K. Sawano, *Adv. Supercond. Sci. Technol.* Vol. **3**, 733 (1991)

4. W. Lo, D. A. Cardwell, C. D. Dewhurst and S. -L. Dung, *J. Mater. Res.* Vol. **11**, 786 (1996)

5. S. Marinel, J. Wang, I. Monot, M. P. Delamare, J. Provost and G. Desgardin, *Supercond. Sci. Technol.* Vol. **10**, 147 (1997)

6. W. Lo, D. A. Cardwell, S. –L. Dung and R. G. Barter, *J. Matter. Sci.* Vol. **30**, 3995 (1995)

7. D. Shi, D. Qu, S. Sagar and K. Lahiri, *Appl. Phys. Lett.* Vol. **70**, 3606 (1997)

8. R. L. Meng, L. Gao, P. Gautier Picard, D. Ramirez, Y.Y. Sun and C.W. Chu, *Physica C,* vol. **232**, 337 (1994)

9. K. Ohtsu, Y, Yamada, T. Izumi, Ynakamura and Y. Shiohara, *J. Mater. Res.* Vol. **11**, 1094, 1996.

10. Y. Jee, G-W Hong, C-J Kim, *IEEE Trans. Appl. Supercond.* Vol. **9**, No. 2 (1999)

11. C. Varanasi and P.J.McGinn, Journal of Electronic Materials, Vol 22, No. **10**, (1993)

12. P. Gautier-Picard, E. Beaugnon and R. Tournier, *Physica C*, **276**, 35-41 (1997)

13. Y. B. Kim, C. F. Hempstead and A. R. Strand, *Phys. Rev.*, **129**, 528 (1963)

14. P. W. Anderson, *Phys. Rev. Lett.* **9**,309 (1962)

Chapter 4: Improved Microstructure in Melt Textured YBCO Via a Novel Powder Preparation Technique.

4.1 Introduction

As discussed in chapter 2, the superconducting properties of melt textured YBCO are not intrinsic to the compound, rather they are highly dependent on the microstructure of the given sample. For this reason it is extremely important to understand the processes which take place during melt processing, and how the thermal cycle, stoichiometry and the presence of dopants effect the final microstructure[1-3]. In this chapter the nature of flux pinning is discussed and the mechanisms which take place during processing are examined. In addition, various methods for the production of materials with improved microstructures are presented and compared.

It has been shown by various authors[4] that there are many microstructural features which affect the flux pinning and hence Jc of bulk YBCO. These can be grouped into four categories of pinning mechanism:

1. Core pinning. This mechanism encompasses phenomena such as δTc, $\delta\kappa$ and precipitate pinning[5]. This is the most common type of pinning in which a portion of the condensation energy losses due to having a region of depressed order parameter within the normal core can be regained by locating the normal core in a region where the order parameter is naturally suppressed. δTc pinning is attributed to local variations in the order parameter arising from regions having a lower Tc when compared to the surrounding bulk. $\delta\kappa$ pinning is associated with local variations in the superconducting length scales λ_L (also known as magnetic pinning) and ξ, which can be related to the presence of features such as defects and twin planes. Lastly, precipitate pinning is derived from the

partial or complete suppression of the order parameter due to the presence of compositionally distinct non-superconducting inclusions within the bulk.

2. Elastic Pinning. There are two types of elastic pinning; parelastic and dielastic[6]. Both are derived from the small expansion in volume and the small changes in elastic constants associated with the normal to superconducting phase transition. The parelastic mechanism is a first order elastic interaction between the strain field caused by the normal core and the stress field of a crystalographic defect, for example a dislocation. The dielastic interaction is a second order interaction resulting from the dependence of the self energy of a defect on the elastic constants of the medium. A force will result as the normal core is stiffer than the surrounding bulk. However, consideration of this force alone would predict a repulsive vortex-defect interaction.

3. Collective Pinning. Collective pinning is a phenomena which arises from the tendency of vortices not to act individually, but rather move cooperatively due to their repulsive interactions[7,8]. This can be understood by considering the Abrikosov lattice described in chapter 1. If a completely rigid lattice were to interact with a random distribution of pins then there would be no net pinning force as free energy cannot vary with position. However, if the condition for perfect rigidity is relaxed and fluxons are allowed to locally to compress, shear or tilt then the lattice as a whole may be pinned.

4. Surface Pinning. The sample surface may be considered as a pinning site as there exists an energy barrier for flux to enter or exit the sample. This barrier, called the Bean-Livingstone surface barrier[9], is modelled by the superposition of an attractive potential of a vortex and its mirror image anti-vortex and a repulsive term due to surface currents (see Fig 4.1).

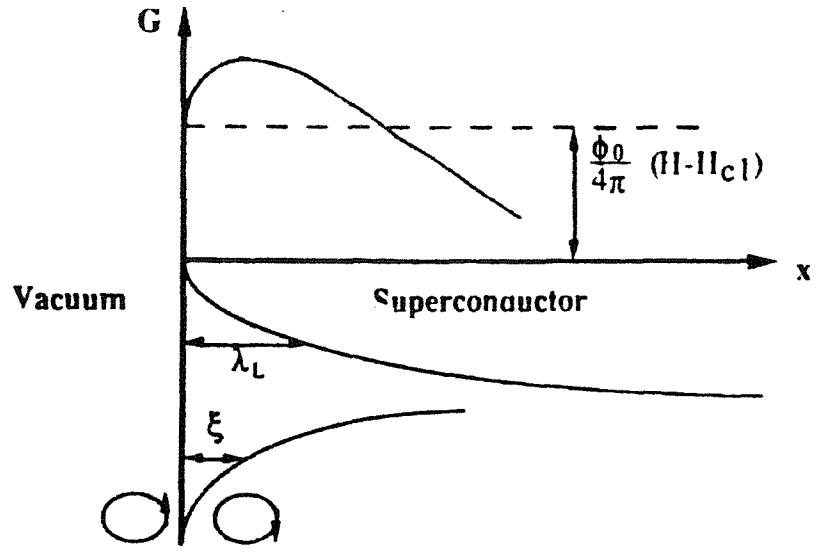

Fig 4.1 Surface barrier to penetration of flux into an equilibrium type II superconductor showing the spatial variation of the Gibbs free energy relative to the superconductor-vacuum interface.

From the definition of these mechanisms it can be seen that the main way in which the pinning of a given material may be controlled is by the introduction or enhancement of the core pinning within the bulk. From considering the elementary pinning force density, f_p, which is defined as the local pinning force associated with the local variation in the order parameter, a simple relationship reveals the nature of the most effective pinning centres. This is shown in eq.1;

$$f_p \propto \frac{dU}{dx} \propto \frac{U_0}{r_p} \qquad \text{eq.1}$$

where U_0 is the depth of the pinning potential well and r_p is the range of the pinning potential. The value of U_0 is sensitive to both the type pinning centre and the given material. r_p, the range of the pinning potential, can be approximated to the coherence length, ξ, which is again defined by the material. From this we can imply once the dimensions of a pinning centre exceed ξ, there is no longer any benefit from increasing

volume. Therefore it can be said that a high number density of fine pinning centres will be more effective than the same volume fraction distributed in larger volume inclusions.

4.2 Powder Production and Experimental Procedure

Shown in fig.4.2 is the pseudo binary phase diagram for the YBCO system. It can be seen that for all temperatures above 1015 °C the 123 phase decomposes into 211 and liquid phases. As described in chapter 2, it is in this region during melt processing that Y211 inclusions can form and ripen[10]. It can also be seen in fig.4.2 that at temperatures above 1200°C the Y211 decomposes, giving a mixture of liquid phases and Y_2O_3. It is this region of the phase diagram which is exploited in the Plasma Melt Quench powder preparation technique.

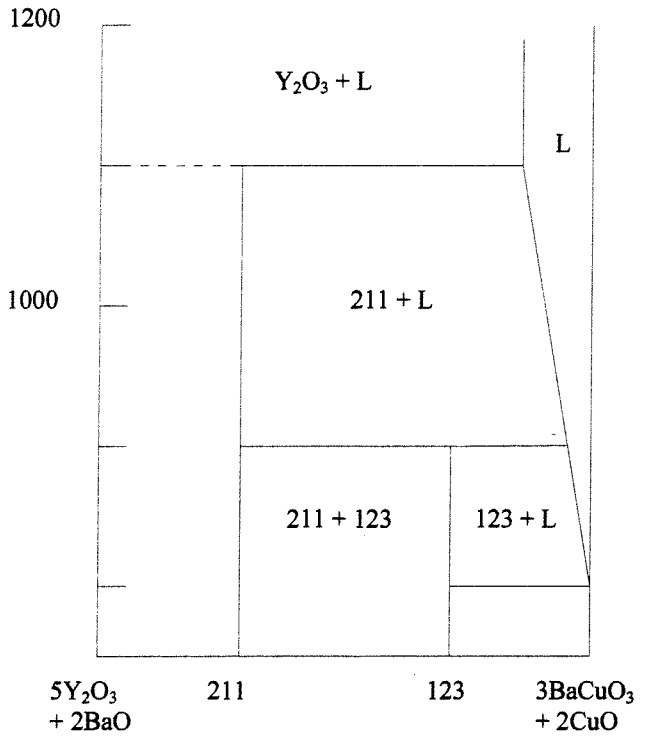

Fig 4.2 Pseudo-binary phase diagram for YBCO

In this process a stoichiometric mixture of Y123 powders is inserted into a plasma spray, which is at temperature in excess of 15,000 °C. This atomises the constituents of the mixture, thus decomposing any already formed 123 or 211 phases present. This mixture is sprayed onto a rotating copper cylinder. The cylinder has a large enough thermal mass so as to allow a considerable amount of powder to be quenched in this manner without a large degree of heating taking place. Once the cylinder is fully coated the powder is collected in the form of flakes. In order to retain the purity of the powder the flakes are not scraped from the cylinder as this could result in contamination arising form either the copper cylinder or the implement used to remove the powder. Instead the powder was removed by striking the cylinder with a heavy, padded implement. The vibrations arising from the impacts were sufficient to dislodge the coating and allow its collection. The powder was then stored in a vacuum chamber without grinding until it was used for processing bulk YBCO. The reason grinding was not carried out prior to usage is because powder produced in this fashion is extremely reactive. Hence, as grinding increases the surface area in contact with the atmosphere, it would seem counter productive to do so.

It was intended that the powder resulting from this process would be an amorphous phase consisting of a mixture of barium cuprates with a fine, even distribution of Y_2O_3 particles throughout[11]. Evidence for this was provided by X-ray crystallographic study which revealed the absence of any detectable crystal structure.

Once the melting point of the 123 phase has been exceeded 211 will begin to form and ripen. During the growth process it has been shown that in order for 123 phase to grow it is necessary for 211 phases to be dissolved by the liquid phases. Therefore during the solidification process Y211 inclusions will reduce in size as the growth front approaches. If the inclusions are not entirely dissolved then the remaining material will be trapped within the 123 bulk. In a standard melt growth cycle using ordinary powders the 211 particles will nucleate randomly. This tends to result few nucleation sites, which ripen into large inclusions. As the number density of inclusions is low, each inclusion will need to provide large amounts of material for 123 phase growth. Therefore there is a greater

tendency for the smaller inclusions to dissolve completely, a fact which is exacerbated when one considers that the larger surface area to volume ratio found for smaller particulates means that they will dissolve more readily. The case for the PMQ powder differs considerably. Initially there is a fine distribution of Y_2O_3 spread evenly throughout an amorphous matrix of barium cuprates. The Y_2O_3 particles not only provide the material necessary for the production of Y211 but also act as nucleation sites. Because there is an already formed distribution of condensation sites the tendency for large scale, inhomogeneous nucleation and ripening is greatly suppressed. Instead, the resulting distribution of Y211 inclusions should mirror the initial distribution of Y_2O_3 particles. As there should be a high number density of uniformly small Y211 inclusions spread evenly throughout the melt the amount of ripening and dissolution should be similar for all inclusions, thus the removal of small inclusions may be avoided. Also, as the high surface to volume ratio of the inclusions allows a faster transfer of material, the crystal growth rate will be larger. This is important as in the melt texturing process a great deal of degradation and inhomogeneity of superconducting properties can result from liquid loss during thermal processing.

The common feature of most of the powder preparation techniques described in chapter 3 is that Y211 phase is allowed to form prior to melt processing. This means that as soon as a temperature in excess of the melting point of Y123 is reached, ripening of the Y211 inclusions will begin. This has been illustrated by many authors, in particular Murikami et al have demonstrated, using electron microscopy to study samples quenched from 1100°C, that different powder compositions produce different formations of Y211 during ripening[12].

4.3 Sample Preparation

PMQ powder prepared in the manner described above was used to produce melt textured YBCO in the following manner. Firstly, flakes of powder were removed from the vacuum container and ground using various regimes in either a pestle and mortar or a ball mill. At this stage some powders were doped with 0.5 %wt. platinum and thoroughly mixed. Samples were prepared ready for melt texturing by being formed into pellets using a uni-axial cold press. In order to maximise the number of individual melt textured samples produced from a small amount of available powder, pellets were prepared using a 5mm diameter die. This allowed 7mm high pellets to be prepared from 0.6g of powder. The pellets were pressed for 90 seconds producing a pellet of density 70% of the theoretical.

As in this experiment the intention is not to produce large single grains of Y123, rather to produce grains suitable for microstructural study, there is no necessity for the strictly controlled temperature gradients discussed in chapter 3. In fact, as a temperature gradient would cause preferential nucleation and directional solidification the resulting microstructure would be more inhomogeneous than that of a sample prepared with no gradients. For this reason a furnace configuration was used which was designed to provide a homogeneous temperature distribution. Fig 4.3 illustrates this arrangement schematically. The alumina plates shown positioned above and below the sample act as radiation baffles, thus providing a more homogeneous temperature profile for radioactive transfer and eliminating the possibility of horizontal temperature gradients across either the top or bottom surfaces of the pellet. The pellet is supported by a substrate fabricated from yttria stabilized zirconia. The size of the substrate and the area in contact with the bottom of the pellet are kept to a minimum so as to discourage liquid loss. The pellets have fabricated with a large height to width ratio for this same reason.

All samples were processed in this manner, in the same furnace, in an atmosphere of air. After thermal processing samples were cut from the substrate using a wafering diamond

saw. Samples were then prepared for optical examination using polishing wheels impregnated with diamond polishing compounds, the grade of which is varied from 14 micron down to 1 micron.

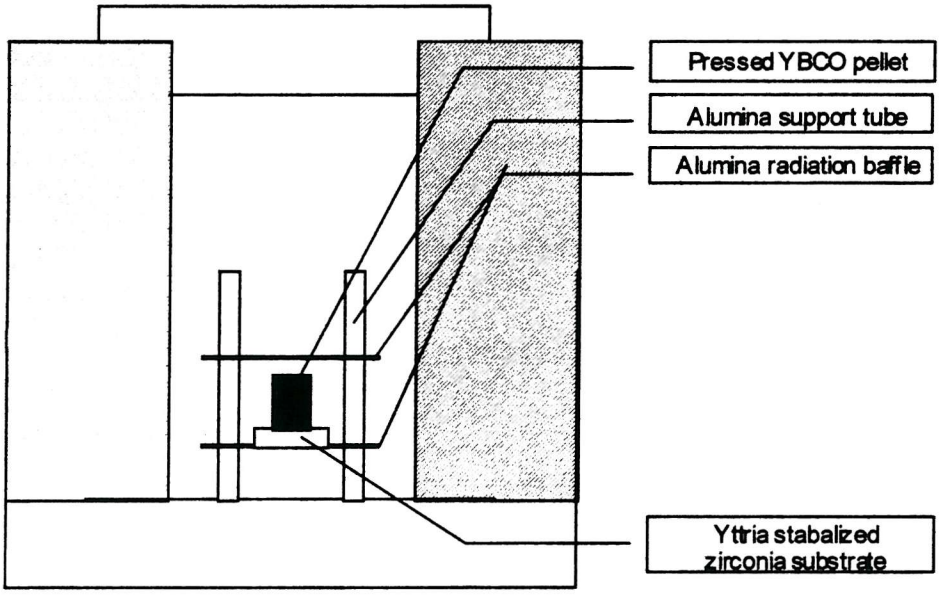

Fig 4.3 Furnace configuration used to process all samples.

4.4 Examination of Microstructure

Show in from Fig 4.4 to Fig 4.11 are a range of polarised optical micrographs illustration the microstructure of various melt textured YBCO samples which have been prepared with a range of stoichiometries and thermal cycles. Fig 4.12 is a table of the corresponding thermal cycles of each pellet examined.

It is immediately apparent when one compares Fig 4.4, a polarised optical micrograph of a sample prepared using standard stoichiometric Y123 powder, and Fig 4.5, a sample prepared using an identical thermal cycle from the PMQ powder, that the material produced from this powder possess a greatly enhanced microstructure with respect to the presence of extremely fine inclusions of Y211 particles. The difference in the morphology and distribution of the Y211 inclusions is considerable. The mean diameter of the Y211 particles in the sample prepared using standard powders is around 5-6 microns, whereas that of the sample produced from the PMQ powder is less than 1 micron.

It may also be observed that the samples produced from the PMQ powders exhibit clustering of the extremely fine particles of Y211 found within the Y123 matrix. It is not known why this clustering occurs. It is possible that there may be an inhomogeneity in the composition of the starting powder causing this, or maybe these regions correspond to a higher concentration of platinum within the melt, although this is unlikely as the same formations are not observed in doped samples prepared from conventional powders.

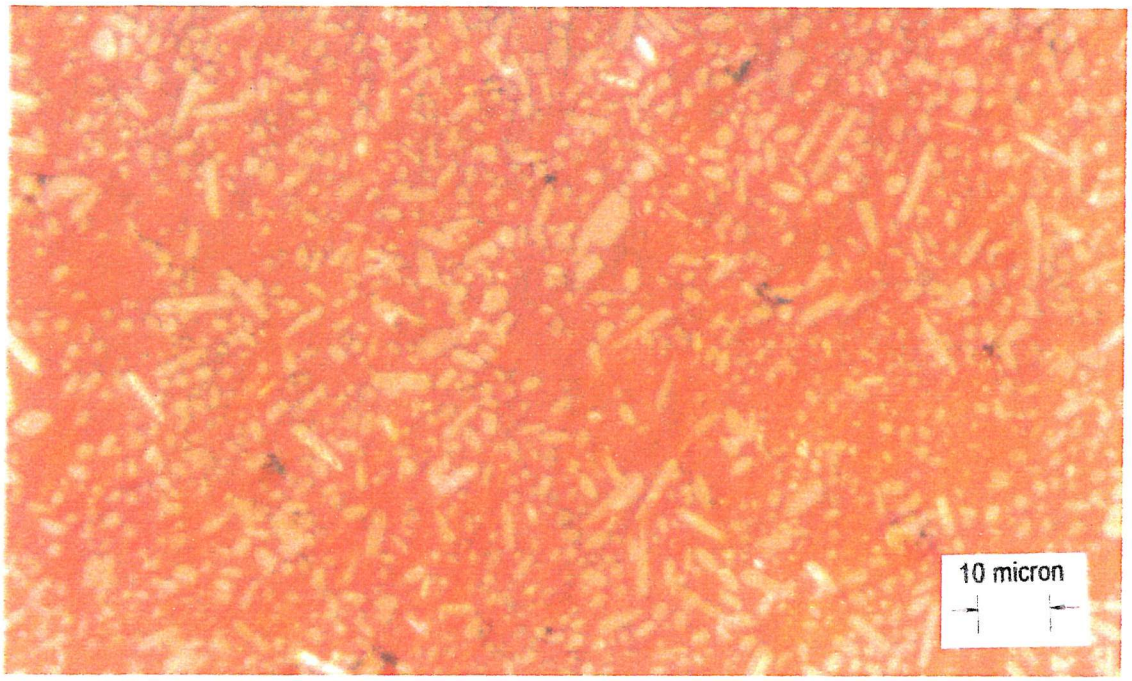

Fig 4.4 Y211 phase distribution found in a sample prepared using conventional starting powders.

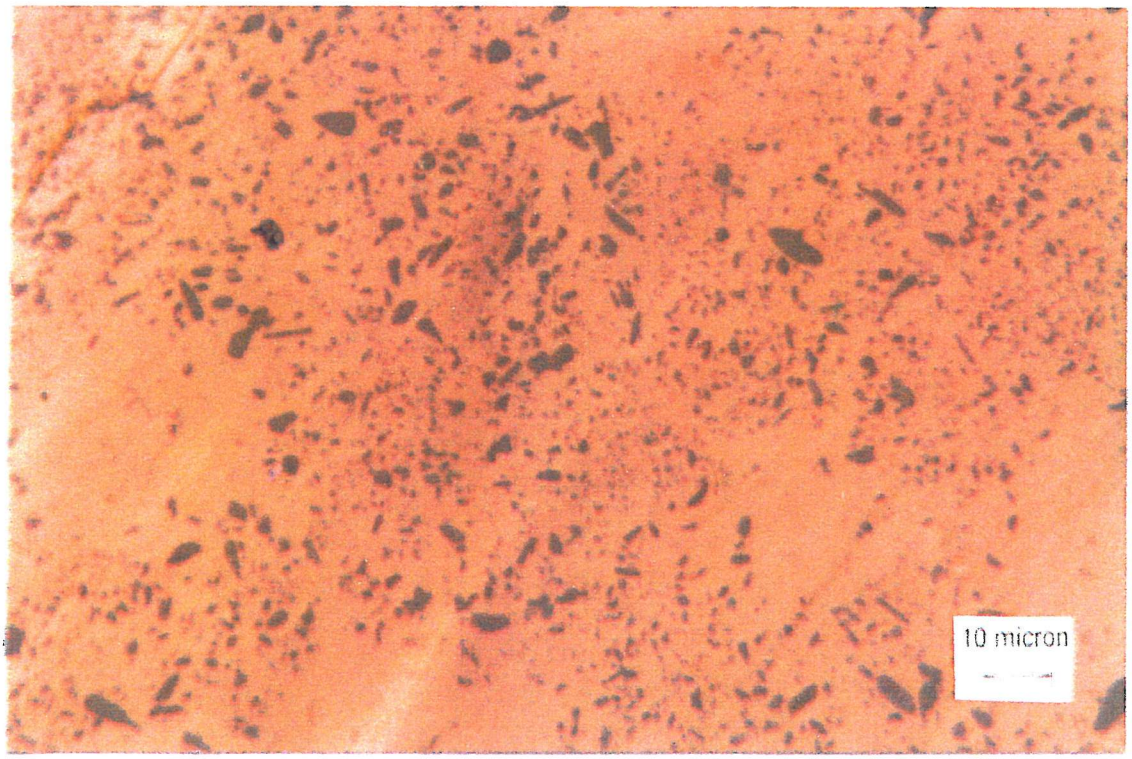

Fig 4.5 Y211 phase distribution found in sample 1 prepared from PMQ powder.

Considering the material produced from the PMQ independently, several interesting features are apparent from microstructure observations. Firstly, let us compare a sample prepared from powder which has been removed from vacuum storage, briefly ground in a pestle and mortar, and then used for pellet preparation (Fig 4.5), with a sample fabricated from powder removed from vacuum storage, thoroughly ground in a ball mill in ether for in excess of 5 hours and then used for pellet preparation (Fig.4.6). The microstructure of the resulting samples of bulk material display a high degree of similarity. However, close examination reveals that in fact the material which has not been ball milled is slightly superior. The reasons for this can be explained as follows. Firstly, as the seed particles for the growth of Y211 are extremely fine and evenly distributed to begin with, excess grinding does not noticeably reduce their diameter or increase the homogeneity of their distribution. Secondly, as the phases present in the PMQ powder are extremely reactive, grinding and exposure to the atmosphere will allow some reactions to take place prior to processing, thus introducing impurities and coarsening of the Y_2O_3 particles. Thus the amount of grinding necessary is that sufficient to allow the powder to be densely packed during pellet preparation.

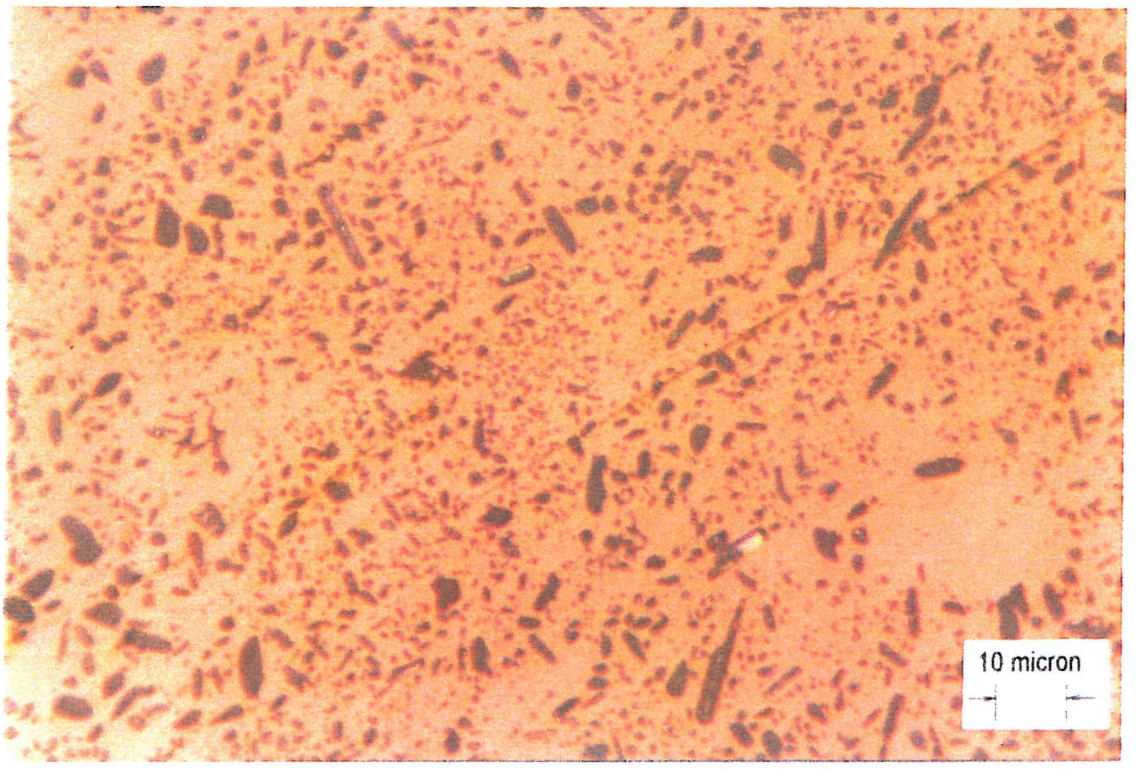

Fig 4.6 Y211 phase distribution found in sample 2 prepared from PMQ powder.

Illustrated in Fig.4.7 is an intermediate magnification micrograph showing the microstructure of a PMQ sample on a larger scale. One may observe from this that the density of Y211 displays some inhomogeneity. There are a large number of circular regions visible through out the bulk where the density of Y211 inclusions is greatly reduced.

A higher magnification micrograph of one of these regions is given in Fig 4.8. It has been observed that these regions in some instances may be completely devoid of Y211. However, in other examples same Y211 inclusions are present near the centre of the region. These inclusions are of a different geometry to the inclusions seen elsewhere within the bulk. They take the form of extremely fine rods or whiskers of Y211.

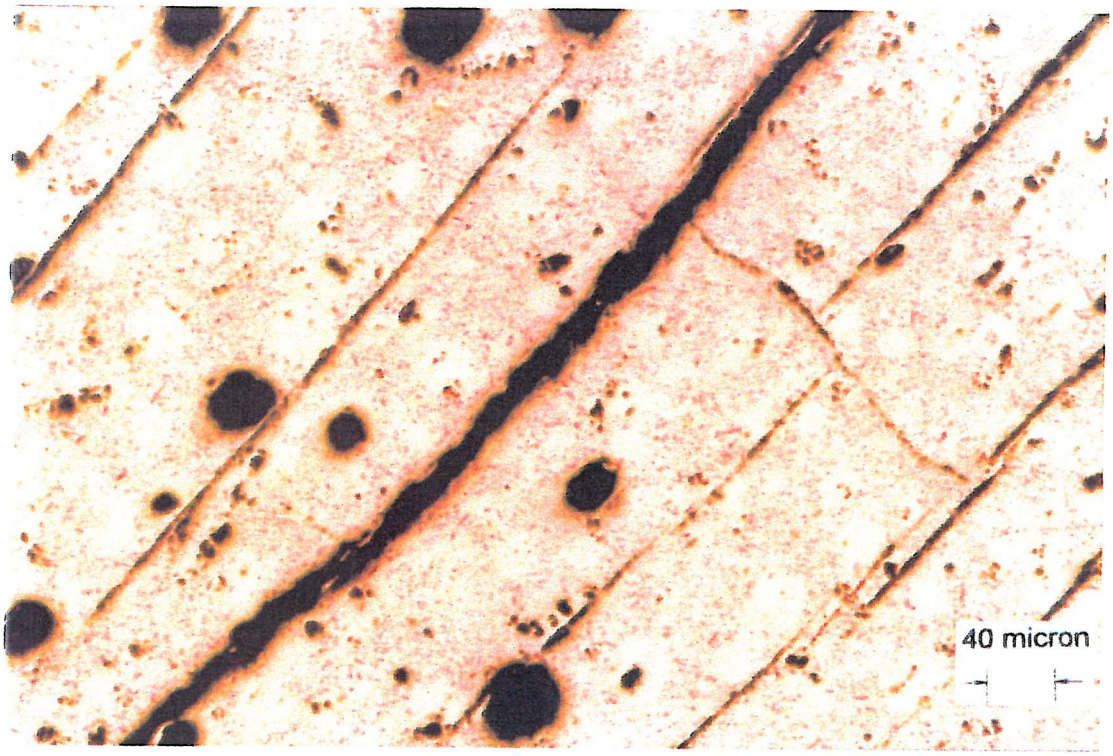

Fig 4.7 Long range Y211 phase distribution found in samples prepared using PMQ powders.

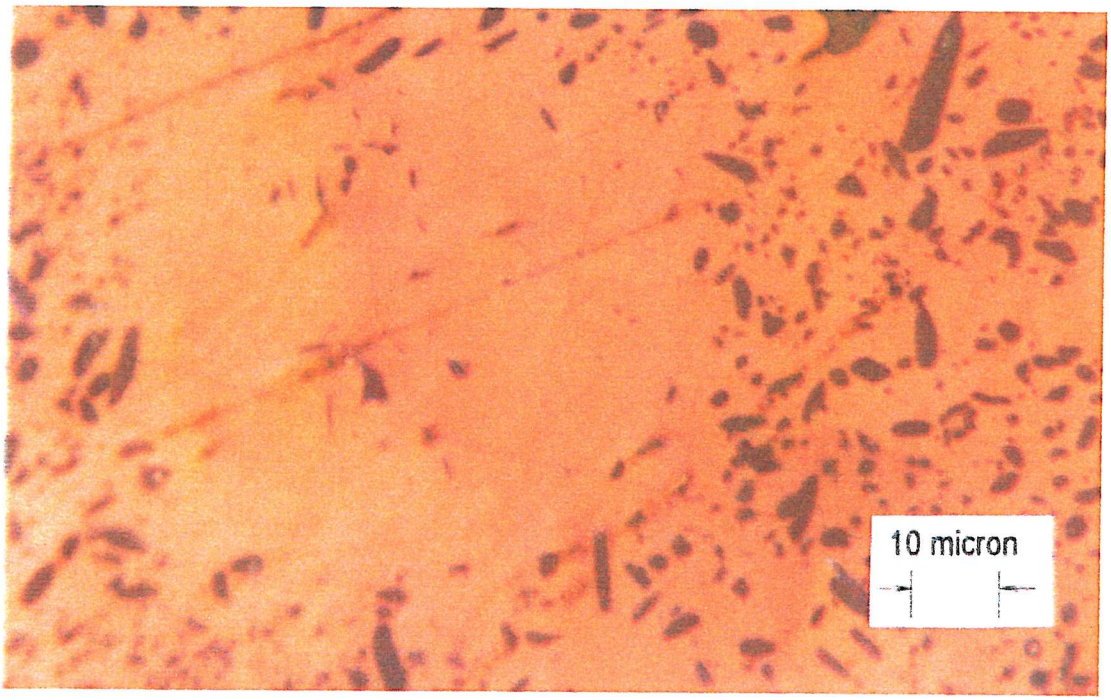

Fig 4.8 Area of depleted Y211 concentration.

The mechanism behind these regions of reduced Y211 density is believed to be closely connected to the growth kinetics of the Y123 bulk. It is known that the preferential direction of crystal formation is in the ab plane, as the velocity of solidification is larger in this direction. For this reason it is possible for propagation in the c direction to occur at many places. It is believed that these regions of reduced Y211 density correspond to regions of growth initiation in the c direction. The Y123 is effectively seeded in the c direction by the already formed bulk. Hence it is in these regions that the largest amount of Y_2O_3 is dissolved by the liquid phases and used for growth of Y123. This may also explain the elongated nature of the few Y211 inclusions found within these regions, as any ripening will take place primarily in the direction of the bulk crystal growth. This kind of evidence for the nature of crystal growth is less observable in samples prepared from normal powders because the inclusions are larger, and so are less prone to dissolution.

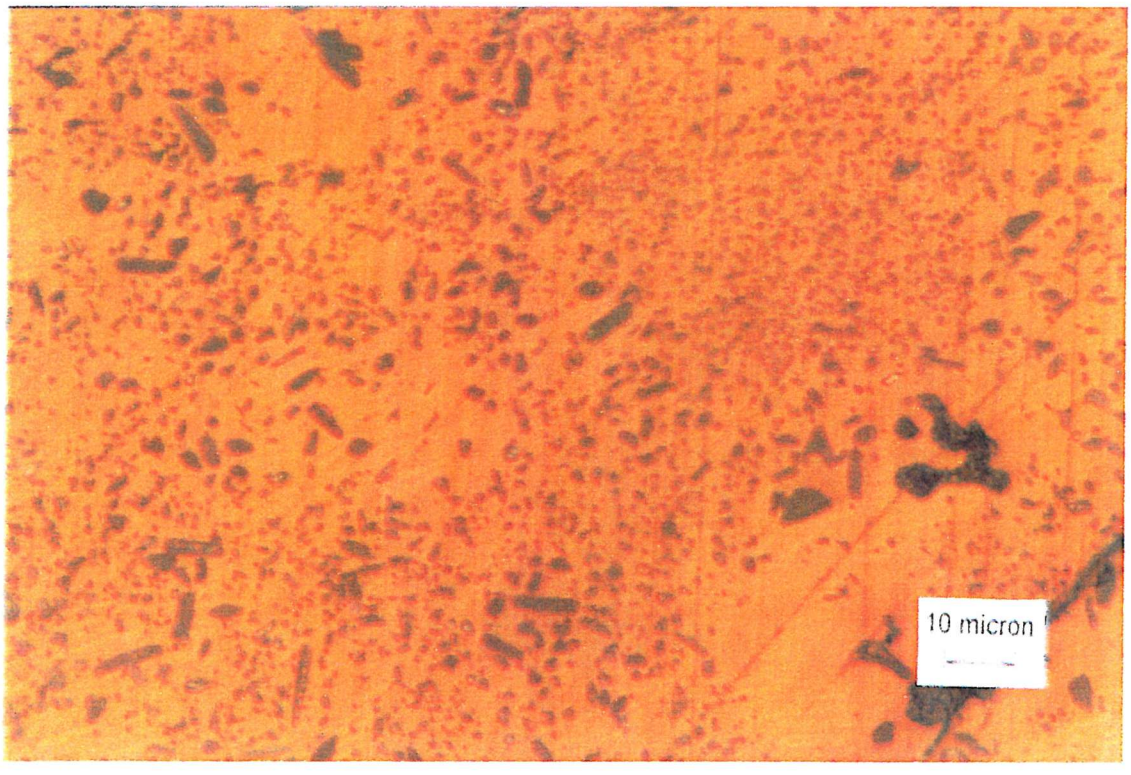

Fig 4.9 Micro structure of sample 3, processed with an increased initial ramp rate.

Shown in Fig 4.9 is the microstructure of a sample produced with a high initial ramp rate. From examining samples such as this it was deduced that variation of the initial ramp rate between 60°C/hr and 300°C/hr had little to no effect on the Y211 distribution within the bulk. Reginalda et al[13] has suggested that during heating crystals of Y123 form, and it is the interfaces of these crystals which can act as nucleation sites for Y211. Hence, if one increases the ramp rate, the equilibrium size of the crystals is reduced, therefore there is a higher density of nucleation points, resulting in a finer distribution of Y211. The effects of this process were not observed in this study. This reinforces the proposition of Varanasi et al[14] who states that this effect is dominated by other processes unless the ramp rate is in excess of 700°C/hr. This extremely high value imposes practical difficulties with respect to furnace design and also cause other issues related to the almost spontaneous evolution of gasses which are the consequence of having such a high rate of heating.

Seen in Fig 4.10 is an illustration of a sample processed with an increased dwell time above the peritectic. A long dwell time is in some cases desirable as the increased densification which results can compensate for a high ramp rate or a low maximum temperature. However, in this instance it is apparent that the increased duration available for Ostwald ripening of the Y211 phases and the increased liquid losses have resulted in a microstructure with a larger volume fraction of Y211 phase, the average diameter of which is greater than that seen previously.

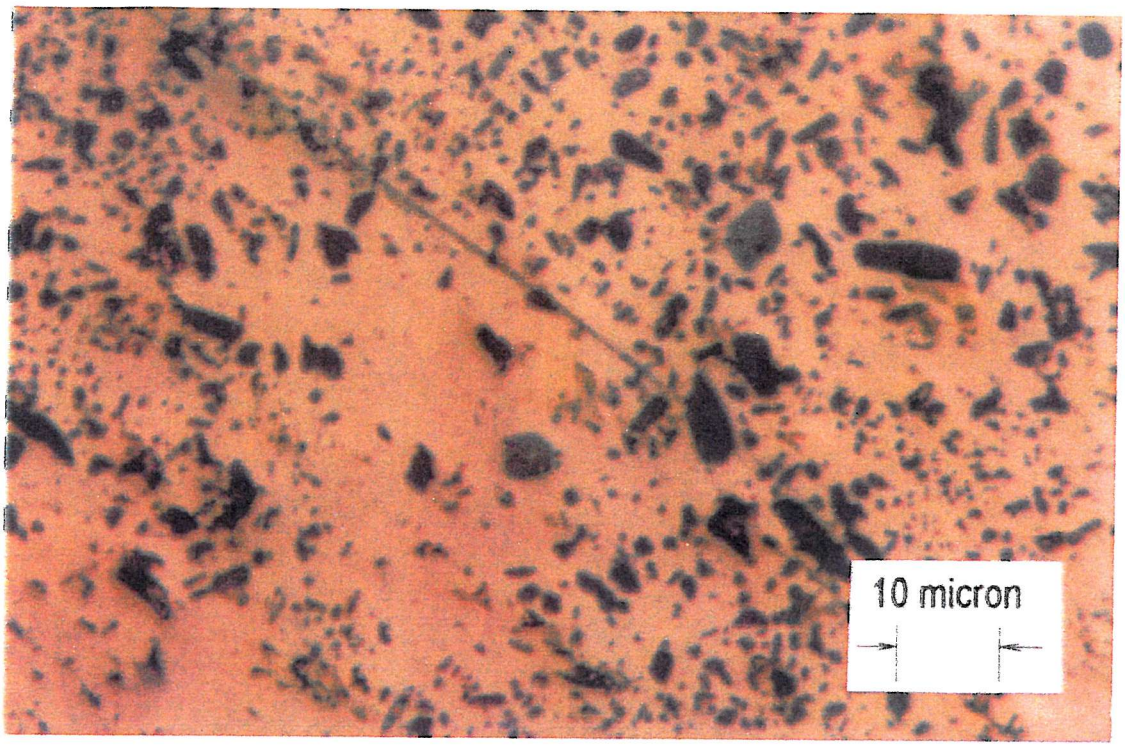

Fig 4.10 Sample 4 illustrating the increased size of Y211 inclusions which result from a high dwell temperature.

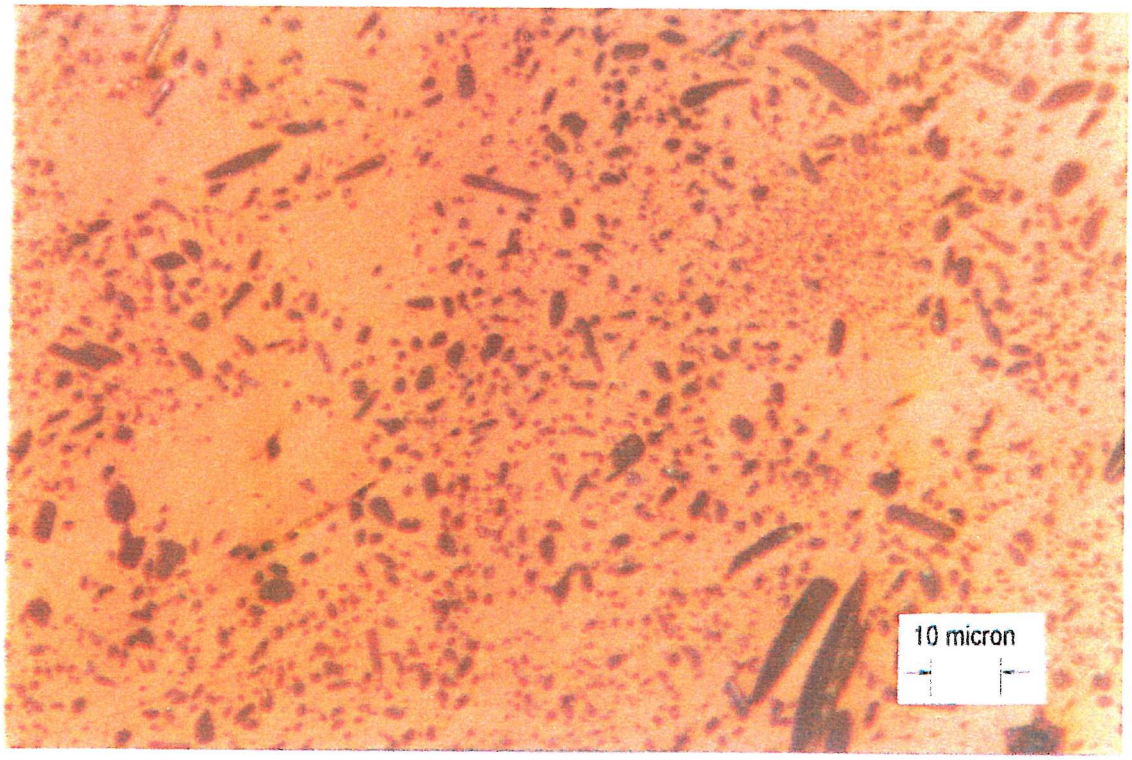

Fig 4.11 Sample 5 which was processed with a higher maximum temperature.

The effects of variation in the maximum temperature have also been investigated. Shown in Fig 4.11 is a micrograph of a sample processed with a peak temperature of 1125 °C. A high maximum such as this can be beneficial as the reduced viscosity of the liquid phases at high temperatures allows gas to escape and aids densification. However, increased liquid loss is a side effect of this process, often resulting an inhomogeneous material. In this instance, as no temperature gradient is employed, little inhomogeneity results. The material produced show little or no variation from that produced at a lower temperature. For the production of large single crystals it is necessary to use a temperature gradient, so, as no benefits to the microstructure result from a higher temperature, there is no reason to risk inhomogeneity by employing a high peak temperature.

Sample	**Ramp Rate** **°C/hr**	**Temperature** **°C**	**Dwell Time** **min**
No. 1	300	1040	30
	Step	1010	0
	1	960	0
	Step	0	End
No. 2	300	1040	30
	Step	1010	0
	1	960	0
	Step	0	End
No. 3	1000	1040	30
	Step	1010	0
	1	960	0
	Step	0	End
No. 4	300	1040	90
	Step	1010	0
	1	960	0
	Step	0	End
No. 5	300	1125	30
	Step	1010	0
	1	960	0
	Step	0	End

Fig 4.12 Table of the thermal cycles used to produce the samples under examination.

4.5 Conclusion

In this chapter a novel method for the preparation of high quality Y123 powder has been presented. It has been successfully shown that this method of powder production produces samples with a high quality microstructure, displaying many of the characteristics necessary for superconducting properties to persist at high levels of electromagnetic field. Also it has been possible to study the effects of processing conditions on the resultant microstructure and so gain some insight into the mechanisms involved.

It should be noted that the examples presented here are a small cross section of the sum of the samples produced. Subtle variations in the thermal cycles employed to create the pellets appeared to have little to no effect on the resultant microstructure. Hence, it is felt that there is little value in providing a discussion on every variation in processing conditions employed . This is in itself interesting as it has often been contended that the microstructure of large grain Y123 is strongly dependent on precise control of thermal processing.

4.6 References

1. K. Salama and D. F. Lee, *Supercond. Sci. Technol.,* vol. **7**, (1994)

2. P. Diko, W. Gawalek, T. Habisreuther, T Klupsch and P. Gornert, *J Microscopy*, Vol. **184** (1996)

3. P. Diko, *Mater. Sci. Eng*, vol. **B53**, (1998)

4. M. E. McHenry and R. A. Sutton, *Progress in Materials Science*, Vol **38**, pp. 159-310 (1994)

5. M. A. Cambell and J. E. Evetts, *Critical Currents in Superconductors.* Taylor and Francis, London (1972)

6. E. H. Brandt, *J. Low Temp. Phys.* **26**, 735, **28**, 290 (1977)

7. A. I. Larkin and Yu N. Ovchinkov, *J. Low Temp. Phys.* **34**, 409 (1979)

8. C. P. Bean and J. D. Livingston, *Phys. Rev. Lett.* **12**, 14 (1964)

9 M. Murikami, N. Sakai, Tiguchi and S I Yoo, *Supercond. Sci Technol*, **9** (1996)

10. C. Varansi, P. J. McGinn and S. Sengupta, *Journal of Electronic Materials,* Vol. **23**, 11 (1994)

11. M. Murikami, M. Murita, K. Doi and M. Miyamoto, *Jpn. J. Appl. Phys.* **28**, 1189 (1989)

12. S. Sengupta, D. Shi, J.S. Lou, A. Buzdin, V. Gorin, V. R. Todt, C Varansi and P.J. McGinn, *J. Appl. Phys.* **81** (11) (1997)

13. J. Reginalda, X. Yao, D. G. McCartney, C. J. Kiely and F. J. Tatlock, *Materials Lett.* **17** (1992)

14. C. Varansi and P. J. McGinn, *Journal of Electronic Materials,* Vol. **22**, 10 (1993)

Chapter 5 : The Effects of Neutron Irradiation on Undoped and Lithium Doped Single Grain Melt Textured Bulk YBCO

5.1 Introduction

In order to improve the superconducting properties of high temperature (HTc) superconductors it is imperative that vortex pinning is increased. It is understood that the pinning force is a function both of the thermodynamic properties and the microstructure of the material[1]. Pinning centres can be introduced via the introduction of defects into the crystal lattice, the size, distribution and topology of which all strongly effect the J_c of the given material[1]. Consensus suggests that uniformly dense, non-overlapping pinning centres of a size comparable to the coherence length would provide optimum conditions with respect to J_c.

One method of artificially introducing defects into a HTc superconductor is to use various forms of radiation. These include proton[2], electron[3], charged ion[4] and neutron irradiation[5]. With the exception of neutrons, all of these forms of irradiation involve charged particles which interact strongly with solid matter. This leads to the formation of a very inhomogeneous build up of defects, which is not desirable when attempting to improve superconducting properties. As neutrons are uncharged they penetrate freely into materials such as YBCO and so a homogeneous distribution of defects results. However, as neutrons interact so weakly, expensive prolonged exposure is necessary (5×10^{18} neutrons/cm^2), although critical currents have been improved by factors of 3-10 via this process. As a way of bypassing these problems YBCO powder has been doped with 1%mol LiHO and then melt grown. A reasonable proportion (7.6%) of the lithium is ^{6}Li. This isotope has a large neutron absorption cross section (σ = 945 Barns) and its fission products consist of an α particle and a ^{3}H ion[6]. These particles are emitted virtually back to back and so form columnar defects of up to 25μm in length. As the Li is evenly distributed throughout the material and the neutrons are not strongly absorbed by Y, Ba, Cu or O, the fission-fragment damage tracks will be homogeneously distributed within

the bulk. A similar approach has been adopted by Weinstein et al[7] with considerable success. They have demonstrated a substantial increase in critical current (a factor of around 4.5) by irradiating U doped YBCO with around 10^{17} neutrons.

5.2 Theoretical

As mentioned previously, a variety of irradiation techniques have been employed with the intent of improving the superconducting properties of superconductors via microstructure alteration. These attempts have shown a large degree of success with respect to increasing the intrinsic critical current of high temperature superconductors. The degree and nature of the damage incurred by the various processes are dependent upon the fluence, energy and scattering cross sections of the irradiating species as well as the conditions in which the irradiation process takes place (i.e. temperature, beam current, etc). Two distinctions may be made between they types of radiation. Firstly, between uncharged (neutrons) and charged (all other forms of irradiation), and secondly between those which create localised defect cascades, those that leave defect tracks and those in which fission fragments provide damage.

Using irradiation techniques we are able to vary the state of disorder within superconducting materials, which is related to the defect concentration within the material. The can vary in extent from dilute vacancy formation to enough disorder to force phase transitions or to the large number of atomic displacements necessary fro amorphization of the material. The link between radiation induced defect structures and superconducting properties has been convincingly illustrated for many conventional superconductors[8]. For high temperature superconductors it has been well established that disorder in the oxygen sub lattice is closely related to the superconducting properties of the material. Hence it was thought that irradiation induced oxygen displacements would cause T_c to be suppressed. It was only as a result of experimental studies that the importance of pinning was recognised.

Because neutrons are uncharged particles only nuclear scattering events are relevant in determining the damage caused to the structure of the material. For charged particles the main form of interaction is scattering from the electron cloud. The result of this distinction is that neutrons transfer much less energy per unit length. This means that fast neutrons may penetrate freely through YBCO samples of over 1cm, whilst 3.5 Mev protons have a range of around 60 microns. This impacts both the degree of microstructure alteration and the spatial extent of the effected regions. One of the most important factors for the enhancement of critical current densities in HTSC materials is the homogeneity of the defects, hence the large spatial extent of neutron damage offers distinct advantages. A further consideration is that neutron induced damage normally occurs in clusters which are reasonably large, i.e. around 25 Angstroms.

5.3 Sample Preparation

In order to produce single grain samples of undoped YBCO a standard seeded melt grown procedure was employed[9-13], as described in detail in Chapter 3. Undoped samples were produced from 0.5 inch pellets pressed from a stoichiometric powder mixture of 0.9Y123 + 0.1Y211. These pellets were then thermally processed in a vertical furnace with an identical configuration and thermal cycle as that given in chapter 3.

The lithium doped samples were prepared from a powder mixture of 0.9Y123 + 0.1Y211 + XLiHO mol, where X was varied from 0.01 to 0.02. This powder was then used to press 0.5 inch pellets suitable for melt processing. The initial results of melt processing lithium doped pellets in an identical manner to that employed for the production of undoped single grains demonstrated that a different thermal cycle would need to be devised for the manufacture of lithium doped YBCO single grains. Lithium doped pellets produced in this manner displayed a large degree of liquid phase loss (i.e. the loss of barium-copper oxides) resulting in a high degree of shrinkage. Also, only a small fraction of the pellet is able to form Y123 material due to the deficiency in the amount of liquid

phases which are necessary for the continuation of the growth process. An example of a pellet grown in this way can be seen in Fig 5.1.

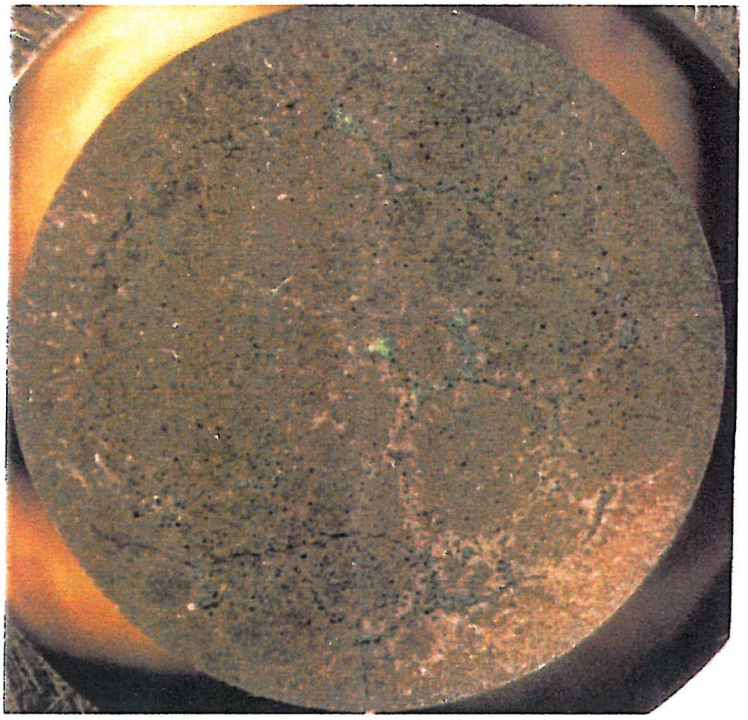

Fig 5.1 Photograph showing the morphology of a lithium doped YBCO pellet processed using a standard melt processing technique.

It is apparent from this evidence that the addition of lithium increases the amount of liquid loss during processing, hence it may be deduced that the dopant in some way reduces the viscosity of the melt, reduces the peritectic of the compound or induces a combination of both. For these reasons it was decided to continue only with the minimum doping level, which is given by X=0.01.

Liquid losses have always been a problem when melt processing bulk YBCO. However, this issue can be addressed in two simple ways; firstly by a reduction in processing temperature and secondly by doping with Y211 phase. As the processing parameters used have been shown to be successful with material undoped with lithium and as the powders have already been doped with Y211 phase it was concluded that reducing the processing

temperatures would be the best course of action. With this in mind, a systematic study was undertaken in which the thermal cycle used to produce undoped material was gradually adjusted downwards until a suitable regime for manufacturing lithium doped material could be found.

This approach proved successful, with the objective of producing single grains of lithium doped YBCO being achieved. It was found that the addition of 1% (mol) LiHO to the powder mixture reduced the effective peritectic temperature of the melt by around 14°C.

Fig 5.2 and Fig 5.3 show polarised optical micrographs of the microstructure of the lithium doped and undoped samples produced in the manner described previously. Both materials show a good, dense structure. However, in comparison with the standard, undoped material the lithium doped bulk shows a slightly unusual microstructure with respect to Y211 phases. The large inclusions are as expected and can be attributed to the large quantity of liquid phase lost during processing. However, also present in the Li doped sample are regions of uniformally small inclusions of 211 phase. The mean diameter of the inclusions in these regions is smaller than that observed in the undoped bulk, a desirable feature from the point of view of flux pinning. This strange formation could be attributed to several mechanisms. One could be that the lithium itself acts as a nucleation site for Y211 formation thus resulting in a finer, more even distribution. The lithium could inhibit the ripening process which causes Y211 inclusions to enlarge during thermal processing. Both of these attributes have been demonstrated by the addition of platinum to powders prior to processing. Another factor could be that, as the peritectic temperature has been reduced considerably, the degree of ripening has also reduced. The loss of liquid phases has also increased shifting the stoichiometry towards the Y211 rich region which could also result in an improved distribution.

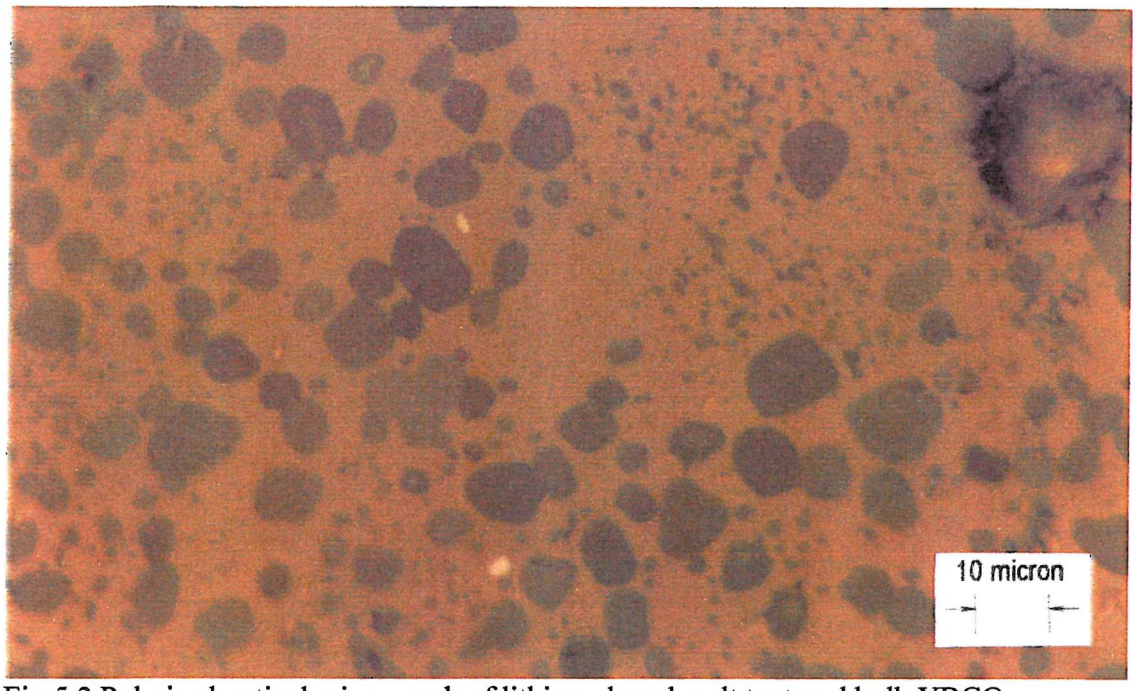

Fig 5.2 Polarised optical micrograph of lithium doped melt textured bulk YBCO

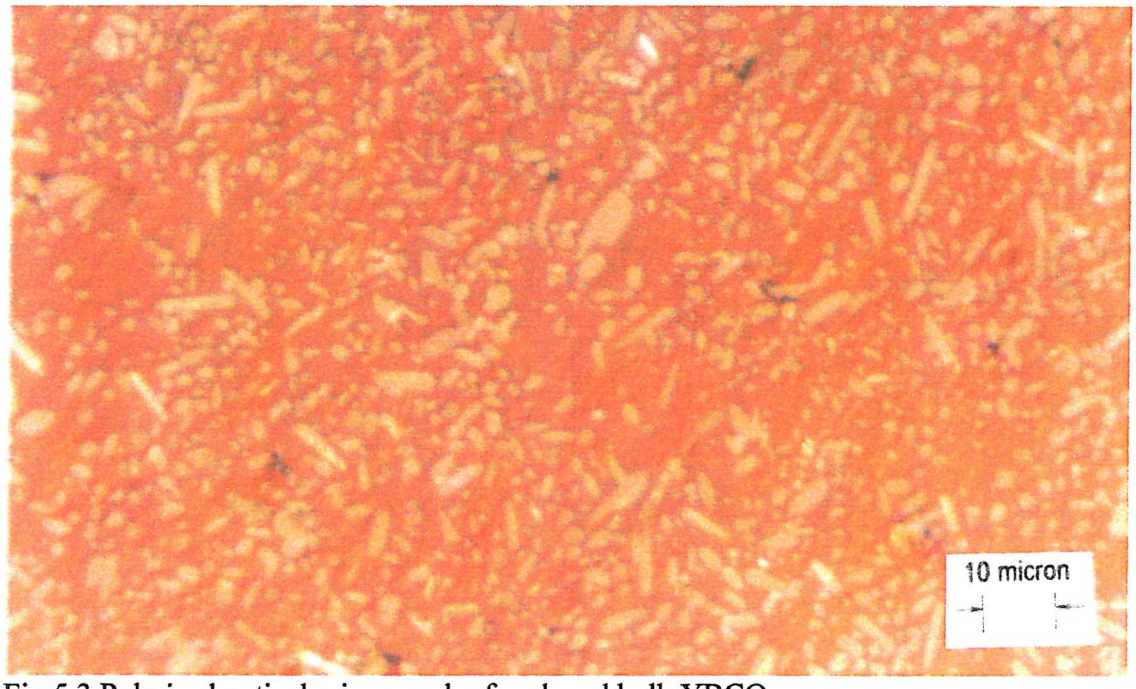

Fig 5.3 Polarised optical micrograph of undoped bulk YBCO.

After thermal processing single grain samples suitable for irradiation and measurement had to be sectioned from the lithium doped and undoped pellets. Firstly, the top surface of

the pellets is polished and examined using a polarising microscope. From this it is possible to ascertain the suitability of the material, i.e. grain size, grain orientation, the presence of large voids, etc. Then a suitable large single grain is cut using a wafering diamond saw. The samples used for irradiation and measurement were of dimensions 4×4×0.25mm (smallest dimension parallel to the c axis), but for comparative purposes it was necessary to prepare two samples from a single grain, one for irradiation and one to act as a control, hence the single grains used were at least twice this size in the ab direction. In addition to the samples described above, another sample of undoped YBCO was cut from the same grain as the square plate samples. This sample was 1×0.2×5mm in size, with its longest dimension perpendicular to the c axis. The purpose of this sample was to allow geometric considerations to be accounted for when examining magnetisation data, a procedure to be described in more detail later.

All samples were then annealed in the same furnace at 500 °C for 100hrs in flowing oxygen. One sample of lithium doped and one sample of undoped YBCO were then transported to the Imperial College reactor at Ascot where they underwent irradiation by approximately 10^{17} thermal neutrons cm^{-2} over a period of around 5 days.

5.4 Measurement and Results

All magnetic measurements presented here were made using a vibrating sample magnetometer(V.S.M). This device operates by vibrating a sample in a controlled manner in the presence of an applied magnetic field. Pick up coils are then used to so as an induced e.m.f. may be measured for a range of applied fields, allowing the magnetic moment of the sample to be quantified. Using the critical state model and the geometry of the sample, the critical current for any given applied field may be calculated, as is shown in eq 5.1:

$$Jc = \frac{10 \times \Delta M}{a - (a^2 / 3b)} \qquad \text{eq 5.1}$$

where a is the thickness and b is the width in an infinite slab geometry. As this conversion is only correct for the infinite slab geometry, and as the samples to be studied here are of a plate geometry, it was necessary to in some way provide a scaling function so that the geometric demagnetisation factor could be eliminated. This was achieved by preparing two samples from the same grain of the undoped, non-irradiated material. The first sample was of identical geometry to the rest of the samples prepared for this study i.e. 4×4×0.25mm, whilst the second sample was of dimensions 1×0.2×5mm, a much better approximation to the infinite slab geometry. After making measurements with both samples it was relatively simple to produce a scaling function which, as the material of the samples was as close to identical as possible, accounted only for the difference in geometry. As the dimensions of all the other samples were the same as the first sample, this function could then be used to account for their geometric dependencies, despite the fact the material itself could display different superconducting properties.

It should be noted that any direct comparisons made between doped and undoped samples should be seen in a qualitative manner only. The superconducting properties of YBCO vary from region to region, grain to grain and sample to sample, even if processing conditions are identical, which is not the case here.

Shown in Fig 5.4 to Fig 5.6 are the field dependences of the four different samples at 77 K, 65 K and 30 K respectively.

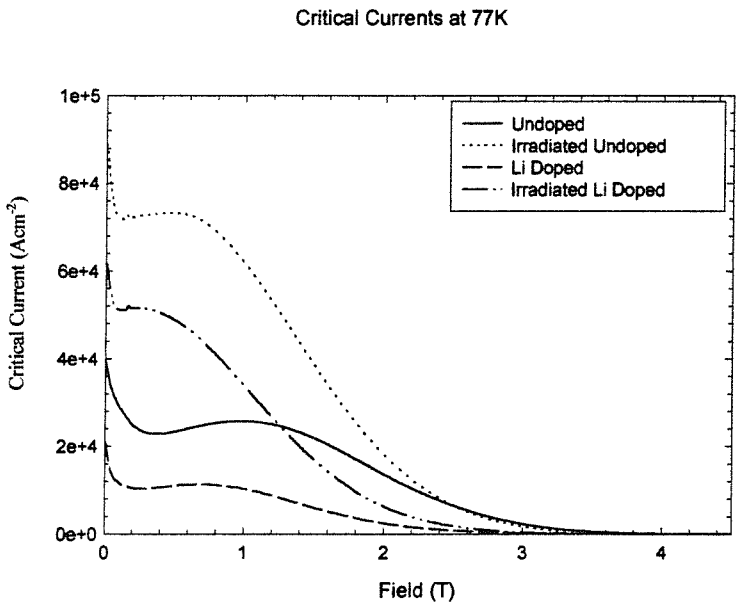

Fig 5.4 Critical current densities as a function of field for Li doped and undoped melt-grown YBCO single grains at 77 K.

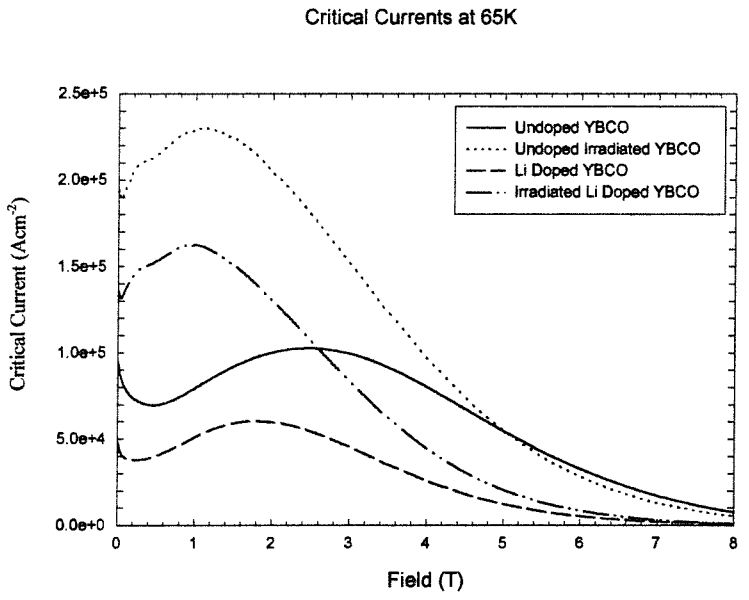

Fig 5.5 Critical current densities as a function of field for Li doped and undoped melt-grown YBCO single grains at 65 K.

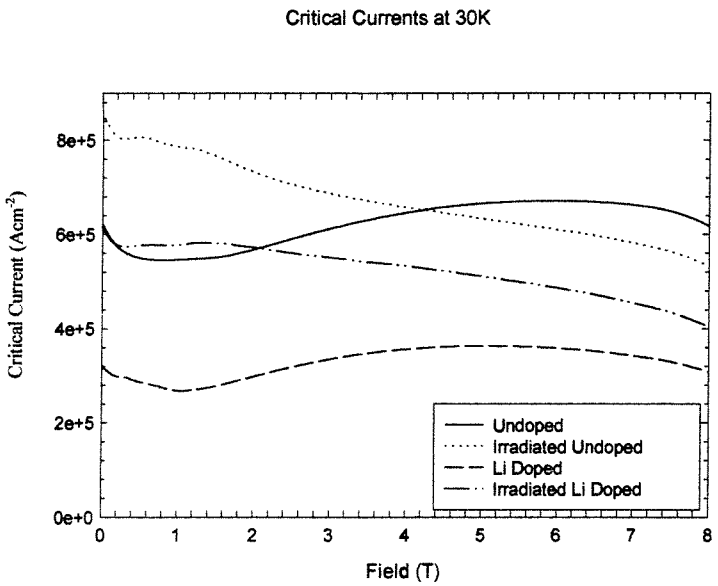

Fig 5.6 Critical current densities as a function of field for Li doped and undoped melt-grown YBCO single grains at 30 K.

It is immediately apparent from Fig. 5.4 to Fig. 5.6 that the irradiation process has changed considerably both the magnitude and field dependence of the critical currents, without actually increasing the irreversibility fields of the respective materials. The undoped and Li doped samples show very similar curve shapes both before and after irradiation at all temperatures. The magnitude of the J_c for the undoped sample is shown to be noticeably larger in both cases, but the actual size of the increase due to irradiation is very similar in both instances, as can be seen in Fig. 5.7 to Fig. 5.9. The shape of the curves is very similar when one compares doped with undoped. This would seem to indicate that the change in pinning centres observed is almost identical for both materials, hence the bulk of the increase in the lithium doped sample cannot be attributed to the dopant.

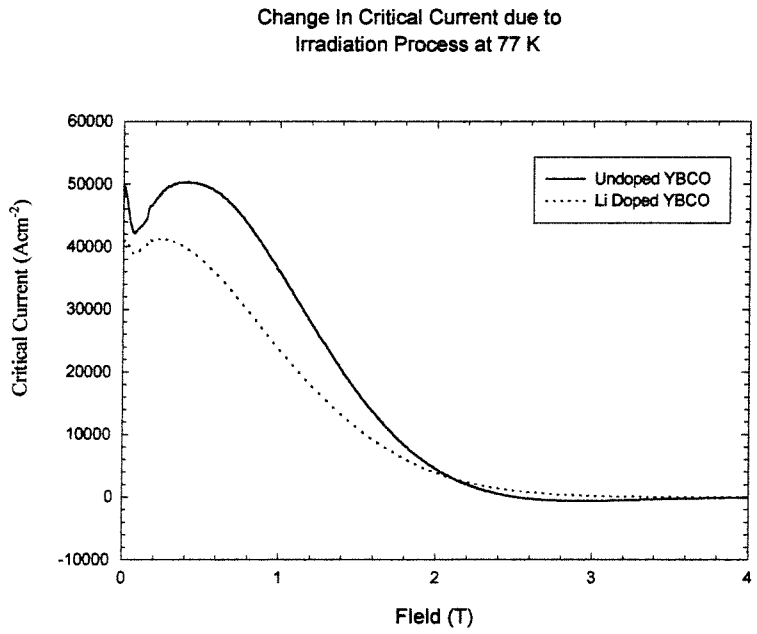

Fig. 5.7 Absolute increase in Jc due to irradiation process at 77K.

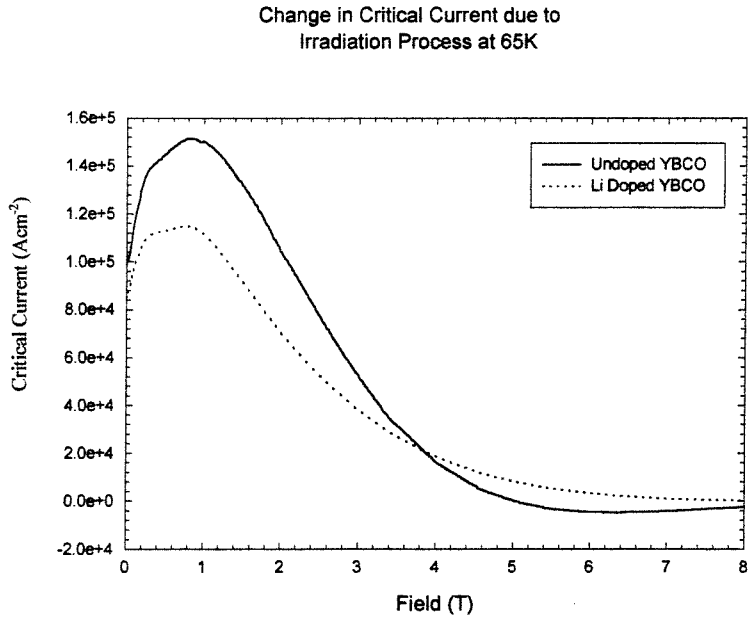

Fig 5.8 Absolute increase in Jc due to irradiation process at 65K.

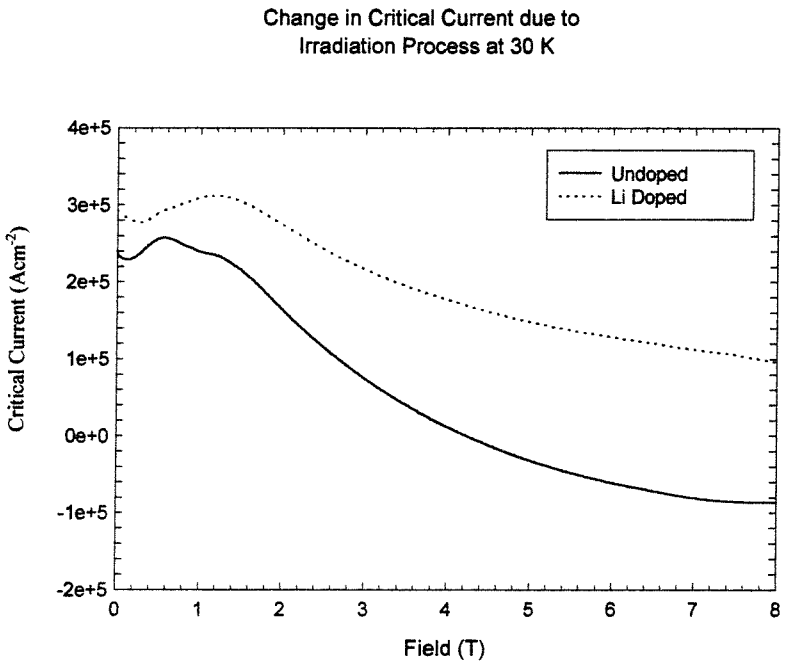

Fig. 5.9 Absolute increase in J_c due to irradiation process at 30K.

In terms of percentage increase when comparing normal and irradiated samples the change seen with the Li doped material is considerably larger (see Fig.5.10). It may also be seen that there is a slight depression of the irreversibility field for the undoped material after irradiation. This becomes more obvious from the data gathered at lower temperatures. The measurements taken at 30K clearly demonstrate that whilst the irradiation of the Li doped sample continues to contribute positively to the J_c of the material up to fields in excess of 8 Tesla, the undoped material has its Jc reduced by irradiation at fields larger than around 4 Tesla. In fact, at this temperature the contribution to J_c due to the irradiation of the Li sample is larger at all fields than that obtained from the irradiation of the undoped sample. The only indication that a distinct type of pinning centre may result from the presence of lithium within the bulk can be best observed in Fig. 5.10. At both 77K and 65K at 2 T and 6 T respectively a hump may be observed in the relative increase in J_c of the doped sample in contrast to the smooth curves seen with undoped material.

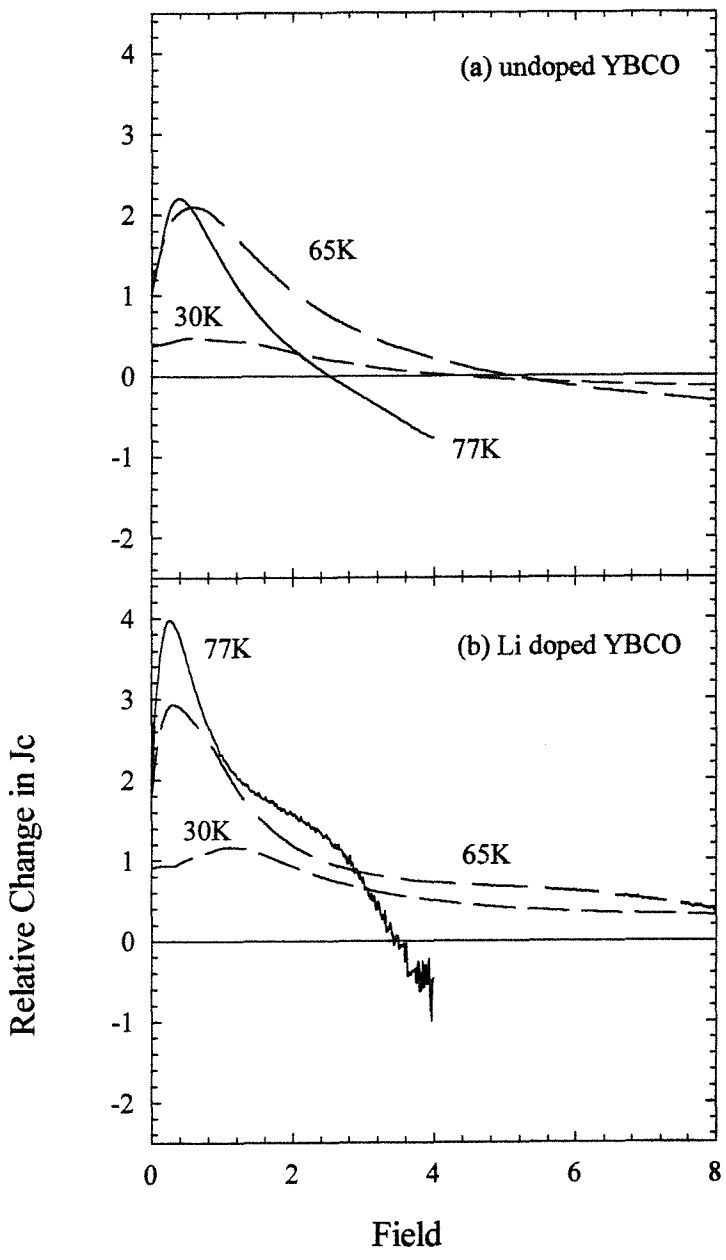

Fig. 5.10 Relative change in the critical current density at different temperatures before and after thermal neutron irradiation. (a) undoped YBCO and (b) Li doped YBCO.

If this is the case then it would suggest the presence of a low density of high field pinning centres.

5.5 Conclusions

Lithium doped melt grown YBCO has been processed and irradiated with thermal neutrons in an effort to improve flux pinning and hence J_c. The comparisons drawn here demonstrate the enhancement achievable with low fluence neutron irradiation. The strong similarity between the field dependencies of the doped and undoped samples after irradiation suggests that the fragmentation of the Li did not contribute significantly to the improved pinning observed. The large increase in J_c observed after the irradiation of the control was somewhat unexpected at such low fluencies. The data indicates that the irradiation process has effected the superconducting properties of the material in one of two ways. Either the effect of the original pinning mechanism has been reduced and superseded by another kind of pinning centre, or the intrinsic J_c of the material has been reduced due to the damage caused by the irradiation process, which, at low fields has been compensated for by the introduction of additional low field pinning centres. This is evident from the way in which at high field and low temperature the irradiated control sample is inferior to the normal control sample. The irradiated Li doped sample is always superior to the normal Li doped sample, but this can be attributed to the general poor quality of the Li doped material rather than to any effects due to Li fragmentation.

Continuation of this project will involve the optimisation of the initial processing, i.e. the production of Li doped YBCO with the same properties as the undoped material. This will be achieved via improved heating cycle and stoichiometry, and also finding the optimum Li fraction and neutron dosage with respect to inducing the largest possible increase in J_c. Microstructural observations and measurements of the quantity of Li remaining in the bulk are also planned, whilst repetition of the experiment using different dopants, such as boron, gadolinium[14] and uranium[7] are also anticipated.

5.6 References

1. M. E. McHenry and R. A. Sutton, *Progress in Materials Science* **38**, 159 (1994)

2. T.J. Shaw, J. Clarke, R. B. van Dover, A. E. White, L. F. Schneemeyer, R. J. Felder, and J. V. Waszczak, *Physical Review B* **54**, 21 (1996)

3. Y. Matsui, E. Takayama, and K. Kato, *Jpn. J. appl. Phys.* **26**, L1183 (1987)

4. K. V. Rao, R. Puzniac, D. X. Chen, N. Karpe, M. Baran, A. Wisniewski, K. Pytel, H. Szymczak, K. Drybye and J. Bottiger, *Physica C* **153-155**, 347 (1988)

5. R. L. Fleischer, H. R. Hart, K. W. Lay and F. E. Luborsky, *Phys. Rev.* **B 40**, 2163 (1989)

6. V. Sandu, G. Aldica, J. Jalklovszky, S. Popa, E. Cimpoiasu, C. Garlea and I Garlea, *Journal of Superconductivity* **8**, 3 (1995)

7. R. Wienstien, R. Sawh, Y. Ren, J. Lui and D. Parks, Preprint

8. C. S. Pande, *Phys. St. Solids,* **A 52**, 687 (1979)

9. W. Lo, D. A. Cardwell, C. D. Dewhurst and S. -L. Dung, *J. Mater. Res.* Vol. **11**, 786 (1996)

10. S. Marinel, J. Wang, I. Monot, M. P. Delamare, J. Provost and G. Desgardin, *Supercond. Sci. Technol.* Vol. **10**, 147 (1997)

11. W. Lo, D. A. Cardwell, S. –L. Dung and R. G. Barter, *J. Matter. Sci.* Vol. **30**, 3995 (1995)

12. D. Shi, D. Qu, S. Sagar and K. Lahiri, *Appl. Phys. Lett.* Vol. **70**, 3606 (1997)

13. M. Morita, S. Takebayashi, M. Tanaka, K. Kimura, K. Miyamoto and K. Sawano, *Adv. Supercond. Sci. Technol.* Vol. **3**, 733 (1991)

14 J. O. Willis, K. E. Sikafus and D. E. Peterson, *Advances in Superconductivity IV, Proc. 4th Int. Symp. Superconductivity,* Tokyo, 323, (1991)

Chapter 6: Post Processing Of Melt Textured Sm123

6.1 Introduction

Many of the potential applications of bulk high Tc superconductors demand high current capacity in the presence of high magnetic fields[1-3]. This has been a fundamental problem for all high Tc superconductors with respect to finding viable industrial uses. Although the production of single crystal RE123 materials has greatly improved the ability to conduct in large fields in comparison to sintered or multi-granular materials, the field dependence of the critical current is still too large. Attempts to reduce the field dependence and increase Jc at high fields via microstructure alterations resulting from the melt textured growth process have met with considerable success[4-8]. Refinement of the RE211[9] phase distribution, introduction of secondary phases[10-13] and various forms of irradiation[15] have all demonstrated their usefulness for increasing the high field pinning forces within the material. However, the most impressive advancement in this field has come from the processing of RE123 materials with large atomic radii (i.e. Sm123 and Nd123) in a reduced oxygen atmosphere[16]. With this technique irreversibility fields in excess of 10T and critical currents of ~40000Acm^{-2} at 2T and 77K have been achieved[15].

La	Nd	Sm	Eu	Gd	Dy	Y	Ho	Er	Tm	Yb	Lu
1.17	1.12	1.09	1.08	1.07	1.05	1.04	1.04	1.03	1.02	1.01	1.00

Fig 6.1 Atomic Radii of rare earth elements in Angstroms.

Shown in Fig 6.1 are the atomic radii of the various RE ions used in the production of RE123 materials. The atomic radius of Ba is ~1.49 Angstroms. It is apparent from this that the radii of Sm and Nd are closer to that of Ba than that of Y. It has been reported by many authors[16] that when the RE radius is comparable to Ba as is the case with Nd and Sm, then substitution takes place on the Ba site during melt processing in air:

$$RE + 2Ba + 3Cu + O_y \Rightarrow RE_{1+X}Ba_{2-X}Cu_3O_y \qquad \text{eq 6.1}$$

This substitution on the barium site is not observed in Y123 or Er123. Sm/Nd123 materials processed in air display low T_c, low J_c, good field dependence but poor irreversibility field when compared with Y123 at 77K. Many sources have reported using X-ray crystallography and EDX data that the suppression of the critical temperature is due to this substitution. It is proposed that a different, lower T_c phase is formed which suppresses the overall Tc and results in the generally inferior superconducting properties.

At first this phenomenon appeared to consign the light RE superconductors to being inferior cousins to materials such as Y123 and Er123. However, further investigation led authors such as Murikami to discover that melt processing of Nd123 in a reduced oxygen atmosphere produces a superconductor with a high T_c (~94K), a high J_c and a good field dependence (50000 Acm^{-2} at 77K and 2T). It was found that by carrying out the seeded melt growth process in 0.1% O_2, 99.9% Ar atmosphere high quality single grains could be produced that displayed a high field pinning mechanism previously not observed in the heavier ion RE123 materials. The reason for this improvement has not been fully understood until recently, when thermometric analysis was used to study the relationship between the substitution factor, denoted as X in equation 1, and the melting/solidification temperature of the composite. It has been demonstrated that there is a slight variation in melting/solidification temperature with X. The variation becomes greatly exaggerated in a low oxygen atmosphere, where as in air this correlation is too non-linear to exploit. It was found that the smaller the value of X, the higher the peritectic temperature of the melt, so with controlled solidification in a reduced O_2 atmosphere it is possible to produce a material with a small X value. Grigorashev et. al.[17] have produced a phase diagram of this system which has been reproduced in Fig.6.2.

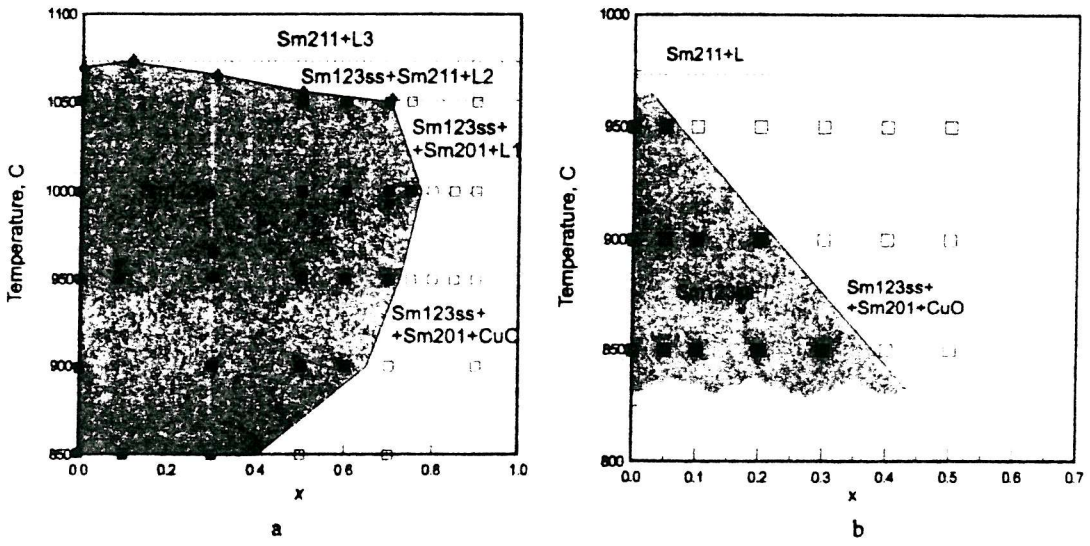

Fig 6.2 Phase diagram of $Sm_{1+X}Ba_{2-X}Cu_3O_Y$ in air (a) and 0.1% O_2 atmosphere (b)[17]. The shaded region corresponds to the temperature-composition combination where the material remains stable and solidified.

Using this phase diagram it can be easily understood how processing in a controlled atmosphere allows the value of X to be reduced.

This substitution is also the suggested source of the high field pinning mechanism seen in these materials. As stated previously, Nd and Sm ions are able to substitute on the Ba site, producing a lower T_c phase. If this process takes place in a limited manner, i.e. small X, then very fine Nd/Sm rich clusters are formed (around 200 nm). These regions are superconducting at low fields but at higher fields they become normal allowing them to act as very effective high field pinning centres. This is one of the reasons for the "fish tail" effect observed in the magnetisation curves of these materials.

As discussed, the processing of melt textured Nd and Sm in a reduced O_2 atmosphere produces high quality superconductors. However, there are difficulties with this process. Murikami et al[15] have shown that the best results come from working with very low oxygen partial pressures, 0.1% O_2 in Ar. Controlling the atmosphere to this degree of accuracy is difficult under beneficial conditions, but when attempted in conjunction with seeded growth the practical problems become inhibiting. The necessity of hermetically sealing a furnace whilst incorporating a flowing gas supply, providing temperature

gradients and a "cold finger" device for cooling the seeding region puts such demands on furnace design that cost and complexity of operation become serious considerations. Dimesso et al [18] have tried to overcome this problem by processing in air whilst shifting the stoichiometric ratio of the starting material towards the Ba rich region. This technique has enabled them to reduce the degree of Nd - Ba substitution whilst "batch processing" large numbers of samples at once. However, the reduction in X is not as large as that seen in the reduced oxygen regime, and so the resulting material is not of such a high quality.

In this chapter a novel method for producing melt textured Sm123 with a small value of X is presented and discussed. With this method, material that has already been melt processed in air is then post processed in a reduced oxygen atmosphere in an attempt to reduce the ratio of Sm - Ba substitution in already grown crystals. Systematic compositional and magnetic measurements are presented in an attempt to find the optimum temperature for phase conversion.

6.2 Procedure for the Preparation of Melt Textured Sm123

The technique used for melt textured growth of RE123 materials shows little variation from one rare earth element to another. The main factor which changes between the different materials is the peritectic temperature (Tp) at which growth begins. Y123 has a Tp of around 1010 °C where as for Sm123 it is around 1055°C. Although this difference may seem arbitrary, it does introduce some problems when melt growing. When Tp is reached, the material will decompose into RE211 (or RE422) and liquid phases. These liquid phases are similar in composition for both processes and are in the form of mainly barium cuprates. One can deduce from this that when processing Sm123 the liquid phases will be less viscous and so will be more easily lost during processing. Another factor resulting from the higher temperatures at which growth takes place is that a silver cold finger is less suitable as some melting takes place in the region of the plug. Also, at these higher temperatures the furnace, especially one with a temperature gradient, is put under much greater strain. For these reasons it was decided that rather than grow large monoliths using the method described in chapter 3, multi-granular samples melt grown in a standard horizontal tube furnace would be prepared.

Green powder was produced by repeatedly calcining and grinding a mixture of Sm_2O_3, $BaCuO_2$ and $Cu0_2$ powders. The calcined powder was then pressed into 0.5 inch pellets using a cold uni-axial press. As can be seen in Fig 6.3, a flat area was then ground on to the side of the pellet so that it could then be rested on its side on top of an yttria stabilised zirconia substrate. The configuration was used so as to ensure fairly uniform properties along the length of the pellet, i.e. reduce the variation due to liquid loss. Pellets were then processed using a standard melt growth thermal cycle, shown in Fig. 6.4, which was developed after various trials to produce fairly large grains with good overall density.

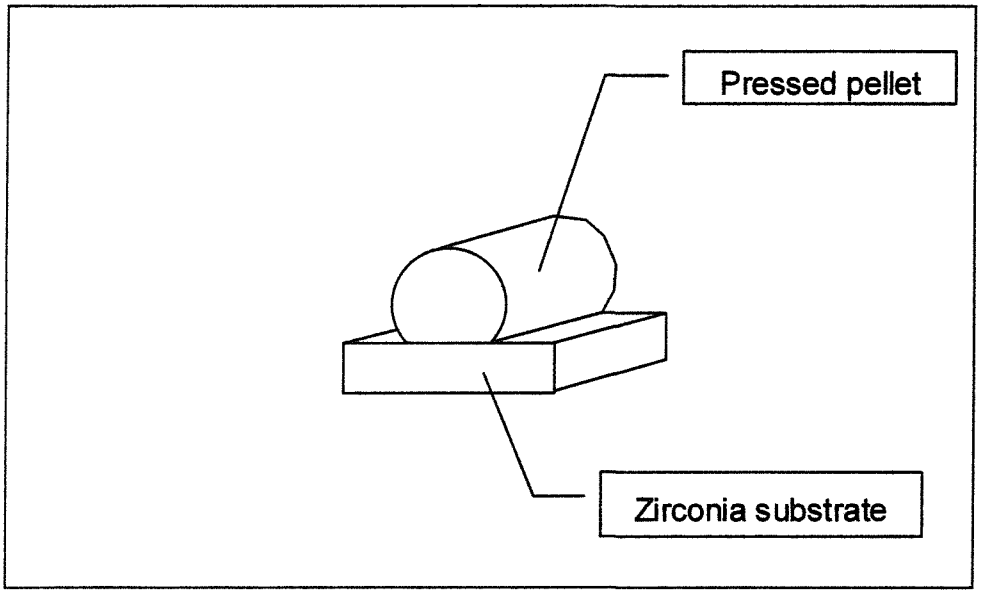

Fig 6.3 Schematic of Pellet configuration.

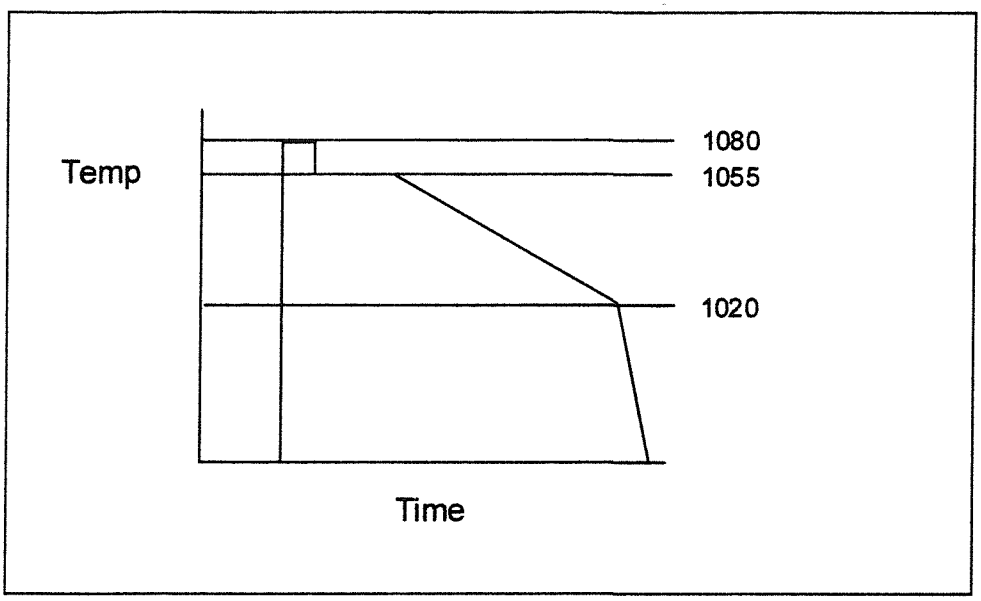

Fig 6.4 Thermal cycle for the processing of MTG Sm123. All temperatures quoted in °C

6.3 Sample Post Processing : Part 1

Initially, it was by no means certain that it was possible to convert phases from high to low X value without destroying the already formed crystal structure. With this in mind, a preliminary study was undertaken in which single grains were processed at high temperature in a reduced oxygen atmosphere and then examined using magnetic measurements to look for any shift in the field dependence and critical field which could be associated with a shift in the value of X.

The single grains were prepared as follows. Firstly, a pellet was selected and smashed between two copper plates. The fragmentation of the pellet often takes place along the cleavage plains, allowing the easy separation of single grain samples which can then be polished flat producing orientated samples suitable for VSM measurements. Although these samples are not uniform in shape or volume they are of similar geometry and identical alignment, so comparisons may be justifiably drawn.

First, it was necessary to ascertain the temperature at which these Sm123 crystals melt in an atmosphere of 0.1% O_2 / 99.9% Ar. A systematic study was undertaken in which single grains were heated up to various temperatures and then optically examined. The

criteria for the optical study was to find the point where the original structure was no longer present. Using this technique it was possible to measure the melting point to being between 933 and 938 °C. Although this figure is a useful reference temperature it should be noted that this melting temperature corresponds only to a particular ratio of Nd - Ba substitution, which is why a more accurate measurement is of little value as the ratio will vary from grain to grain and within the domain itself. Also, this value will only be correct for material prepared in a similar fashion to the crystals used here. This temperature indicates the point at which enough melting occurs to destroy the crystal structure, not the point at which melting is initiated at any point in the grain.

Once this limiting temperature had been found it made it possible to investigate the feasibility of conversion without the destruction of the grain. For this preliminary study, two single grain samples were processed at (a) 900 and (b) 920 °C for 100 hours in an atmosphere of 0.1% O_2 / 99.9% Ar. Magnetisation loops for these samples and an unprocessed sample (c) were measured using a vibrating sample magnetometer (V.S.M). All samples were oxygenated after processing in the same furnace at 320 °C for 100 hrs in flowing oxygen.

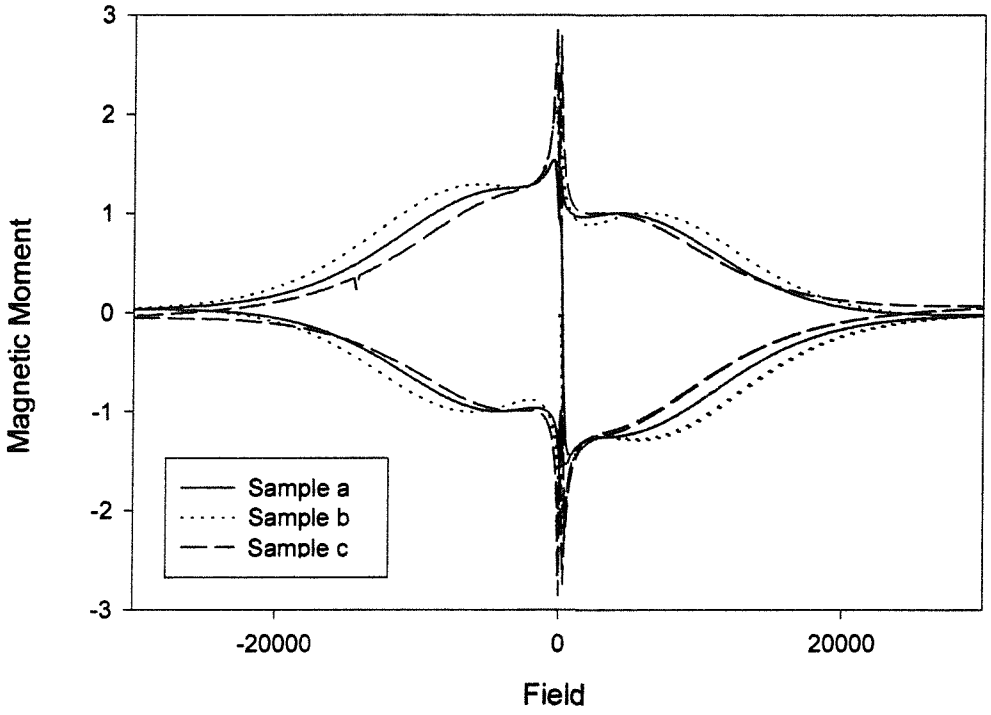

Fig 6.5 Normalised magnetisation curves of samples a and b processed at 900 and 920 °C respectively in 0.1% O_2 / 99.9% Ar for 100 hrs and sample c which is a control.

As can be seen in Fig 6.5, there is a small but definite shift in the in the magnetisation curves. Most apparent is the increased fishtailing of the curves with increasing temperature of processing. In addition, the irreversibility fields of these samples also increase with processing temperature. The shift to higher field observed in the fishtail could under different circumstances be attributed to different annealing conditions, but, as the samples were processed simultaneously under identical conditions, this explanation can be eliminated. This data can be interpreted as an increase in high field superconductivity correlating with a decrease in the proportion of low Tc phase present in the grains. Hence it follows that processing in the reduced oxygen atmosphere after crystal growth was successful in reducing the fraction of material with a very high substitution ratio in comparison to material with a lower ratio. The second part of this chapter studies this phenomenon in more detail.

6.4 Sample Processing : Part 2

For the second part of the experiment a multi-granular melt textured pellet was selected and cut into 1 mm thick quadrants using a wafering diamond saw. These quadrants were then sliced into wafers suitable for the experiment. All samples used for comparative purposes were cut from the same quadrant so as to ensure the similarity of their initial properties.

After demonstrating the feasibility of the post processing of melt grown Sm123 in a reduced oxygen atmosphere with a view to reducing the amount of Sm - Ba substitution, the next step was to refine the process and quantify the degree of substitution. It was decided that the best method for achieving this would be to take samples slowly up to a range of temperatures around the melting temperature (938 °C) found earlier, and then use back scatter data gathered using a S.E.M. to study the stoichiometry of the final samples. It was hoped that slowly ramping the temperature would provide enough time so as only a small fraction of the material would be at a temperature higher than its peritectic. Ideally the increase in temperature should be slow enough so as to allow one of two processes to occur; either to allow any small inclusion of material which has a high enough ratio of Sm-Ba substitution to melt, undergo some kind of phase migration and then re-crystallise with the same orientation as the surrounding bulk, or to facilitate a solid state diffusion process which changes the composition to match the equilibrium composition for the given temperature and atmosphere.

Six Sm123 quadrants were prepared as described above. Five of these samples were processed in a reduced oxygen atmosphere whist one sample was kept as a control. The five samples were processed in 0.1% O_2 / 99.9% Ar with the following thermal cycles; firstly all samples were heated at 60 °C/hr to a temperature of 920 °C. Then the temperature was increased at 1 °C/hr up to the maximum temperature (T_m) and held there for 12hrs. T_m was different for each sample, ranging from 940 to 1020 in steps of 20 °C. Following this, all samples were cooled at 100 °C/hr to room temperature.

The substrates used during these processes were standard alumina plates. Alumina poisons superconductors preventing any magnetic measurements being made with these samples. However, it was felt necessary to use alumina instead of yttria stabilized zirconia or platinum because it was found that the use of these materials resulted in the samples sticking to the substrate, prohibiting their removal for examination without the samples breaking. Also, platinum is readily dissolved by any liquid phases, a factor which could effect the microstructure and peritectic of the bulk. The slightly porous alumina substrate was found to absorb any small amounts of liquid phase released during processing away from the sample without any large degree of sticking and without a detectable amount of chemical transfer back to the sample. All the samples presented were processed this way successfully with the exception of the samples with T_m at 980 °C and 1020 °C. The failure of the sample processed at 980 °C was due to external factors related to the presence of impurities in the furnace. The sample processed at 1020 °C produced more liquid phases than the other samples and so broke whilst being removed from the substrate. Fortunately it broke into pieces large enough to be useful. The reasons behind the excess liquid phases released by this sample will be discussed in more detail later.

Following thermal processing in a reduced oxygen atmosphere all sampled were annealed together in flowing O_2 for 100 hrs at 320 °C. This annealing process was carried out so as to improve the contrast available when using the optical polarising microscope to examine the structure of the samples.

6.5 Results and Discussion

Shown in Fig 6.6 to Fig 6.10 are polarised optical micrographs of each of the samples (with the exception of the sample with T_m=980) after processing a reduced oxygen atmosphere.

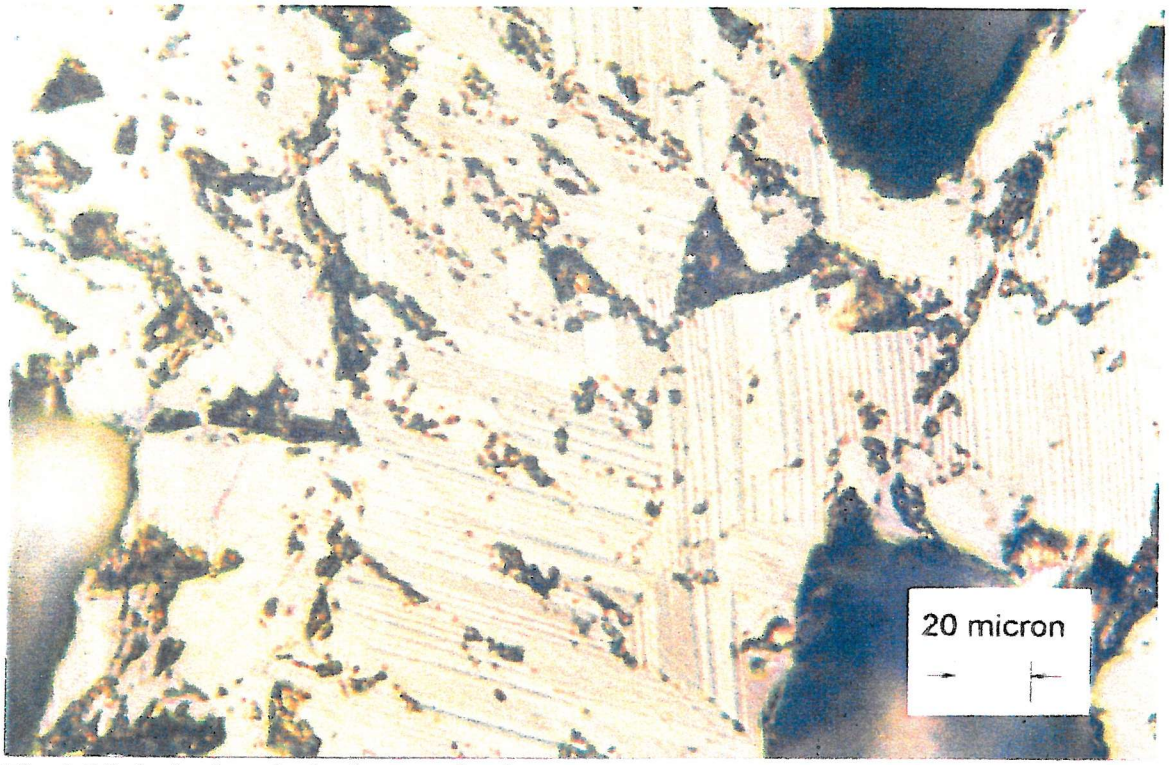

Fig 6.6 Polarised optical micrograph of control sample grown in air

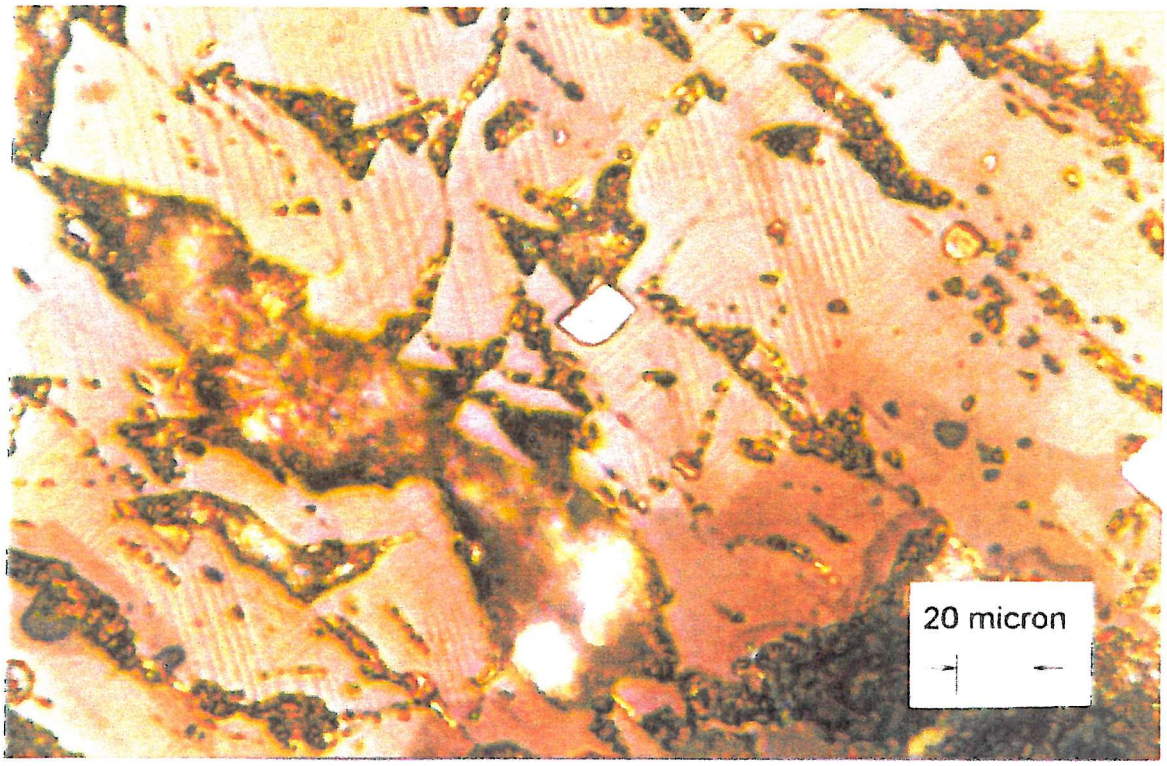

Fig 6.7 Polarised optical micrograph of sample post processed at T_m=940 °C

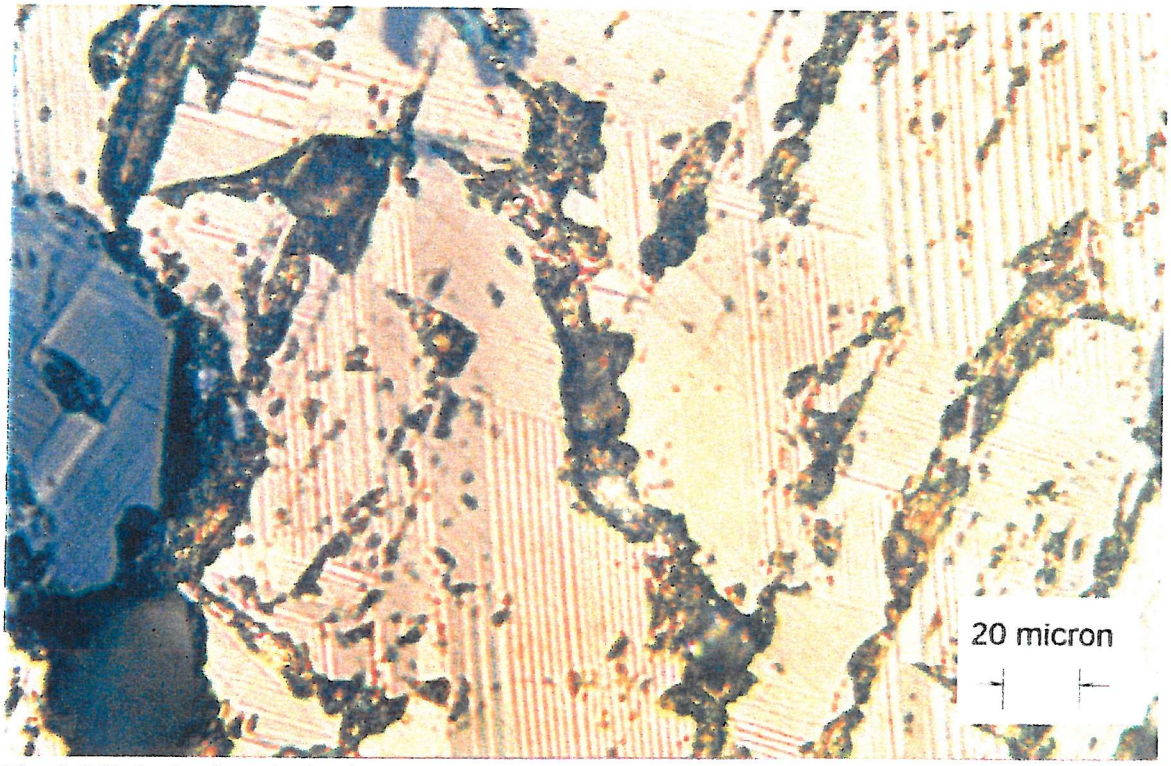

Fig 6.8 Polarised optical micrograph of sample post processed at T_m=960 °C

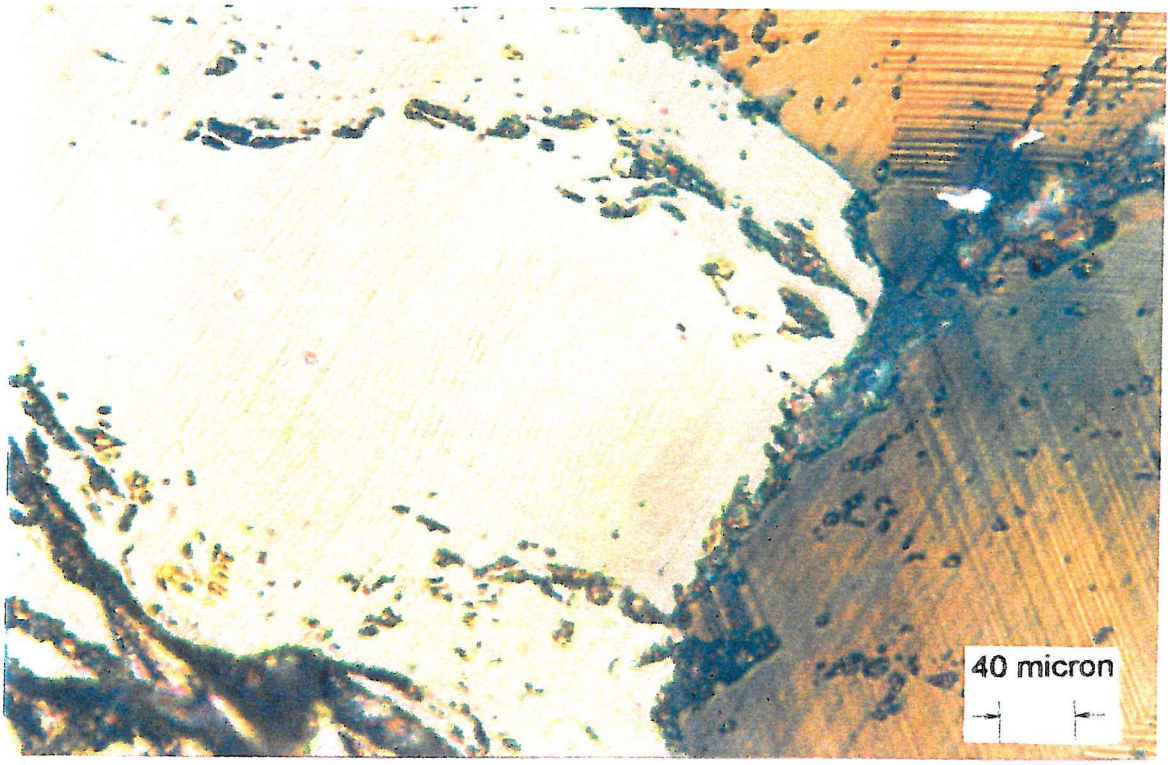

Fig 6.9 Polarised optical micrograph of sample post processed at T_m=1000 °C

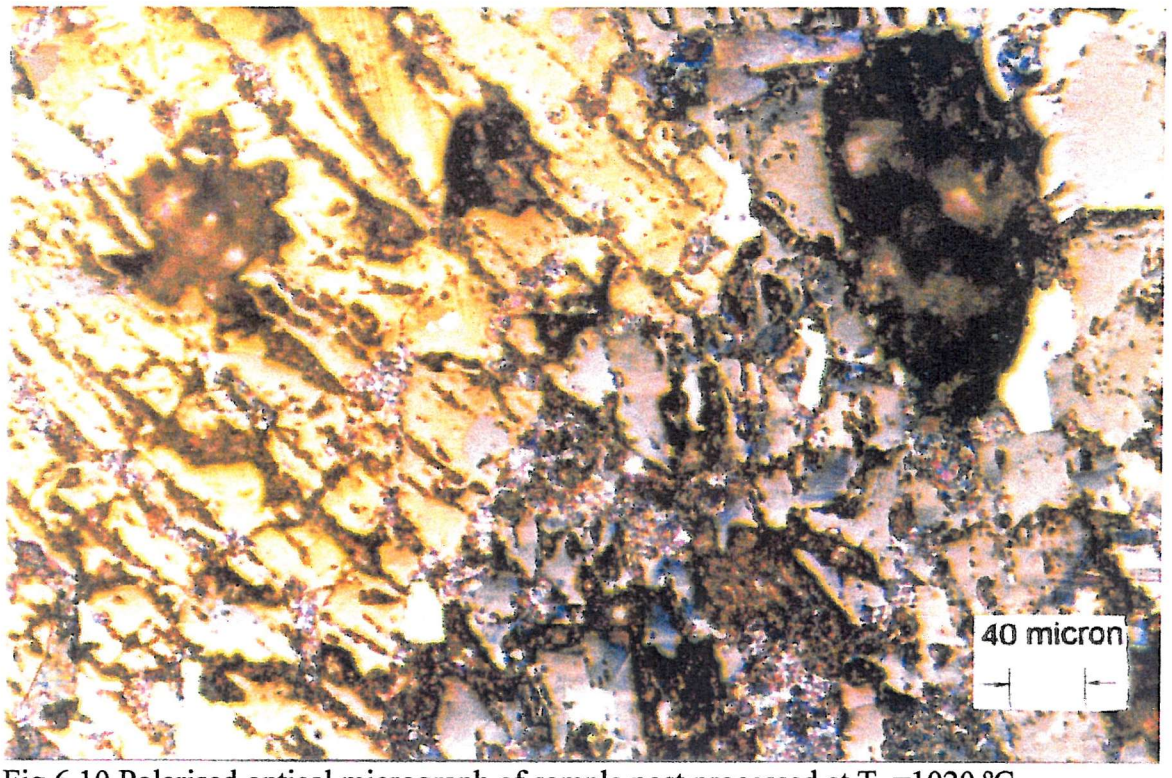

Fig 6.10 Polarised optical micrograph of sample post processed at T_m=1020 °C

As discussed previously, the samples lost some liquid phases during processing. This was expected because the samples are multi-granular, hence the presence of liquid phased at grain boundaries or in separate inclusions is normal. However, the sample with T_m=1020 °C lost considerably more liquid than the other samples. The micrographs shown above (Fig6.6 to Fig 6.10) indicate that this sample has a greatly differing microstructure in comparison with the other post processed samples and the control sample. For all other values of T_m the microstructure remains similar to that of the control sample. For T_m=1020 however the grains appear considerably smaller, with a high degree of porosity and high percentage of non-123 phases. This evidence would suggest that a degree of melting has taken place in this sample, ruining the microstructure and suggesting an upper limit for this process. However, for all T_m equal to and below 1000 °C no obvious change in structure has occurred. Considering that previous experiments have indicated that fast heating to any temperature above 938 °C results in decomposition, these results would suggest that the slow heating has allowed a gradual compositional shift without causing large scale melting.

In order to investigate further it is necessary to look at the composition of the processed material in comparison with the control sample. In order to do this the samples were

examined using a scanning electron microscope (S.E.M). By collecting the back scattered electrons it is possible to form a spectra and so identify the elements present and their relative quantities (EDX). Shown in Fig 6.11 are two plots of the ratio of Sm to Ba found in these samples.

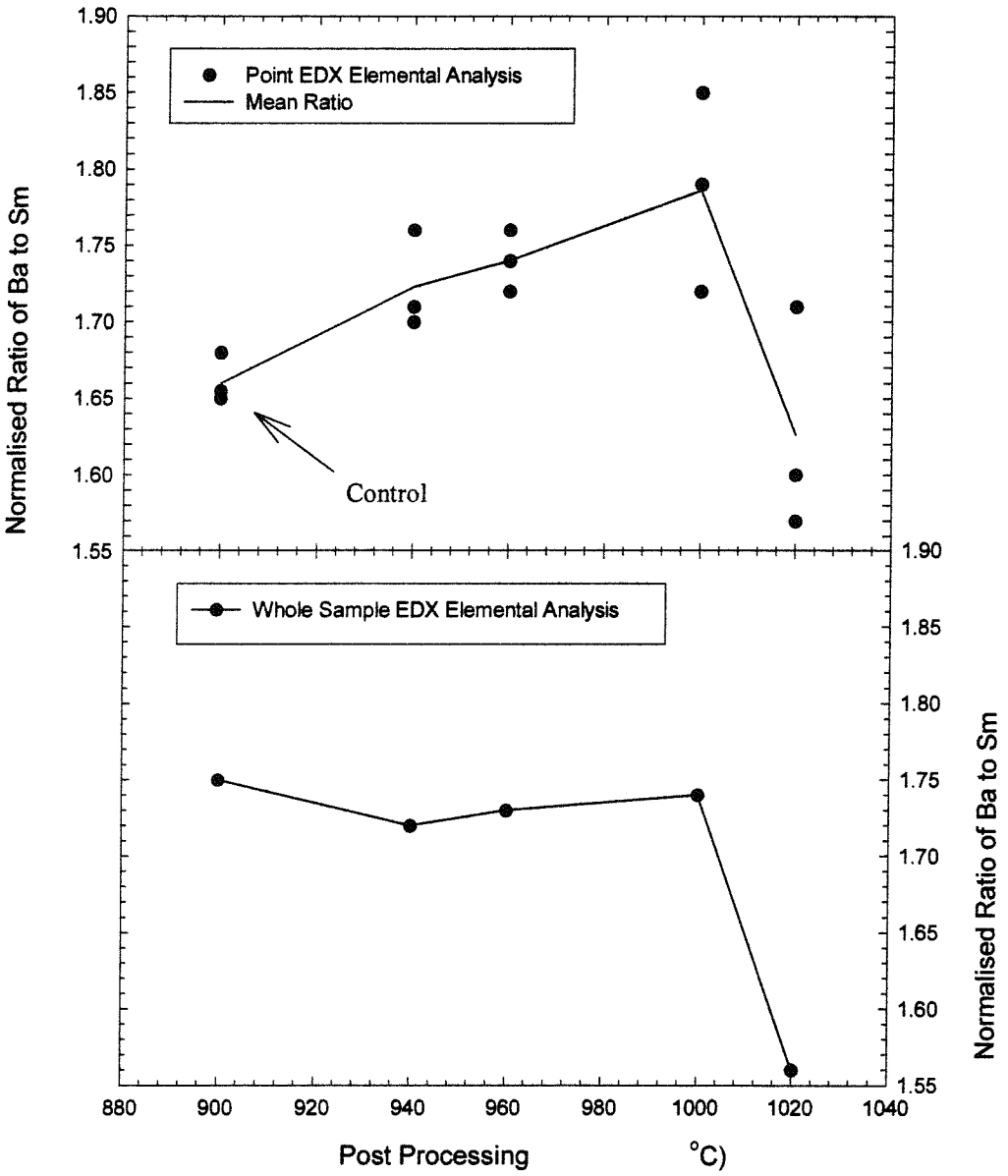

Fig 6.11 EDX data illustrating the ratio of Ba to Sm in various control and post processed samples of Sm123.

The first set of data was gathered by taking spectra at randomly selected points within different grains on the surface of the samples. The second set of data was acquired by taking a spectra from the entire surface of the samples. Examination of the first plot reveals an obvious trend where the ratio of barium to samarium increases with increasing T_m up until 1000 °C. Somewhere between 1000 °C and 1020 °C a limit is reached above which the ratio shows a sharp decrease. The second plot illustrates an almost constant ratio until, as before, a limit is reached between 1000 °C and 1020 °C when a sharp drop occurs. Combined this with the photographic evidence presented earlier and we may conclude that this is the point at which large scale decomposition occurs. For temperatures below this however, it would appear that the composition within the grains is changing whilst the composition of the sample as a whole remains unchanged. This would suggest that, as the composition is moving away from the Sm rich region of the phase diagram towards a 123 stoichiometry, the samarium ions on the barium sites are being replaced.

6.6 Conclusion

A novel method for the control of Sm/Ba substitution has been developed and discussed. Post processing of melt grown Sm123 in a reduced oxygen atmosphere has been successfully employed to increase the ratio of Ba to Sm within the crystal structure. Control over this ratio is important as the superconducting properties of the material are highly dependent on this.

6.7 References

1. M. Murikami, *Melt processing High-Temperature Superconductors* (Singapore World Scientific 1993)

2. Y. Itho, Y, Yanagi, T, Oka, S. Harada, Y. Yamada and U. Mitzutani, *Jpn J. Appl. Phys.* Vol. **5** (1995)

3. N. Alford, T. W. Burton and J. D. Birchall, *Supercond. Sci. Technol.*, Vol. **3** (1990)

4. W. Lo, D. A. Cardwell, C. D. Dewhurst and S. -L. Dung, *J. Mater. Res.* Vol. **11**, 786 (1996)

5. S. Marinel, J. Wang, I. Monot, M. P. Delamare, J. Provost and G. Desgardin, *Supercond. Sci. Technol.* Vol. **10**, 147 (1997)

6. W. Lo, D. A. Cardwell, S. –L. Dung and R. G. Barter, *J. Matter. Sci.* Vol. **30**, 3995 (1995)

7. D. Shi, D. Qu, S. Sagar and K. Lahiri, *Appl. Phys. Lett.* Vol. **70**, 3606 (1997)

8. M. Morita, S. Takebayashi, M. Tanaka, K. Kimura, K. Miyamoto and K. Sawano, *Adv. Supercond. Sci. Technol.* Vol. **3**, 733 (1991)

9. C. H. Choi. Y. Zhao, C. C. Sorrel, M. La Robina and C. Andrikidis, *Physica C*, **269** (1996)

10. N. Ogowa, I. Hirabiashi and S. Tanaka, Physica C, **177**, 101 (1991)

11. P. McGinn, W. Chen, N. Zhu, L, Tan, C. Varanasi and S. Segupta, *Appl. Phys. Lett.*, **59**, 120 (1991)

12. N. Ogowa, and H. Yoshida, Adv. Supercond., **4**, 132 (1992)

13. N. Ogowa, I. Hirabiashi and S. Tanaka, *Physica C*, 185-189, 2409 (1991)

14. S. J. Manton, C. Beduz, Y. Yang, K. Deligiannis, P. A. J. deGroot, *Mater. Sci. Eng. B*, **B53** (1998)

15. M. Murikami, N. Sakai, T. Higuchi and S. I. Yoo, Supercond. Sci. Technol, **9** (1996) 1015-1032

16. P. Schatzle, W. Bieger, U. Wiesner, P. Verges and G Krabbes, Supercond. Sci. Technol. **9** (1996) 869-874

17. D. I. Grigorashev, E. A. Trofimenko, N. N. Oleynikov and Yu D Tretyakov, *IOP Publishing Ltd.* (1997)

18. L. Dimesso, M. Marchetta, G. Calestani, A Migliori and M. Masini, Supercond. Sci. Technol. **10** (1997) 347-355

Chapter 7: Rejoining of Single Grain Melt Textured Bulk $YBa_2Cu_3O_{7-X}$

7.1 Introduction

There are many potential applications for bulk YBCO, however many of them require large or shaped samples of extremely high quality[1-3]. It is reasonably straightforward to produce large, complex devices from sintered YBCO. However, multi-granular bulk material processed in this fashion displays very poor superconducting transport properties due to the low value of the intergranular critical currents. Hence, the possibility of constructing useful devices in this manner is limited.

The development of the melt textured growth process represented a substantial step towards the production of bulk high temperature superconductors with properties good enough for applications[4-8]. Using this process it is possible to produce large pieces of dense material of higher quality than is obtainable with the sintering process. Many applications can still not be realised however as, although grain sizes are much larger than in the sintered material, weak links caused by grain boundaries still limit the obtainable critical currents.

The implementation of the seeded melt textured growth process finally eliminated the problems associated with grain boundaries by facilitating the production of large, high quality, single grains. However, due to the nature of the thermal cycling and the crystal growth kinetics of the material it is difficult to produce single grains in any but the simplest of shapes. Also, considerable deformation can occur during processing, hence the final product will be of different dimensions to the precursor pellet. With regards to superconducting properties, a good quality material with a high degree of uniformity is necessary for most applications, conditions which can only be met by relatively small discs of superconductor grown by this method. It has been demonstrated that the superconducting properties of seeded melt textured monoliths degrade quickly with diameter and depth. This is an inhibiting factor when preparing large single pieces suitable for machining.

In this chapter a preliminary study of a possible solution to this problem is presented. It has been proposed that in order to bypass the reduction in quality associated with the growth of large single domains we instead create high quality superconducting joints so that devices may be built from high performance, intermediate sized pellets.

Rare earth 123 high temperature superconductors show very little variation in structure whilst demonstrating a wide variety in crystal growth temperature[9]. This would seem to make them ideal for the production of composite systems where ceramics with a lower processing temperature are used to join already grown materials with a higher peritectic. However, this approach does have certain limitations. For example, if one were considering using YBCO to join NdBCO one would have to account for the difficulties which would be encountered when oxygenating, as their ideal annealing temperatures differ by around 200°C. This, combined with the ease of processing and good superconducting properties led to the selection of YBCO as the bulk medium and ErBCO as the joining agent.

The feasibility of re-joining multi-granular bulk YBCO using YbBCO to repair a cut has been demonstrated by Schmitz et al using an infiltration method[10]. This method involves allowing molten liquid and 123 phases (black powder) to permeate into a packed powder of 211 phases (white powder). In their study they were able to demonstrate clearly a degree of alignment between the material on either side of a cut and the newly formed material in the gap. They also observed, as have several other authors, the microstructural benefits of the infiltration method. Viswanath et al have demonstrated the superiority of the distribution of Sm211 inclusions in SmBCO grown via infiltration over that grown in a standard melt growth procedure[11].

7.2 Experimental: Part One

The powder mixtures selected for this study were chosen based upon the published literature describing work undertaken with other materials[11]. The white powder, i.e. the material to be packed into the region to be re-joined, consists of $5Y_2O_3$ + $BaCuO_3$, whilst the black powder, the material which will melt and infiltrate into the white powder, is a mixture of Er123 + 2CuO + 3BaCuO (see Fig.7.5). Re-joining was attempted with other powder mixtures, the results of which are discussed later.

In order to gain some idea of the ideal ratio of these two powder mixtures with respect to the production of high quality bulk material a series of experiments were undertaken. 4mm diameter, 1mm high pellets of white powder were pressed using a cold uni-axial press. Pellets of the same diameter were then pressed from the black pellets. These pellets varied in mass so as to produce varying molar ratios between the white and the black powders. The black pellets were then placed on top of the white pellets and thermally processed on an yttria stabilised zirconia substrate. A thermal cycle was selected based on trials which indicated a good balance between grain size and liquid loss. A ramp rate of 60°/hr was used up to a temperature of 990°C. This temperature was then held for 15 hrs before cooling at 10°/hr to temperature of 950°. The sample was then cooled to room temperature at a rate of 60°/hr. All samples were processed in air.

The ratio of white to black powder was varied from 1:1 to 1:6. After processing samples were cut from the substrate and annealed for 100 hrs in flowing O_2 at 500°C. Following this, samples were polished and examined using a polarising optical microscope. Three factors were used to judge the success of each ratio; grain size, microstructure (i.e. distribution of 211 phases and impurities) and excess liquid. Liquid phases should be kept to a minimum so as to reduce the effects of the joining process on the surrounding bulk.

Using these criteria, the ratio of 1:4 was chosen. Polarised optical micrographs of several samples produced with different ratios can be seen in Fig. 7.1 to Fig. 7.4. Fig. 7.1 is a medium magnification image illustrating the poor macroscopic structure of a sample fabricated with a ratio of 1:2. Note the lack of large grains, the presence of voids and the large quantity of Y211 present in the bulk. The proportion of Y211 is so

large that many individual inclusions have ripened to the point where they join together. This kind of microstructure is typical of samples prepared with insufficient liquid phases. This arises because during melt growth the liquid phases dissolve Y211 and form bulk Y123, hence if the proportion of liquid phase is not large enough no dissolution will take place and instead the remaining liquid will be used to convert the Y_2O_3 into Y211. Fig.7.2 and Fig.7.3 are medium and high magnification micrographs of sample prepared with a ratio of 1:3. Although the structure is superior in comparison to that shown in Fig.7.1 the proportion and size of the Y211 inclusions within the bulk is still too large. Fig.7.4 is a high magnification picture of a sample produced with a ratio of 1:4. The microstructure has an even, fine distribution of 211 phase and no inclusions of other phases such as barium cuprates. Samples produced with a ratio of 1:5 show a similar microstructure but due to the increased proportion of liquid phases increased wetting of the substrate and deformation of the pellet was observed. A ratio of 1:6 shows similar results but inclusions of liquid phase are present within the bulk. It is interesting to note that for ratios around or less than 1:1 infiltration does not take place. Instead, the pellets remain separate, the white pellet only absorbs enough Ba and Cu to form Y211 and the black pellet undergoes considerable shrinkage and forms porous Er123/211 composite. This may indicate the necessity of a "wet" phase needed for any migration process and is discussed in more detail later.

It is believed that the high quality of the microstructure observed in the pellets with white to black ratios of 1:4 and 1:5 can be attributed to the way in which nucleation centres are evenly distributed throughout the bulk. The white pellet is able to act as sponge, soaking up liquid phases into the voids left after pressing. The result is an even distribution of nucleation centres spread throughout the material. The liquid phases will dissolve the white phase, which will mostly have been converted to Y211, raising the peritectic of the melt up until the point where crystal growth is initiated. It is proposed that the growth front will then continue to dissolve the Y211 phase as it spreads, trapping inclusions of yet to be dissolved Y211 as it propagates.

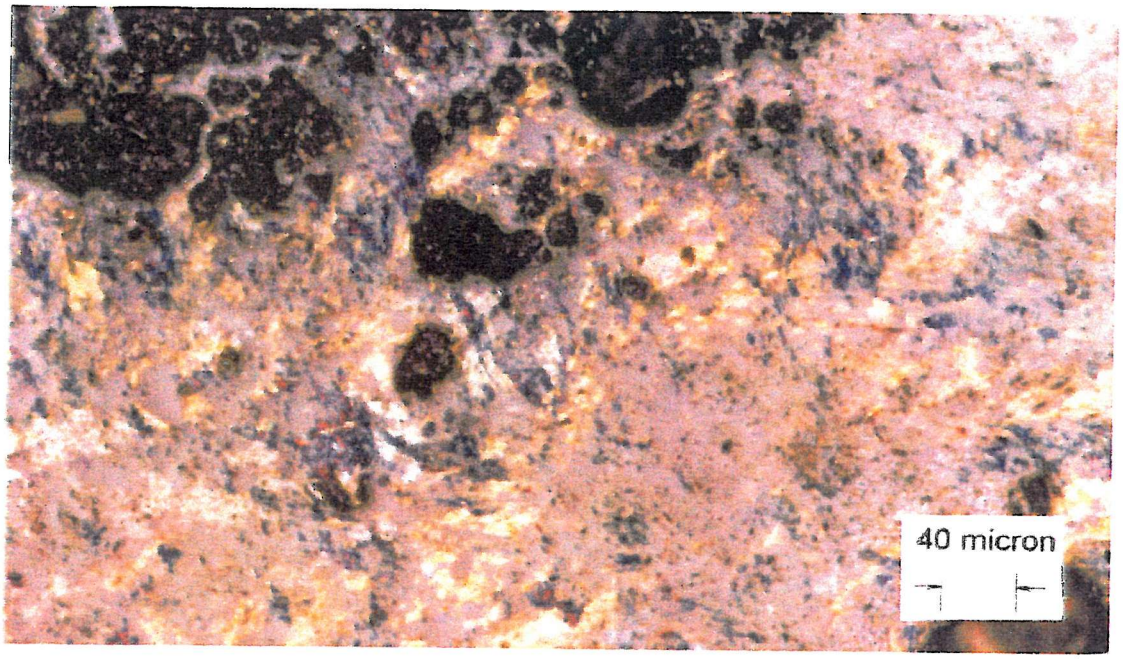

Fig.7.1 Polarised optical micrograph of the microstructure of a sample produced with a ratio of 1:2

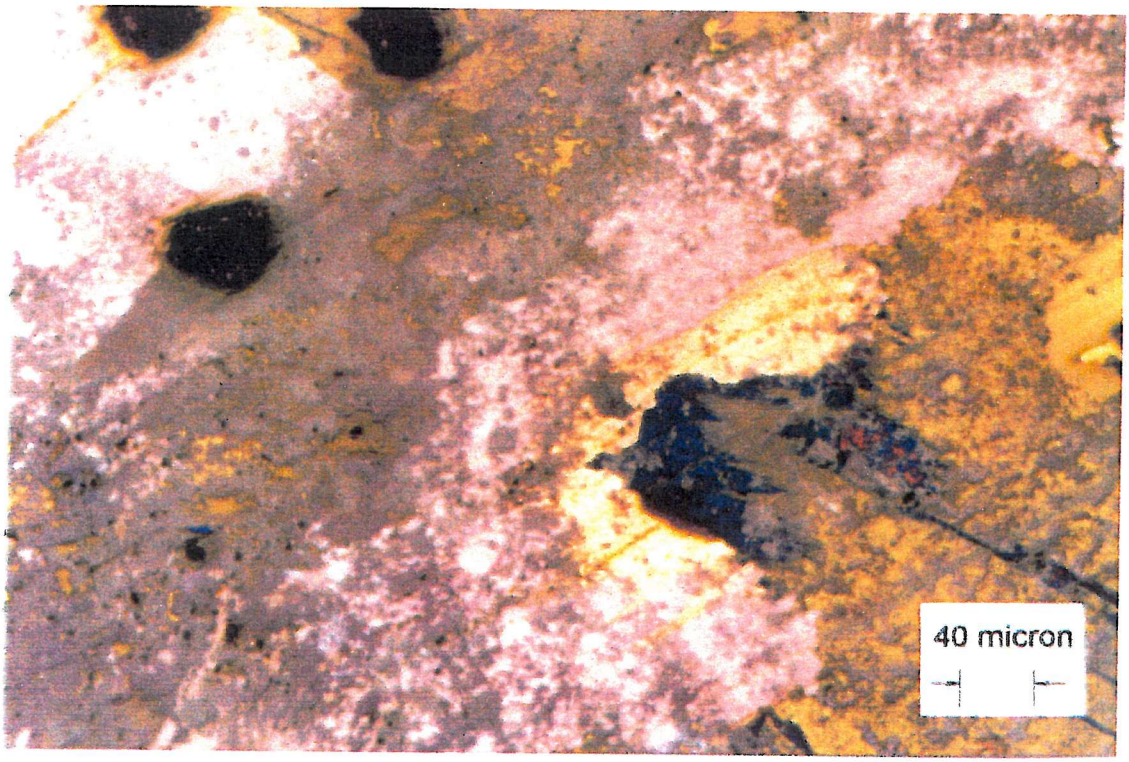

Fig.7.2 Polarised optical micrograph of the microstructure of a sample produced with a ratio of 1:3

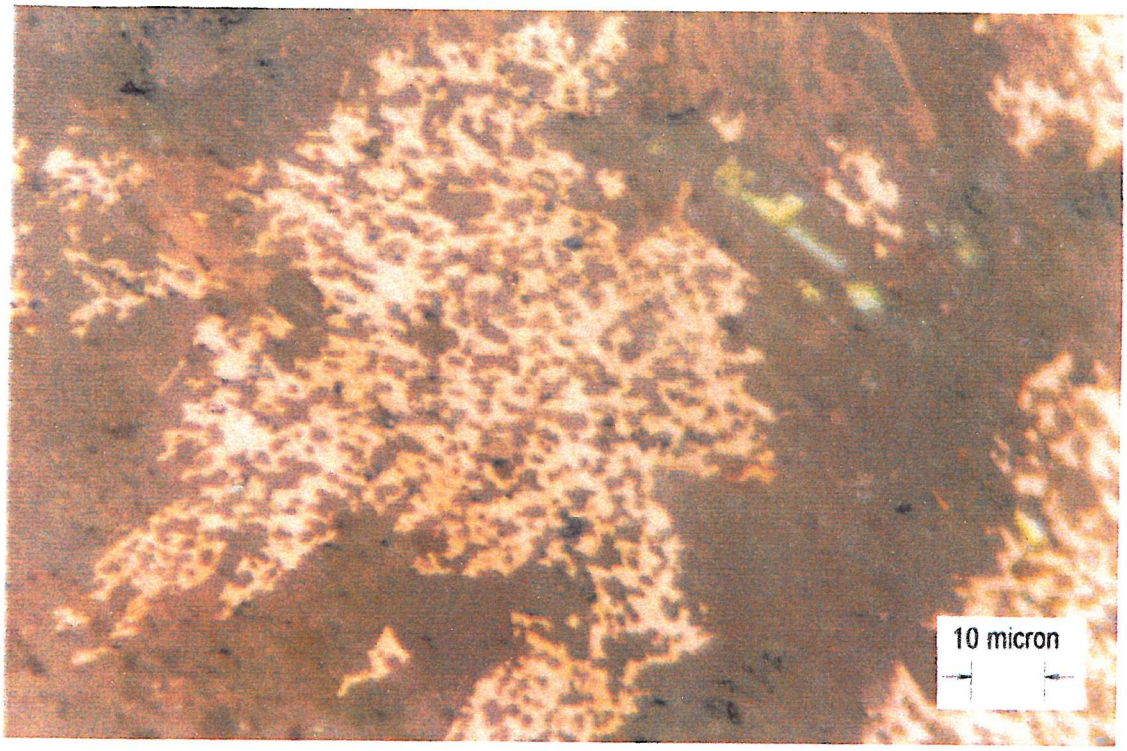

Fig.7.3 Polarised optical micrograph of the microstructure of a sample produced with a ratio of 1:3

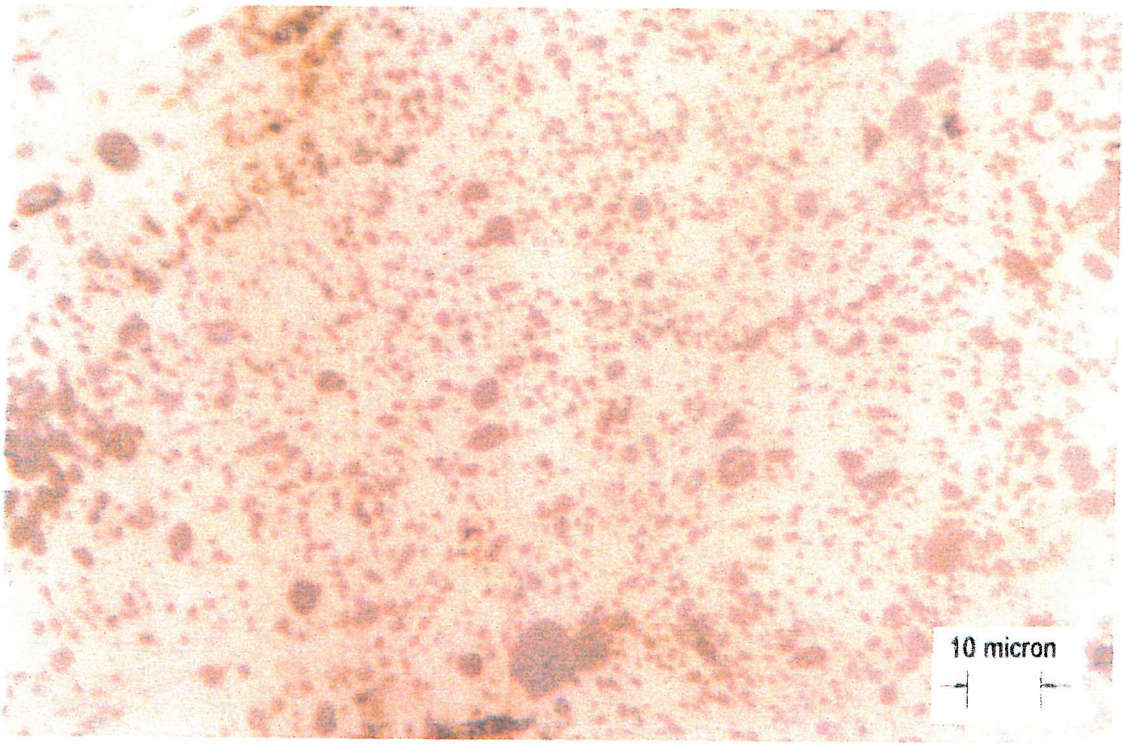

Fig.7.4 Polarised optical micrograph of the microstructure of a sample produced with a ratio of 1:4

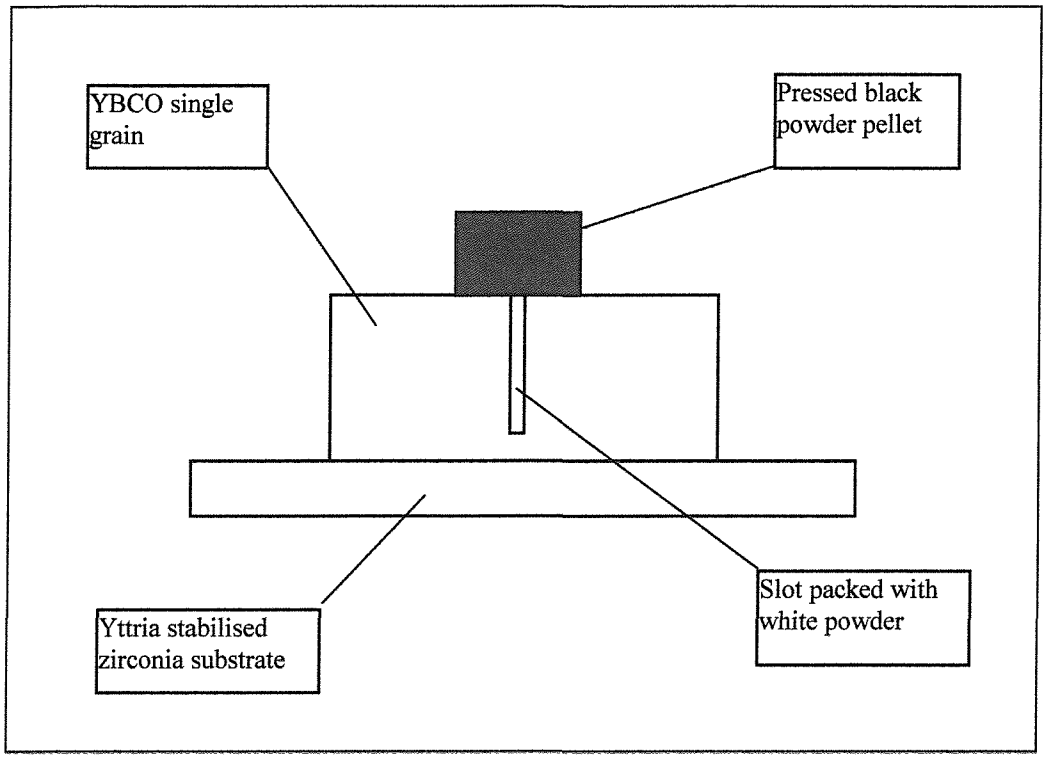

Fig. 7.5 Schematic of re-joining configuration

7.3 Experimental: Part Two

Large, single grains of bulk YBCO were prepared using a standard seeded melt texturing process. Powder mixtures of 0.85Y123 + 0.15Y211 doped with 0.5% wt. platinum were pressed into pellets of 1 inch in diameter and approximately 10 mm in height. These pellets were then sintered at 930 °C in air in order to reduce deformation during thermal processing. A small single crystal of Sm123 was used as a seed placed at the centre of the pellet. The pellet was then processed in a vertical furnace capable of applying a horizontal temperature gradient and a cold finger was used to ensure preferential nucleation around the seed area.

After processing, the pellets were polished and their grain structure analysed. Single grains of suitable size were then sectioned using a wafering diamond saw. These sections, typically of around 6×10×8mm, then had a slot cut into them using a 150 μm thick wafering diamond saw blade. The slot was cut to a depth of around 7mm and

then cleaned. The gap was then packed with white powder and a pressed pellet of black powder placed on top. A schematic of this configuration can be seen in Fig. 7.5. This arrangement was then placed in a standard tube furnace and thermally processed with a cycle identical to that described in section one.

Although it was found previously that the optimum ratio of white to black powder was 1:4, variation in the amount of black powder used for re-joining was necessary due to the differences in the processing conditions. Firstly, the liquid phases have to permeate into a small slot, therefore a larger proportion of liquid phase is lost in the form of surface run off. Also, the bulk material itself will absorb liquid phases and so further reduce the amount of material available for the re-joining process. This resulted in the ratio being increased to 1: 10.

After re-joining the samples were annealed for 100 hrs in flowing O_2 at 500°C and then polished in order to allow for microstructure analysis.

7.4 Microstructure of Rejoined Samples

Shown in Fig. 7.6 is a polarised optical micrograph of a typical re-joined grain. The repaired region is the vertical section in the centre of the illustration. There are no visible grain boundaries, no additional grains and no signs of impurities. The newly grown region appears continuous, dense and with no degree of misalignment. In addition, the microstructure of the joint is considerably better than the surrounding bulk. The distribution of 211 inclusions is exceptionally fine, an important factor when assessing the quality of RE123 superconductors.

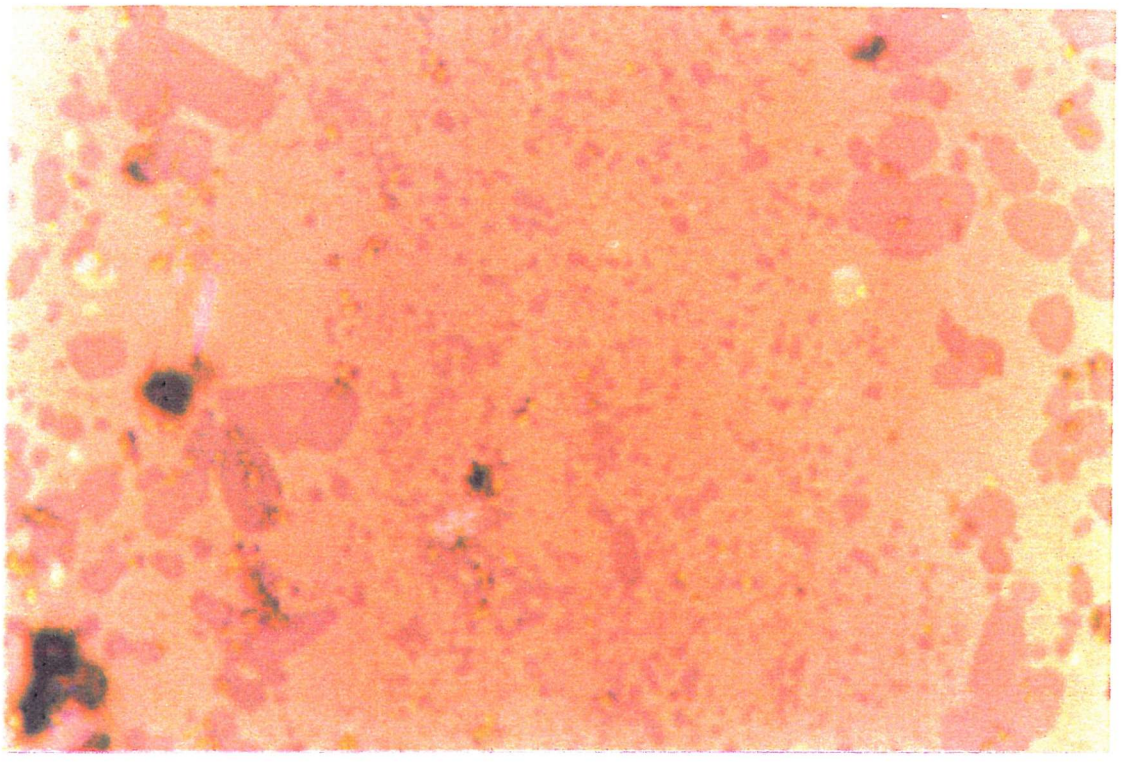

Fig.7.6 Polarised optical micrograph of re-joined region. The section of interest is the strip of fine Y211 particles which run vertically down the centre of the picture.

Reproduced in Fig. 7.7 and Fig. 7.8 are polarised optical micrographs of a different sample. It can be seen from Fig. 7.7 that the inter-planar separation often observed in between the ab planes of bulk YBCO runs continuously through the repaired region. This has probably occurred due to the orthorhombic to tetragonal phase transition which takes place at around 700°C. Although care must be taken to avoid this, the fact that the cracks continue into the rejoined region illustrates how well the new material has integrated into the slot. Fig. 7.8 is a micrograph concentrating on one boundary between the old and the new material. It can be seen from this illustration that in some places the density and diameter of 211 phase at the boundary region is almost large enough to form a non-superconducting boundary. The reasons why this occurred in this instance need to be investigated and understood before applications can be considered. It is possible that this phenomena results from the dissolution of the already formed bulk 123 material, followed by extended ripening of the already present which occurs before the peritectic of the molten compound increases to the point where the re-solidification of the 123 may occur. This would imply that precise

control over the amount of liquid phases, the homogeneity of their distribution and the dwell temperature will be essential for continuation of this work.

Fig. 7.9 shows a sample that has been re-joined using a slight variation of the powder composition. In this case the white powder packed into the slot consists of $5Y_2O_3$ + BaO_2 instead of $5Y_2O_3$ + $BaCuO_3$. It is apparent that the joining process has taken place, but the new material appears less dense than that found with the usual powder composition. Also, the size of the 211 inclusions within the new material are not as refined as those normally observed. However, there is no sign of any increase in size or density of the 211inclusions at the interface region between the old and new material.

The growth mechanisms taking place during this process have been investigated using electron back scattering imaging and elemental analysis. Because of its higher atomic mass Erbium shows up much more brightly than any other of the elements present. Fig.7.10 clearly shows how the distribution of Erbium varies with distance from the repaired region. The Erbium has in fact penetrated a considerable distance into the bulk, although this effect has probably been exacerbated because the sample under examination was porous to begin with. Even so, the effect of this process on the surrounding bulk and the distance over which changes are effected are important factors to be considered, as alterations to the already grown material are to be avoided.

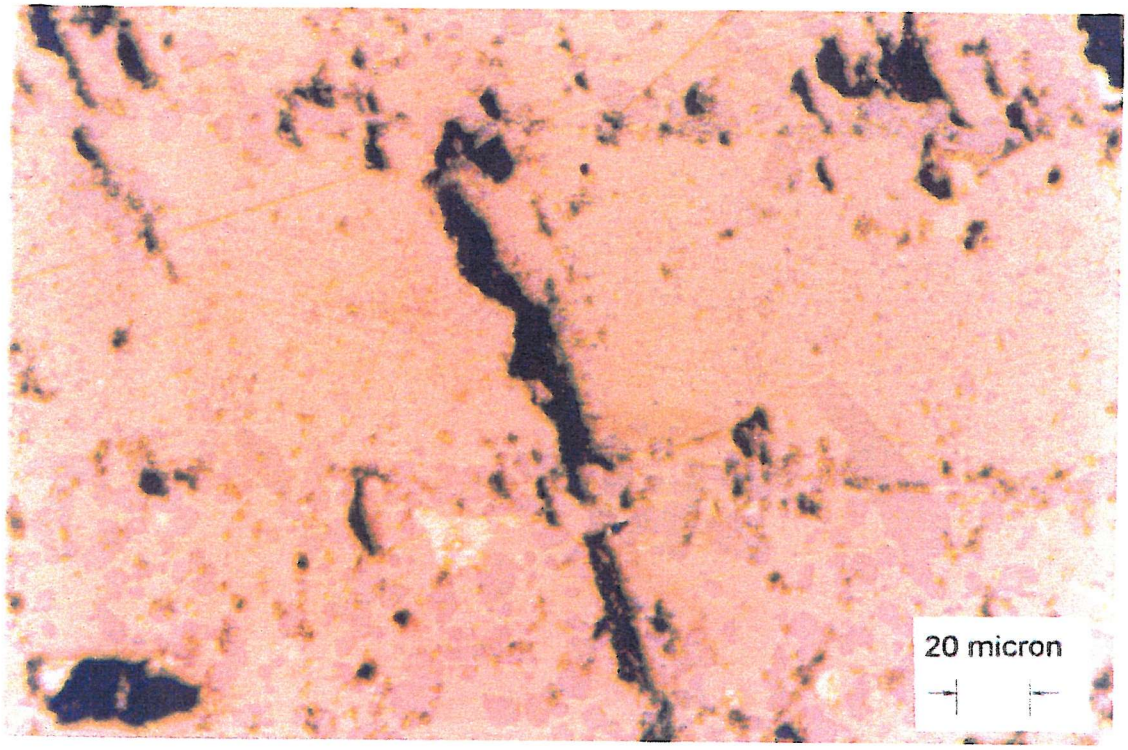

Fig.7.7 Polarised optical micrograph of re-joined region illustrating the strong bond between surfaces.

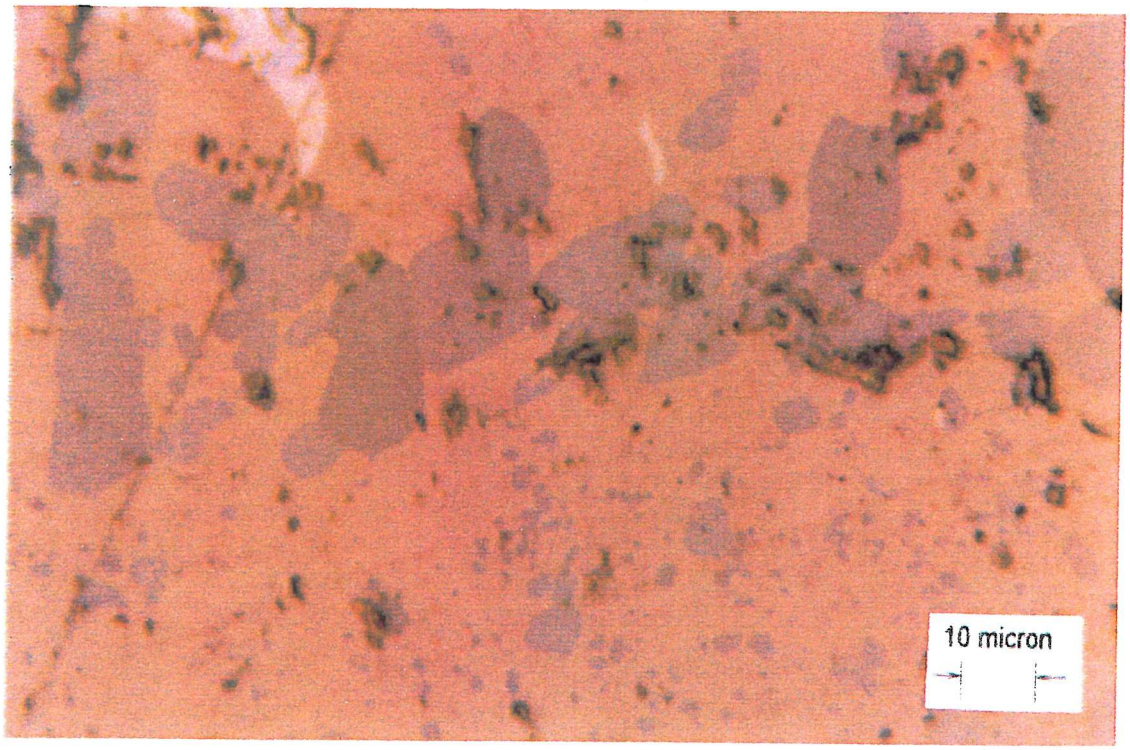

Fig.7.8 Polarised optical micrograph of high 211 density found at some boundaries.

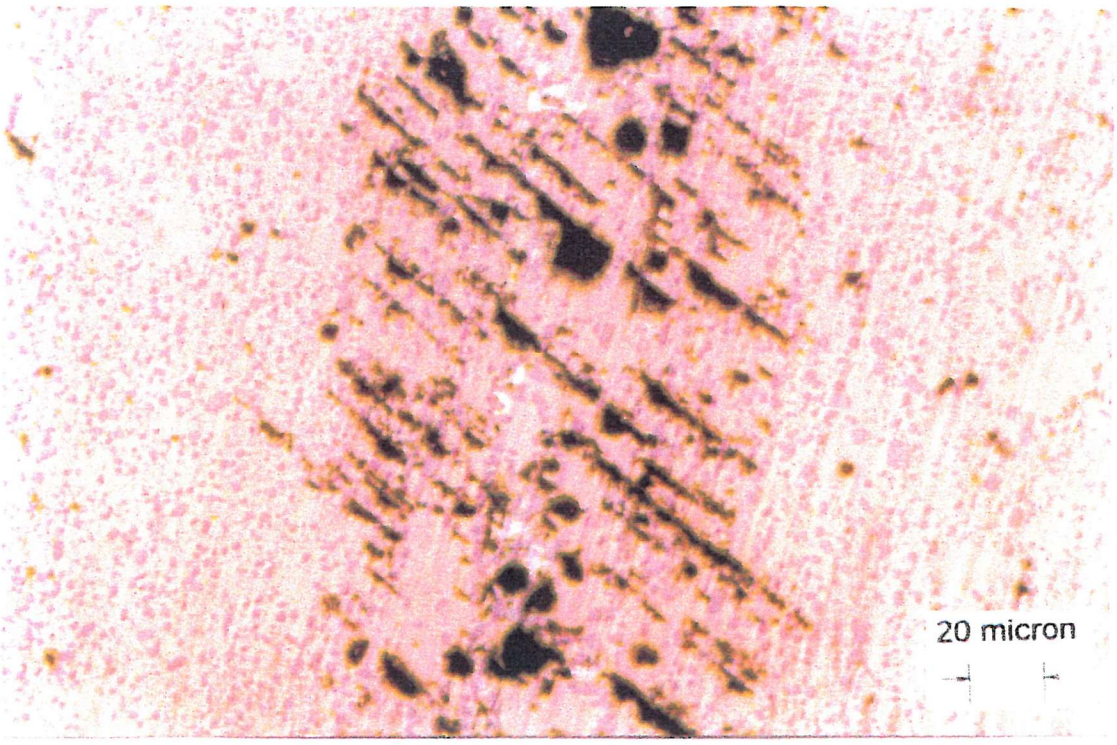

Fig.7.9 Polarised optical micrograph of region re-joined with different powder composition.

Fig. 7.11 is a close up image of the structure inside the gap. Again the bright areas correspond to regions of high Erbium concentration. The ring structure of the bright regions is immediately apparent. Back scatter spectra taken from the three points numbered in Fig. 7.11 can be seen in Fig. 7.12, Fig. 7.13 and Fig. 7.14. Fig. 7.12 shows that these regions correspond to regions of Er/Y123 phase. The dark regions inside the rings were found to be Y211 inclusions (Fig. 7.13) whilst the dark areas outside the rings correspond to Y123 material (Fig. 7.14). Why the Erbium appears to agglomerate around the Y211 inclusions is not known. It is possible that this region of high Erbium concentration corresponds to a zone of phase migration, i.e. a region in which the Erbium rich liquid dissolves the Y211 phase allowing the Yttria to diffuse through the liquid and eventually solidify into Y123 material.

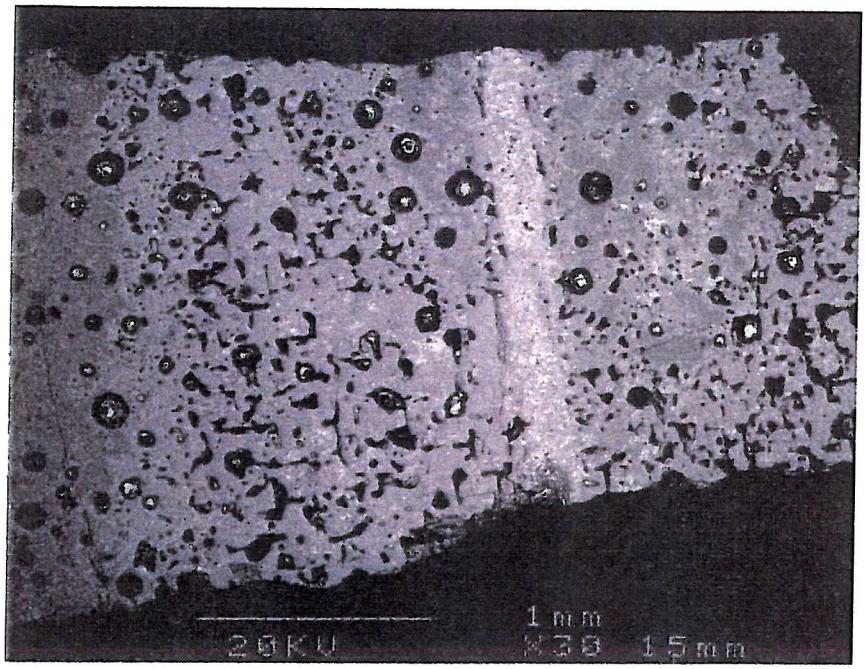

Fig.7.10 Low magnification electron back scatter image of re-joined sample.

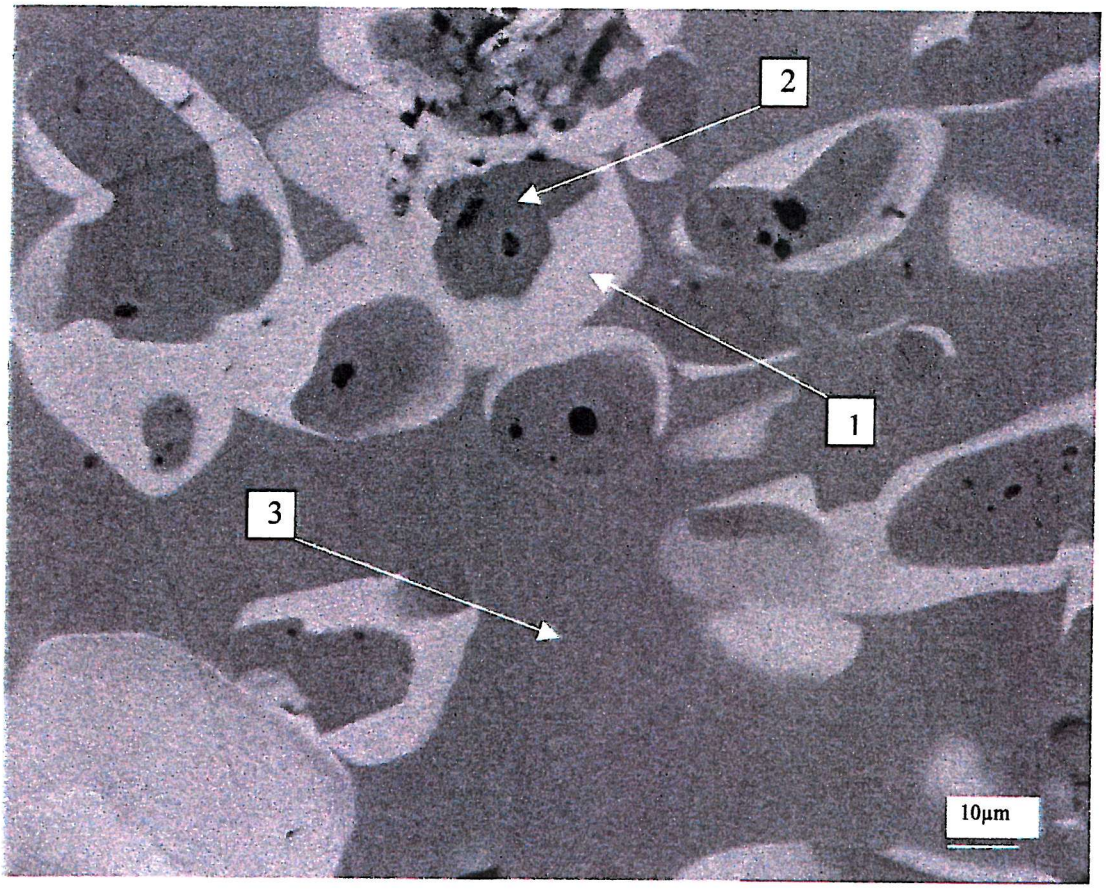

Fig.7.11 Close up electron back scatter image of the structure within the repaired region.

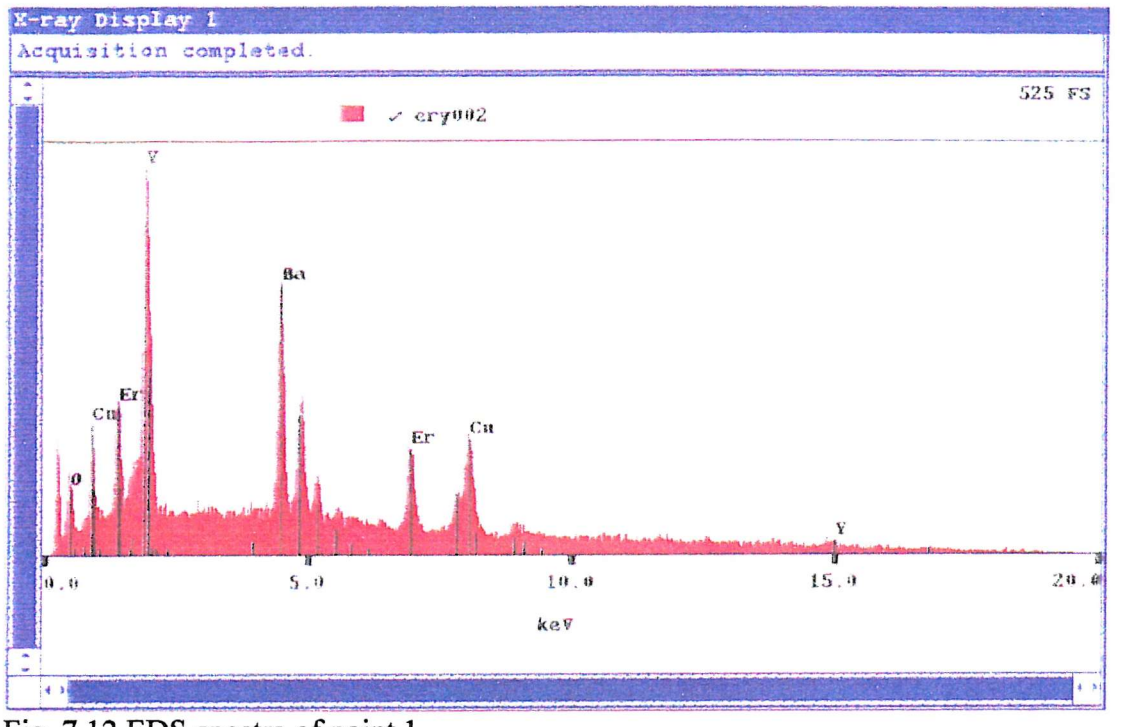

Fig. 7.12 EDS spectra of point 1.

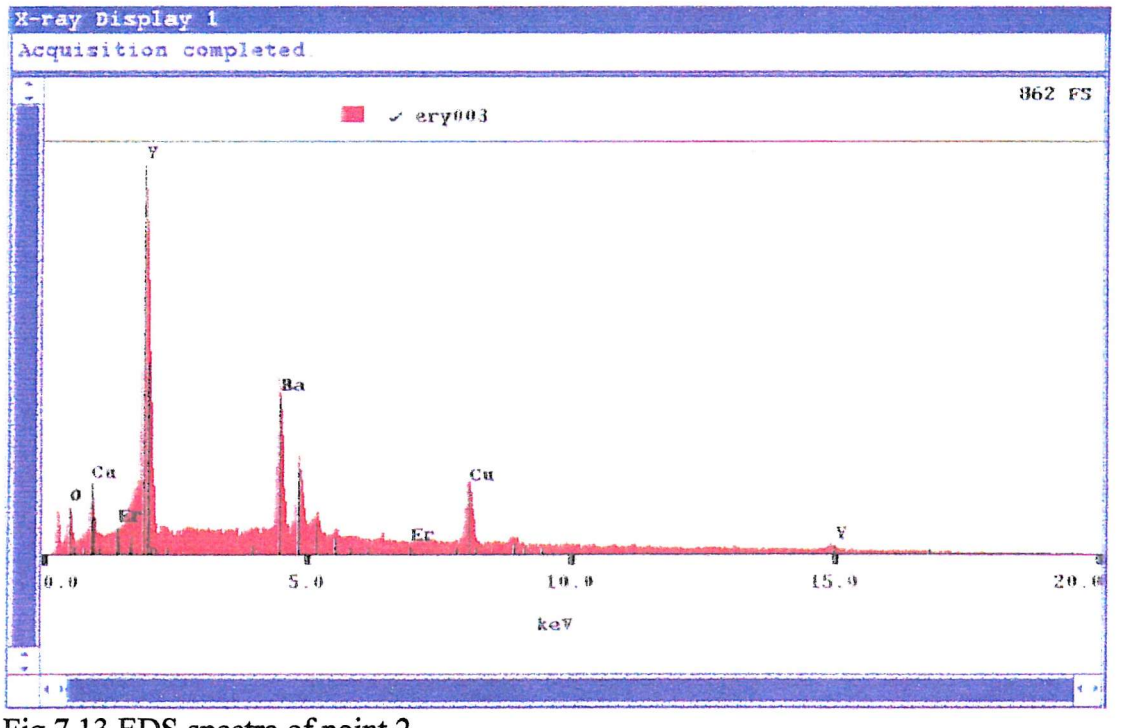

Fig.7.13 EDS spectra of point 2.

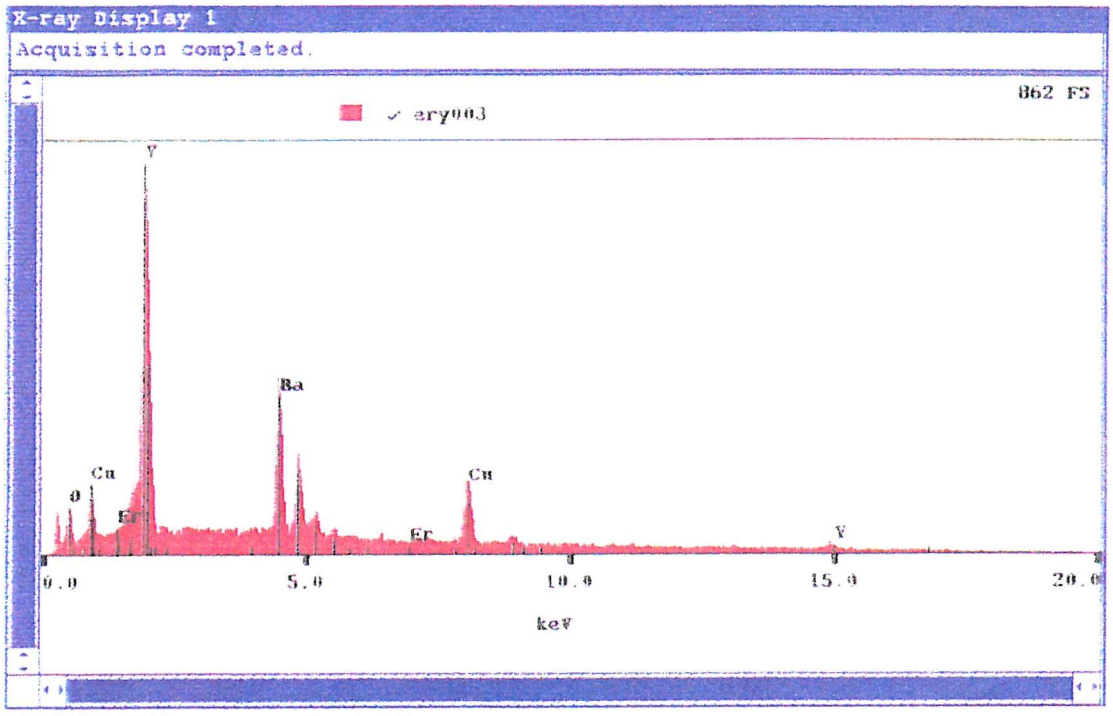

Fig.7.14 EDS spectra of point 3.

In an attempt to more fully understand how the new material nucleates and so repair regions without any grain misalignment a sample was produced where a 100 micron slice of single grain YBCO was placed into the slot before the rejoining process took place. The slice had a grain alignment perpendicular to that of the surrounding bulk. A polarised optical micrograph of the resulting product can be seen in Fig. 7.15. The ninety degree misalignment of the grain makes it extremely easy to differentiate between the slice and the bulk material, with the slice being the bright region running diagonally across the photo. To the left of the region it is possible to observe solidified liquid phases, i.e. barium cuprates, hence no superconducting joint has been formed. However, to the right hand side of the slice no phases are present to form a boundary between the two grains. At some points along the joined region sharing of 211 inclusions can be seen, illustrating the fact that a forming of new material has taken place. In this picture the perpendicular twinning planes characteristic of ab alignment are clearly visible on both sides. The regions close to the slice do not display any large inclusions of 211 phase, a characteristic which has been identified as indicating newly formed material. No similar observation can be made for material with an identical alignment to the slice. Therefore one may conclude that nucleation occurs at the boundary between the molten and the already formed material. The crystal then grows

preferentially in the ab direction, which is to be expected as in the normal melt growth procedure the crystal growth rate is far higher in the ab direction than in the c direction. This confirms that dissolution of the already grown material in order to induce an upwards shift in the peritectic of the melt is a critical factor in this process.

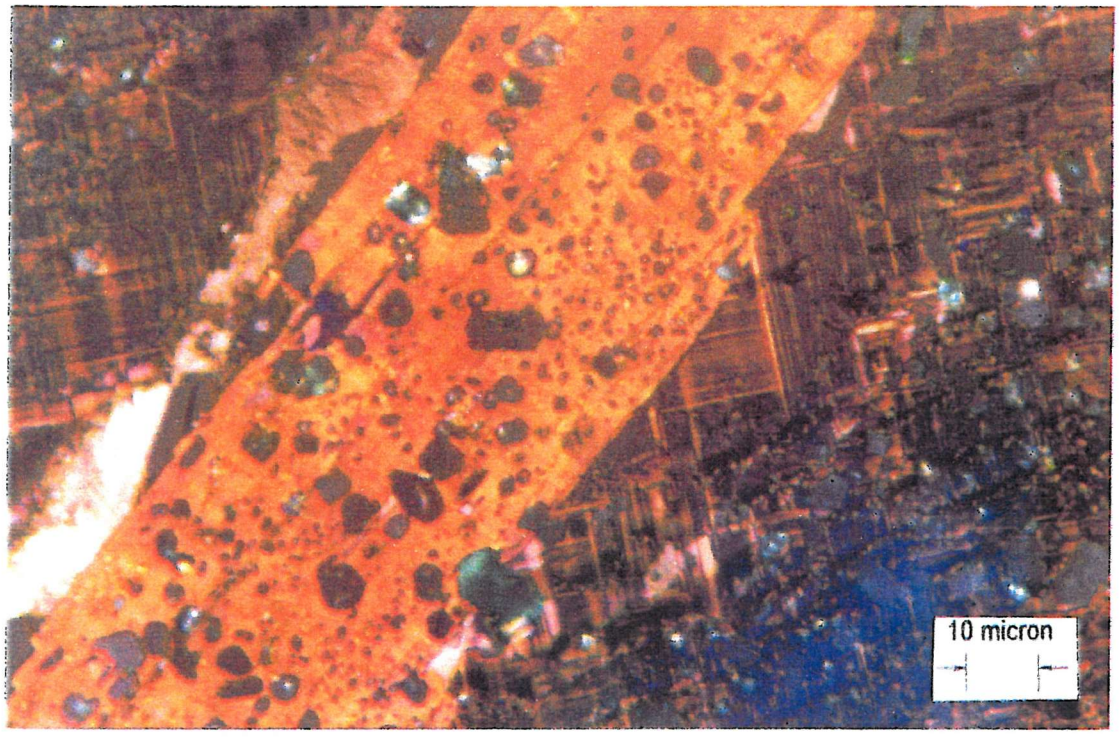

Fig.7.15 Polarised optical micrograph of perpendicular grain boundary.

7.5 Conclusions

The possibility of joining single grains of RE123 materials considerably enhances the applicability of bulk materials with respect to large scale applications. High quality superconducting joints produced via an infiltration method have been fabricated and studied.. This process takes place at a temperature below the peritectic of Y123 and thus the crystal structure of the original bulk remains unchanged. The newly formed Er/Y123 material displays the same orientation as the original grain. Also we have shown that in general the Y211 inclusions are smaller in the rejoined region than in the surrounding bulk. Microstructure and compositional data are presented and discussed.

The microstructure of the sample shown in Fig. 7.6 would seem to make this process ideal for joining together single grains of bulk YBCO without any grain boundaries. However, before this becomes a reality the mechanisms involved need to be understood and several considerations have to be addressed. For example, the quality of the joint is not as reproducible as one would like and the quality through out the sample does show variation.

It is hoped that continuation of this work will lead to the development of a process to allow the fabrication of large, complex superconducting devices suitable for many applications.

7.6 References

1. N. Alford, T. W. Burton and J. D. Birchall, *Supercond. Sci. Technol.*, Vol. **3** (1990)

2. Y. Itho, Y, Yanagi, T, Oka, S. Harada, Y. Yamada and U. Mitzutani, *Jpn J. Appl. Phys.* Vol. **5** (1995)

3. M. Murikami, *Melt processing High-Temperature Superconductors* (Singapore World Scientific 1993)

4. D. Shi, D. Qu, S. Sagar and K. Lahiri, *Appl. Phys. Lett.* Vol. **70**, 3606 (1997)

5. S. Marinel, J. Wang, I. Monot, M. P. Delamare, J. Provost and G. Desgardin, *Supercond. Sci. Technol.* Vol. **10**, 147 (1997)

6. W. Lo, D. A. Cardwell, S. –L. Dung and R. G. Barter, *J. Matter. Sci.* Vol. **30**, 3995 (1995)

7. W. Lo, D. A. Cardwell, C. D. Dewhurst and S. -L. Dung, *J. Mater. Res.* Vol. **11**, 786 (1996)

8. M. Morita, S. Takebayashi, M. Tanaka, K. Kimura, K. Miyamoto and K. Sawano, *Adv. Supercond. Sci. Technol.* Vol. **3**, 733 (1991)

9. M. Murikami, N. Sakai, T. Higuchi and S. I. Yoo, Supercond. Sci. Technol, **9** (1996) 1015-1032

10. G. J. Schmitz A. Tigges and J. C. Schmidt, Supercond. Sci. Technol. **11** (1998), 73-75

11. N.V.N Viswanath, Supercond. Sci. Technol. **11** (1998) 420-425

Chapter 8: Investigations of The Zero Field ab Plane Conductivity of $YBa_2Cu_3O_{7-x}$

8.1 Introduction

Before superconductors can be used for many applications it will be necessary to fully understand and model the transport characteristics of these materials. Applications such as current leads, micro circuitry and fault current limiters all demand predictable responses to transport currents. In addition, the study of dissipation and flux flow characteristics gives us a direct way to build a more complete picture of the superconducting process itself. In this section the resistive transition and the I-V characteristics of single grain melt textured YBCO are studied at temperatures close to T_c and with the current in the ab direction.

At high temperatures (i.e. close to T_c) in layered superconductors such as YBCO the novel effect of spontaneously generated vortex/anti-vortex pairs dominates the electronic transport properties in zero magnetic field. If one supposes that due to the layered nature of the material and the small value of ξ the system is strictly 2 dimensional, then the vortices take the form of pancakes with no intralayer forces to be considered. This 2D system has been modeled by Kosterlitz-Thouless (KT)[1-3] and gives a power-law V(I) dependence:

$$V \alpha I^n \qquad \text{eq 8.1}$$

Obviously this model predicts a resistive transition for any non-zero current. Also, as Fig. 8.1 shows, a fixed value of n is predicted for each temperature, with a transition to n = 1 for any temperature larger than a characteristic temperature (T_{KT}).

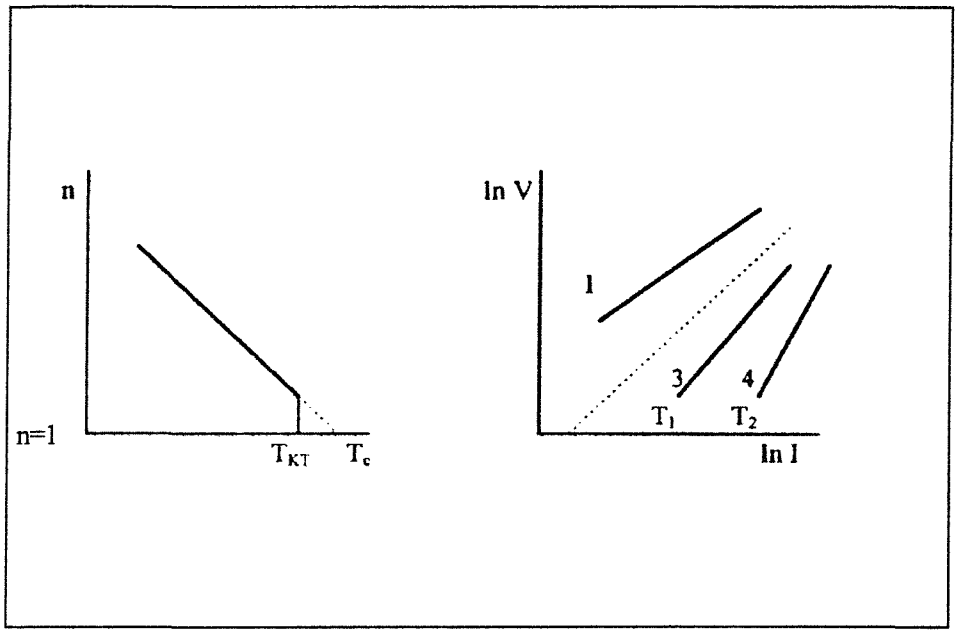

Fig. 8.1 - T phase diagram predicted by KT theory.

The KT theory has been generalized by Jensen and Minnhagen (JM)[4] so that a quasi 3D system may be considered. Their rationale is explained below.

$$E(r) = 2E_c + E_1\ln(r/\xi) + E_2(r/\xi) - s\phi_0 Jr \qquad \text{eq 8.2}$$
$$\quad (1) \qquad (2) \qquad (3) \qquad (4)$$

where (1) represents the creation energy of the vortex pair, (2) represents the attractive force active along the ab plane (the same as in the 2D case), (3) is the intralayer coupling term and (4) is the Lorentz force contribution which is trying to pull the vortices apart. In this notation E_1 is the interlayer coupling constant proportional to $1 - T/T_{c0}$, ξ is the coherence length in the ab plane, s is the distance between the superconducting $(CuO_2)_3$ planes, ϕ_0 is the flux quanta and J is the transport current. E_2 is the intralayer coupling constant and is given by:

$$E_2 = \pi E_1 \xi 2^{1/2} \lambda_j \qquad \text{eq 8.3}$$

where λ_j is the Josephson length. To find the distance at which it becomes energetically favorable for vortex pairs to separate (r_m) it is necessary to differentiate eq 8.2.

$$r_m = E_1/(sJ\phi_0 - E_2/\xi) \qquad \text{eq 8.4}$$

From this we may assume that only vortices created with a separation larger than this will move apart and induce losses. The energy of the barrier that has to be overcome for this to occur is given by:

$$E_b = E(R) - E_c \qquad \text{eq 8.5}$$

$$\Rightarrow E_b = E_1 \ln(E1/(sJ\phi_0 - E_2/\xi)) \qquad \text{eq 8.6}$$

By considering the classical model for escape over a barrier, in conjunction with the Bardeen-Stephen[5] model for flux flow resistance we can deduce a relationship for the rate of generation:

$$\Gamma_f = \exp(-E_b/k_BT) \qquad \text{eq 8.7}$$

$$\Rightarrow \Gamma_f \propto (E_1/(s\phi_0\xi J - E_2))\exp(-E_1/2k_BT) \qquad \text{eq 8.8}$$

The number density of unbound vortices (n_f) is determined by the balance between the rate of creation and the rate of annihilation i.e.:

$$d_f/dt = \Gamma_f - \text{constant} \times n_f^2 \qquad \text{eq 8.9}$$

In the steady state this will be equal to zero and so we may deduce that the rate of creation is proportional to the square of the number density. The flux flow resistance (R_f) is proportional to the number density, hence we may write

$$V = RfI \propto (E_1/(s\phi_0\xi J - E_2))^{-E_1/2k_B T} \qquad \text{eq 8.10}$$

$$\Rightarrow V \propto I(I - I_{c1})^d \qquad \text{eq 8.11}$$

where a is equal to $E_1/2k_BT$ and so is proportional to $1/T-1/T_{c0}$, and I_c corresponds to the critical current given by:

$$I_{c1} = E2/s\phi_0\xi = 2^{1/2}\pi ak_BT/\phi_0 s^2\gamma \qquad \text{eq 8.12}$$

where γ is the anisotropy factor ($\gamma = \lambda_j/s$). It should be noted that it has been shown experimentally[6] that for high currents I_{c1} is proportional to $1-T/T_c$, but for small currents the dependence is more complex. The resistive behavior for all currents can be seen in Fig 8.2, taken from Pierson et. al.[7].

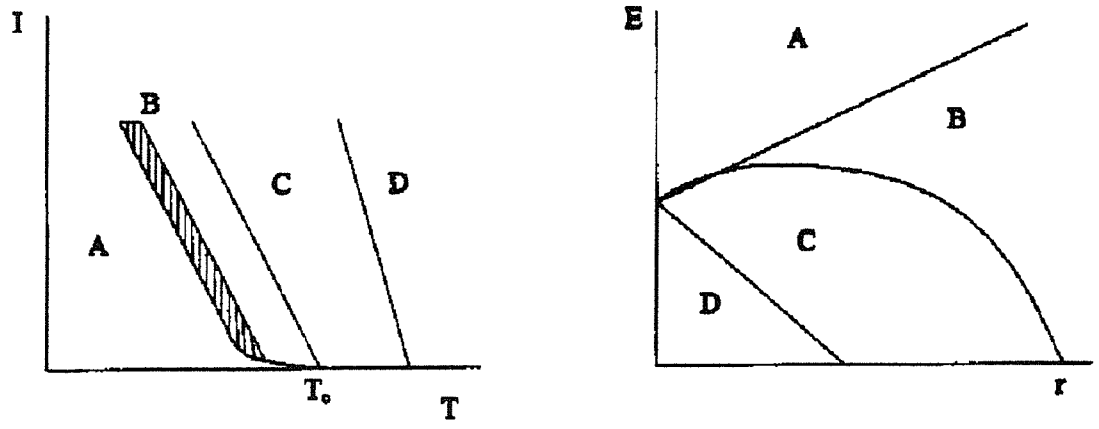

Fig. 8.2 I-T phase diagram for layered superconductors produced by Pierson[5]

The author obtained this phase diagram by performing a real space normalization group analysis on the vortices modeled as a gas of charges that interact via two-body interactions

and under the influence of the Lorentz force. Inset is a visual representation of the energy of the vortex pairs as a function of separation in the 3 different regimes. There are 3 characteristic currents identified in Fig 8.2; $I_{c1}(T)$ is the current value where the unbinding of the vortex pairs starts i.e. when the Lorentz force overcomes the Josephson coupling but not the logarithmic intralayer attraction, $I_c(T)$ is the true critical current where the phase transition occurs and the Lorentz force overcomes the intralayer attraction, and $I_{c2}(T)$ corresponds to the 3D-2D crossover which takes place at T_{KT}. For sufficiently large currents both $I_{c1}(T)$ and $I_c(T)$ are expected to decrease linearly with temperature, with the same slope. At small currents $I_{c1}(T)$ is expected to deviate from this relation and join with $I_c(T)$ at Tc. In region A the current is below I_{c1} and the IV characteristic equates to $V(I) \approx 0$. Region B is the segment of the phase diagram investigated in this work. The low current shaded region approximates to the area in which the JM model holds true before breaking down at higher currents. This breakdown may occur for two reasons, firstly the model is based on rare escapes over a barrier which is not the case at high currents and secondly at temperatures close to the transition the 3D nature of the system will allow current loop blowouts in the perpendicular direction to become significant. Regions C and D are mainly ohmic regions with small non-ohmic contributions addressed in ref[6].

In the following sections the low current density properties in the region approaching T_c are investigated. The R(T) transition and the I-V characteristics of single grain melt textured and de-twinned single crystal YBCO have been measured close to T_c in zero magnetic field for the voltage range of 10^{-9} to 10^{-6} V. The data was analyzed in terms of Pierson's I-T phase diagram detailed above and the region in which the Jensen-Minnhagen equation for the I-V holds true was determined. The JM theory was then used to model our data. In addition the dependence of I_{c1} on $t = 1 - T/T_c$ for $0.0004<t<0.0019$ was investigated.

8.2 Experimental

Single grain melt textured YBCO was prepared via a standard seeded peritectic growth process described more fully in chapter 2[7-11]. A powder mixture ($0.85YBa_2Cu_3O_x$ + $0.15Y_2BaCuO_5$) was pressed into a pellet using a cold uni-axial press. This was then sintered at 980^0C before melt processing in air in a vertical furnace configured so as to enforce a vertical and horizontal temperature gradient. A cold finger was used to provide additional cooling to the center of the pellet where a small single grain of $SmBa_2Cu_3O_x$ was placed to act as an orientated nucleation site for crystal growth. The thermal cycle involved heating the system to a temperature in excess of the peritectic temperature for a short time, before fast cooling to the peritectic region where nucleation is initiated. This followed by slow cooling during which the bulk of crystal formation takes place.

The melt textured pellet was then polished and, using a wafering diamond saw, divided into single grain samples suitable for transport measurements. Crystal orientation was obtained via optical microscopy. The sample was then uniformly oxygenated at 500^0C for 150hrs in flowing oxygen and polished down to suitable dimensions; $3\times1.64\times0.23$ mm^3, with the smallest dimension along the c-axis.

Current contacts were formed along the ends of the sample so as to provide a uniform current along the ab-plane. The contacts for the voltage leads were in the form of two parallel strips 1.37mm apart which were painted on the top surface using a silver epoxy. The contacts were annealed at 500^0C for one hour in a flowing oxygen atmosphere.

The R(T) and I-V measurements were performed with a SQUID pico-voltmeter using a conventional lock-in amplification technique. The probing current, parallel to the ab plane, was modulated with a double polarity square wave of frequency f_m = 68 Hz. The temperature dependence of the resistivity was obtained by cooling the sample at a constant

rate of 0.2 K/min. During the I-V measurements the temperature stability was around 1 mK.

8.3 Results and Discussion

The R(T) measurement performed on single grain melt textured YBCO can be seen in Fig. 8.3. The measurement was carried out using a transport current of 10 μA and revealed a mid-point transition temperature of 91.8 K and a resistive onset of 91.6 K.

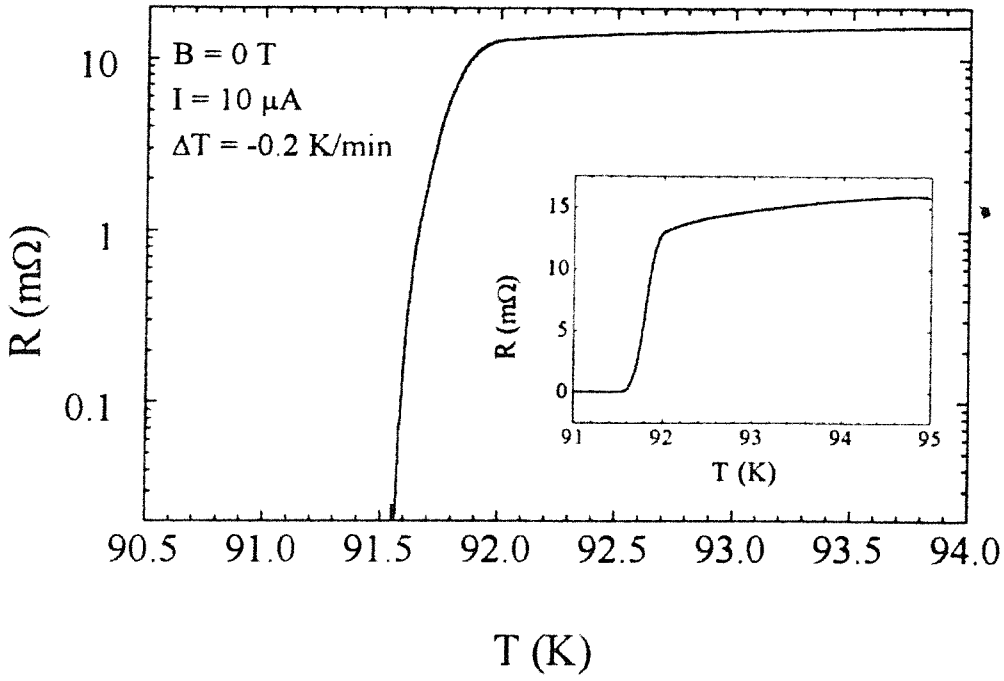

Fig. 8.3 The temperature dependence of the resistance of a single grain of melt textured YBCO (inset linear scale).

Shown in fig. 8.4 are the I-V characteristics of the same sample taken at temperatures close to Tc (91.44 K ≤ T ≤ 91.8 K). The data has been sampled at temperature intervals of

0.02K.

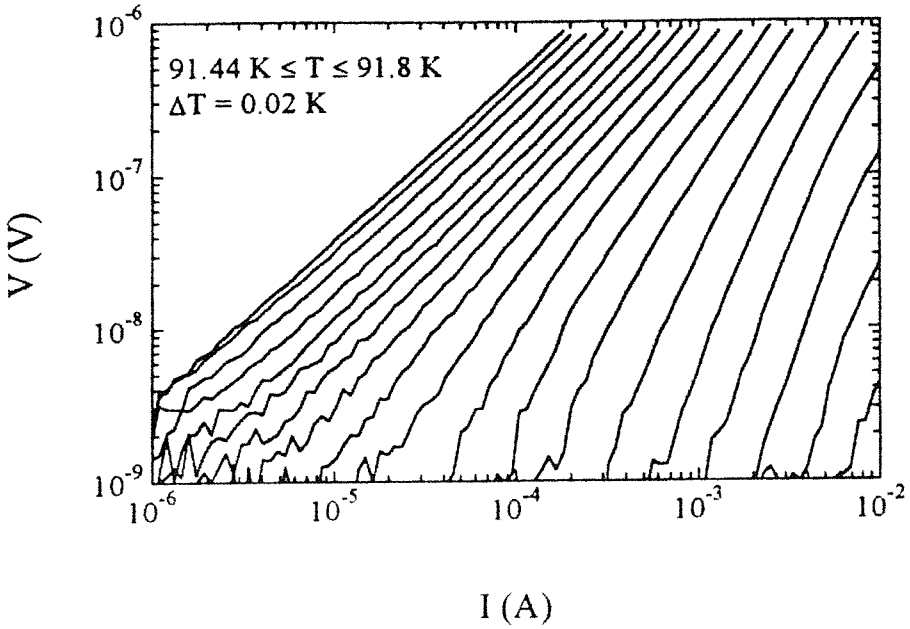

Fig.8.4 Current-voltage curves for single grain melt grown YBCO.

It is apparent from this figure that for T < 91.66 the I-V shows a linear dependence for high currents, whilst for lower currents a downward curvature is observed. As 91.66 K is approached the range over which the power law is valid increases, until 91.66 K is reached, and then an upward curvature is observed for T > 91.66K. It should be noted that the linear part of the curves does not have a gradient of 1. This non-ohmic behavior is discussed in ref[13].

The method used for data acquisition involved a logarithmic incrementation of current, therefore the results are to be interpreted using a transformed set of data. Because of this eq. 8.11 becomes,

$$\log(V) = c + \log(I) + (a-1)\log(I-I_{c1}) \qquad \text{eq 8.13}$$

where c is a temperature-dependent parameter, a is the temperature dependent J-M exponent. This translated data can be seen in fig. 8.5. The solid lines represent a fitting to eq. 13. The fit is good for the lower regions of the curves, but the at higher voltages there is considerable disagreement. As stated previously, the J-M equation is not expected to hold for all of the second region of the phase diagram seen in Fig.8.2. This has been explained in ref[13], and may be represented by introducing a current dependence into eq 8.13, making it:

$$V \propto I(I - F(T,I))^{a(t,I)-1} \qquad \text{eq 8.14}$$

In this regime, when $I \sim I_{c1}(T)$ then $F(T,I) \approx I_{c1}(T)$ and when $I >> I_{c1}(T)$ then $F(T,I) = 0$. This second condition means that for high currents eq. 14 becomes a power law dependence, identical to eq.1. The dashed lines in Fig. 8.5 illustrate the fitting of a power law dependence to the upper regions of the curves.

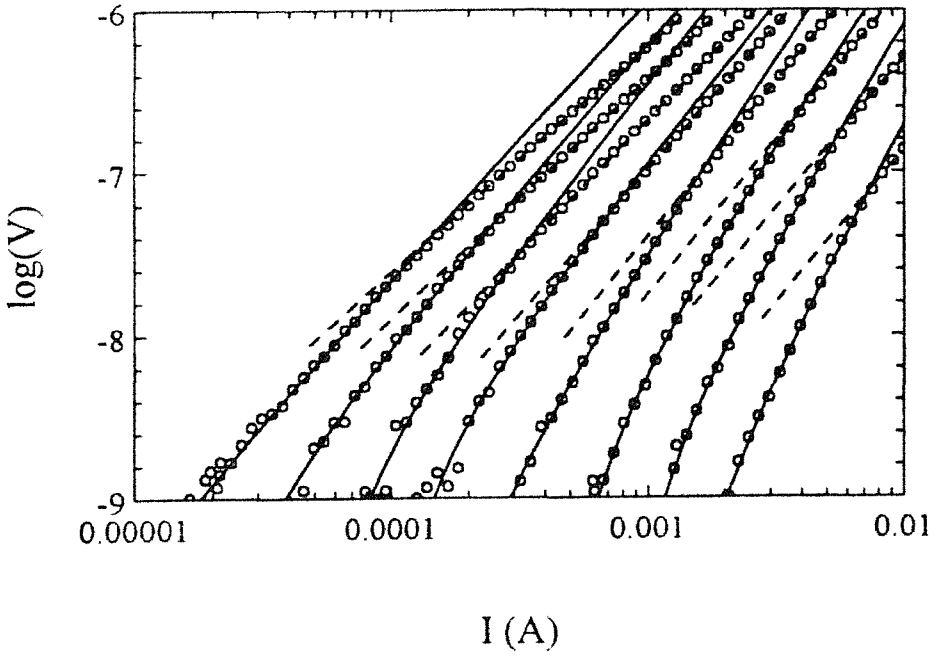

Fig.8.5 I-V data for melt grown YBCO transformed onto logarithmic axis. Temperatures

range from 91.48 K to 91.62 K in steps of 0.02K.

This analysis allows the determination of the temperature dependence of I_{c1}, the value of the J-M exponent and the slope of the power law region (both the JM exponent and the power law are shown in Fig. 8.6).

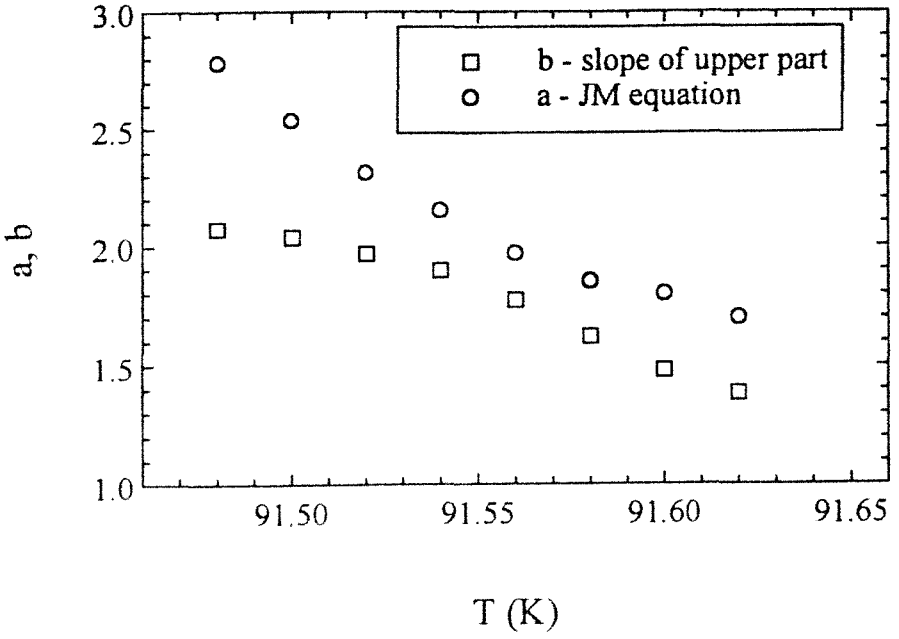

Fig. 8.6 J-M exponent and power law exponent values as a function of temperature.

In Fig.8.7, the temperature dependence of I_{c1} and the approximate characteristic current. I* (dashed line) at which dependence switches from eq 8.11 to eq 8.14, is presented. This figure is in fact a small region of the I-T phase diagram in which $I_{c1}(T)$ is non-linear for exponentially small currents, reaching zero at the same value, T_c, as $I_c(T)$. This region has yet to be theoretically addressed. Fitting this data very close to the critical temperature we found that I_{c1} can be related to (1 - T/Tc) thus:

$$I_{c1} \propto (1 - T/Tc)^{\mu} \qquad \text{eq 8.15}$$

with Tc equal to 91.66 and the exponent having the value $\mu = 3.5$. Unfortunately, the current limitation in our experiment did not allow us to determine the critical current $I_c(T)$ which separates the second and third regions of Fig. 8.2.

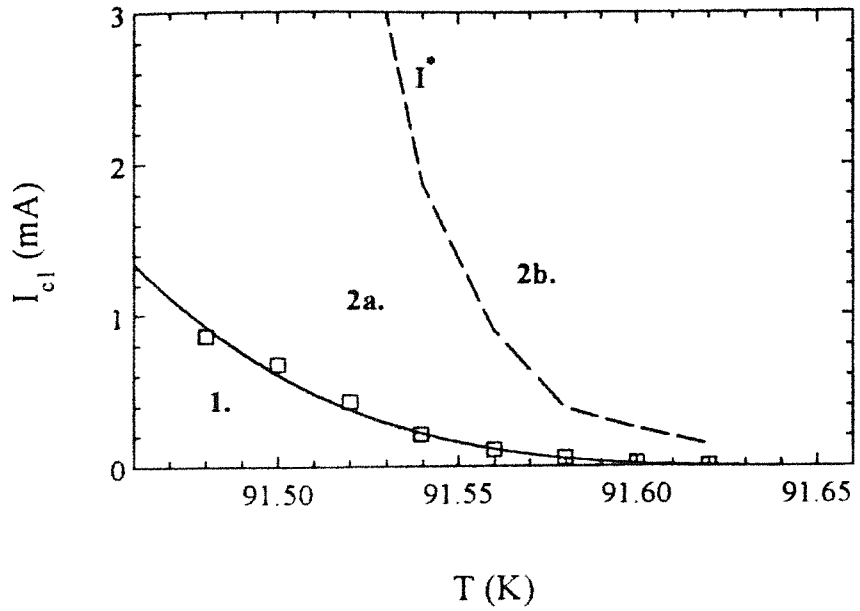

Fig. 8.7 Experimentally determined I-T phase diagram of melt tenured YBCO. Solid line is the fit of I_{c1} with eq 8.15 and the dashed line is marks the crossover between eq 8.11 and eq 8.14.

Identical measurements were carried out on a detwinned single crystal sample of YBCO, obtaining a similar phase diagram (see Fig. 8.8). The data agreed well despite differences in composition, morphology and pinning, giving $\mu \approx 3.7$ and a Tc of 93.94 K.

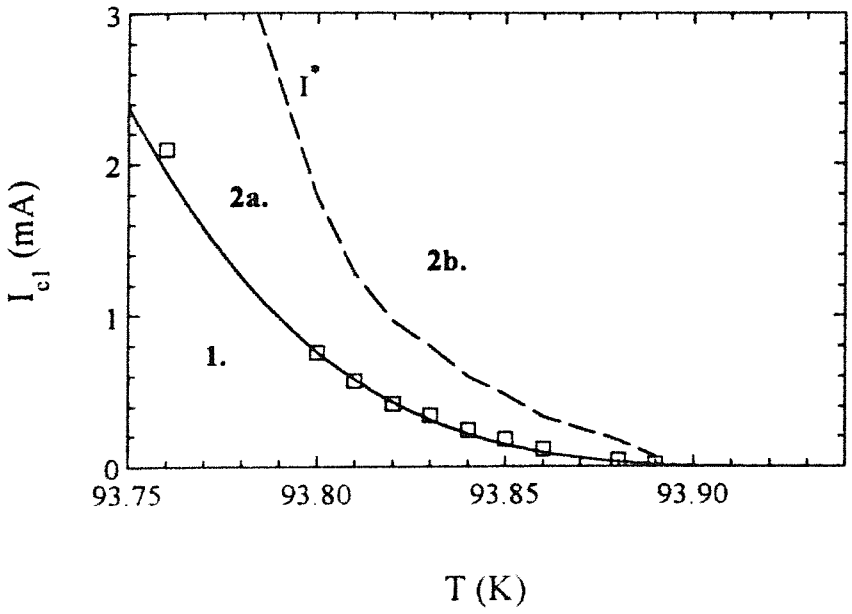

Fig. 8.8 The I-T phase diagram of a detwinned single crystal sample of YBCO. Solid Line represents I_{c1}, dashed line shows the approximate transition from eq. 8.11 to eq. 8.14.

8.4 Conclusions

Single grain melt textured samples of YBCO suitable for ab plane transport I-V measurements were prepared. R(T) and I-V dependencies close to Tc and in zero magnetic field were then obtained in the nV region. For T < Tc, the lower parts of the resulting curves were interpreted in the frame of the J-M model of current induced unbinding of thermally generated vortex/anti-vortex pairs, allowing us to obtain the temperature dependence of the characteristic current, $I_{c1}(T)$, close to Tc. In addition, the current value for a given temperature above which the J-M model becomes inadequate has been measured and interpreted as a cross over between the two sub regions in the phase diagram proposed by Pierson et al[13] For comparison, similar data was taken from a detwinned single crystal YBCO sample, which shows good agreement.

References

1. J.M. Kosterlitz and D. J. Thouless, *J. Phys. C: Solid State Phys.* **6** (1973)

2. L. N. Buleavski, M. Ledvij and V. G. Kogan, *Phys Rev B,* (1992)

3. V. L. Berezinski, *Zh. Eksp. Fiz.* **61**, 1144 (1971)

4. H. J. Jensen and P. Minnhagen, *Phys. Rev. Lett.* **66** (1991)

5. A. M. Kadin, K. Epstein and A. M. Golman, *Phys. Rev. B.* **27** (1983)

6. S. W. Pierson, *Phys Rev Lett,* **74** (1995)

7. M. Morita, S. Takebayashi, M. Tanaka, K. Kimura, K. Miyamoto and K. Sawano, *Adv. Supercond. Sci. Technol.* Vol. **3**, 733 (1991)

8. W. Lo, D. A. Cardwell, C. D. Dewhurst and S. -L. Dung, *J. Mater. Res.* Vol. **11**, 786 (1996)

9. S. Marinel, J. Wang, I. Monot, M. P. Delamare, J. Provost and G. Desgardin, *Supercond. Sci. Technol.* Vol. **10**, 147 (1997)

10. W. Lo, D. A. Cardwell, S. L. Dung and R. G. Barter, *J. Matter. Sci.* Vol. **30**, 3995 (1995)

11. D. Shi, D. Qu, S. Sagar and K. Lahiri, *Appl. Phys. Lett.* Vol. **70**, 3606 (1997)

12. R. L. Meng, L. Gao, P. Gautier Picard, D. Ramirez, Y.Y. Sun and C.W. Chu, *Physica C,* vol. **232**, 337 (1994)

13. S. W. Pierson, *Phys Rev B,* Vol. **55** (1997)

Chapter 9: Transport Properties of Single Grain Melt Textured YBCO in the Presence of an Applied Electromagnetic Field

9.1 Introduction

As the production of high quality bulk YBCO has become a reality the necessity of understanding the electronic properties of the bulk form of this material has become more urgent. It has been known for some time that the field dependence of J_c is affected greatly by the anisotropic nature of bulk YBCO. Calibrating the relationship between the angle of the applied field and the superconducting properties of the material will be essential for a large number of applications.

In this chapter the apparatus for observing the relationship between H_a and J_c, with respect to the elctronic properties of single grain bulk YBCO, are described and the measurements taken discussed.

9.2 Apparatus for Measuring Current – Voltage Curves in the Presence of an Applied Magnetic Field

Shown in Fig 9.1 is the design of the cryogenic high current lead assembly used to carry out transport measurements on bulk samples. As can be seen from this, the dewar has a very narrow lower section and a relatively small volume available for nitrogen storage due to the practical necessities of the magnet. This meant that the current leads and sample support arrangement had to fit into a tube of 17mm in diameter. Obviously, these leads had to be designed so as to balance out the effects of thermal conductivity against heat generation due to resistive losses, so that the amount of cryogen consumed could be minimised. In addition, it is essential that the sample holder is not able to move within the dewar, otherwise the angular dependence measurements would be affected.

The sample holder itself was designed so that either small substrates, for the measurement of small, brittle YBCO samples, or larger substrates, for use with longer less brittle BSCCO tapes may be attached. A Tufnol ring at the joint between the holder and the lead, in conjunction with a Tufnol "nose" section attached at the end of the holder, ensure both that the copper does not come into contact with the side of the dewar and that the holder is fixed in a central position within the dewar. Grooves in the nose section and flattened faces on the ring ensure that nitrogen is able to flow freely. A 2mm groove was machined along one side of the holder allowing voltage contacts to be taken from the sample to a piece of circuit board glued into the recess with G.E. varnish. Protected leads were taken from the circuit board to the top of the sample holder thus eliminating any chance of snagging the wires. This is a desirable configuration as not only is the possibility of accidental damage reduced but also, as the free lengths of wire are very short, hence the amount of electrical noise generated due to motion of wires in the presence of an electromagnetic field may be minimised.

Preliminary trials demonstrated that this arrangement was adequate, but for increased accuracy we found it necessary to ensure that all pairs of leads were formed from the same roll of wire, with the minimum possible number of junctions. This is because measurements at very low voltages are extremely prone to electrical noise arising from thermal e.m.f.'s, an effect which is magnified by compositional inconsistencies.

Another criterion considered during the design of this experimental rig was the necessity for accurate rotational positioning so as to facilitate angular dependence measurements. As can be seen in Fig.8.1, the dewar assembly is mounted above the electromagnet on a fixed aluminium plate. The body of the dewar is held in a brass collar, which is itself attached to a precision machined brass disk, the perimeter of which has 0.5° divisions engraved on it. This disk fits tightly into an aluminium ring bolted to the support plate, thus allowing accurate positioning of the dewar.

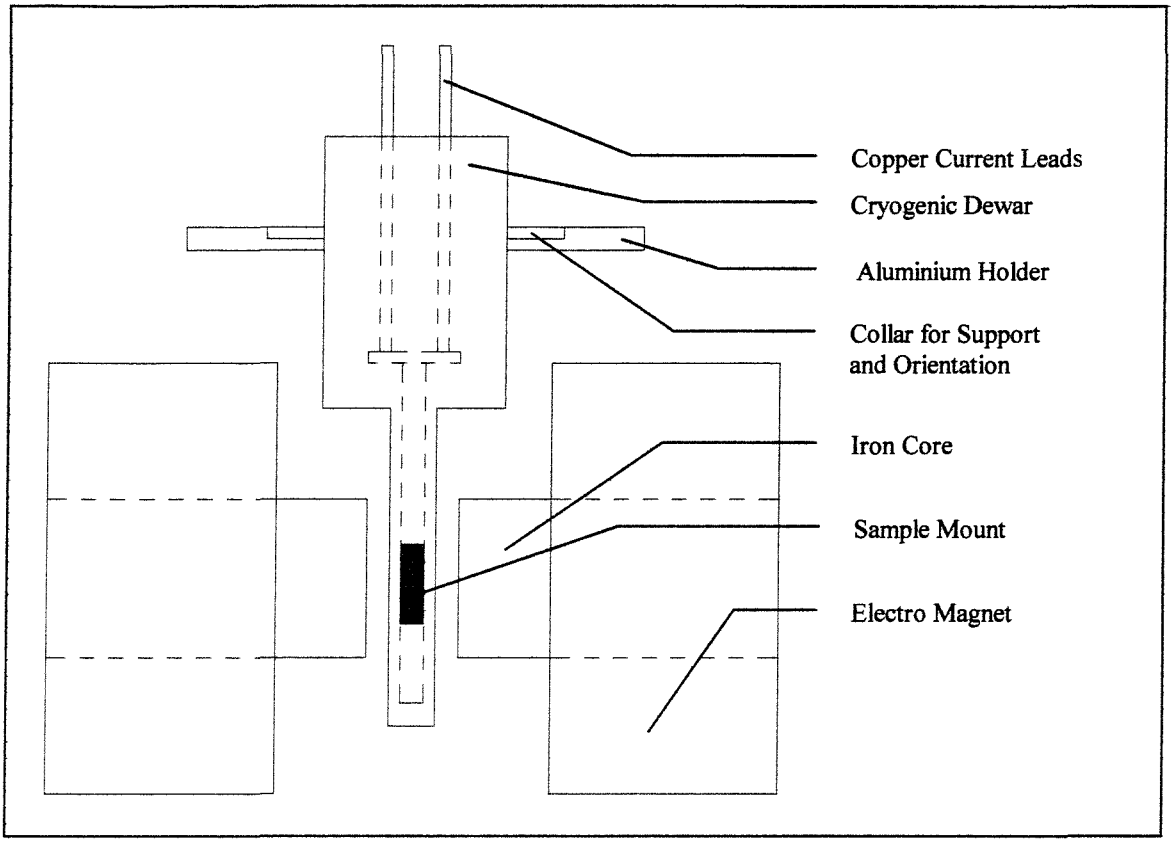

Fig 9.1 Schematic illustration of the experimental apparatus.

9.3 Sample Preparation

Single grain melt textured YBCO was prepared via a standard seeded peritectic growth process described more filly in chapter 2[1-5]. A powder mixture ($0.85YBa_2Cu_3Ox$ + $0.15Y_2BaCuO_5$) was pressed into a pellet using a cold uni-axial press. This was then sintered at 980^0C before melt processing in air in a vertical furnace configured so as to enforce a vertical and horizontal temperature gradient. A cold finger was used to provide additional cooling to the centre of the pellet where a small single grain of $SmBa_2Cu_3Ox$ was placed to act as an orientated nucleation site for crystal growth. The thermal cycle involved heating the system to a temperature in excess of the peritectic temperature for a short time, before fast cooling to the peritectic region where nucleation is initiated. This followed by slow cooling during which the bulk of crystal formation takes place.

9.4 High Density Current Injection Pads on Bulk YBCO

For direct transport measurements on high quality single domain YBCO it is necessary to inject large currents into a small area. Some of the samples measured here display critical currents in excess of 65000 Acm^{-2}, posing a considerable engineering problem with respect the magnitude and the method of injection of the probing current. It is for this reason that the samples examined are of such small dimensions, typically 1mm by 0.15mm in cross section. The length of the samples must also be limited as thermal stresses mechanical deformations will be exaggerated in long samples. An ideal solution to this problem would be to produce samples with wide end sections suitable for electrical contacts, which then narrow considerably, or "neck", to produce a region with a lower engineering critical current. However, YBCO is notoriously difficult to machine as it is an extremely brittle, layered ceramic. This problem is compounded by the thinness of the samples, which meant that in order for any machining or shaping to be attempted the samples first had to be mounted onto a support material. Experiments in this direction resulted in this approach being abandoned as the increased stresses on the shaped regions which occur during cooling caused the samples to crack, making them useless for measurements.

The two configurations used to make measurements can be seen in Fig 9.2. The first, a simple bar shape, is the easiest and safest to prepare. A wafering diamond saw is used to cut slices from a melt textured pellet. The wafer is then cut into strips which are the polished to the required thickness and then silver contact pads are sintered onto them. The second, a zig-zag geometry, has the advantage of producing samples with a greatly increased cross section available for current injection when compared to the cross section of the region in which the measurements are made. These samples are initially prepared in the same way as the plate samples. Once they have been polished to the correct thickness and the silver contacts sintered they are affixed to a substrate. The wafering saw is then used to cut slots into the material, forming the zig-zag geometry. This is a much more

intricate process and can result in the sample being broken during shaping or during cooling. However, a great deal more success has been achieved using this approach in comparison with the necking technique.

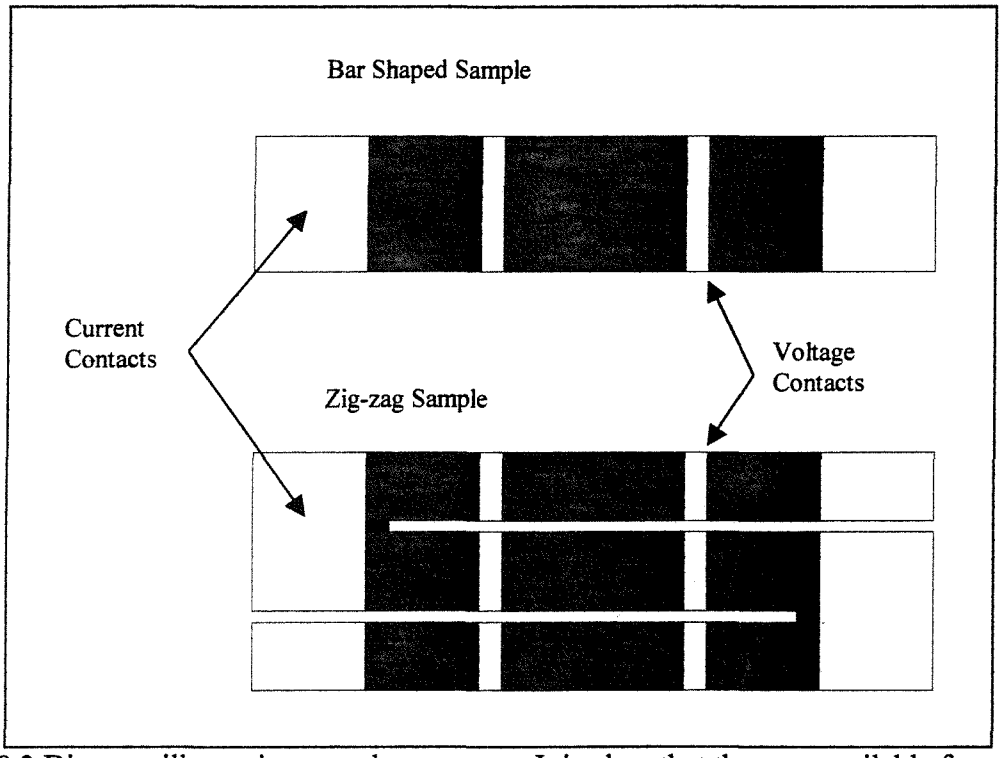

Fig 9.2 Diagram illustrating sample geometry. It is clear that the area available for current injection relative to the cross section of the sample where the voltage measurement is made is much larger for the zig-zag geometry.

The two main methods used to make contacts to high temperature superconductors such as YBCO are pressure contacts and soldered contacts. Pressure contacts were not a viable option for current injection as the required surface area for current transfer is extremely large due to the high currents involved and also because the samples are extremely delicate. Soldered contacts have the advantage of being a low resistance, non-stress inducing method of current injection. Silver was chosen as the material for the current and voltage pads. Silver is ideal for this purpose due to its high conductivity and its ease of soldering. Also, silver does not degrade the superconducting properties of YBCO as

many other metals do. Most importantly however, silver is able draw liquid phases from the material at temperatures well below the peritectic of YBCO and so form a sintered contact. This is important as a semi-conducting layer seems to form at the surface of YBCO, making most soldered contacts comparatively high resistance. Hence, using silver allows us to form an extremely low resistance contact which may then be soldered onto.

When sintering silver contacts it is vital that the particles of silver are extremely small. For this reason a paint consisting of a suspension of extremely fine silver particles in a binding agent is used. It is very important that the binder is of a type which will burn off completely during the sintering process and will not contaminate the material.

For this study it was essential that the contacts have extremely low resistances, hence the development of a successful sintering procedure was critical. The development of such a procedure revealed several important lessons.

It was quickly demonstrated that a good pad could not be formed from a single sinter. This was because, as a large volume of the paint is binder, there was a tendency for very little pain to be left on the sample after sintering. We tried to counteract this by painting a very thick layer of silver on before sintering. This was not successful as the paint would contract and peel away from the surface of the material, resulting in an extremely poor contact pad. Hence a procedure involving two stages of sintering was investigated. We found that sintering at low temperatures, i.e. around 500°C, gave unacceptably high contact resistances. Sintering at around 930°C produced pads that were very well sintered but extremely difficult to solder onto. This problem lead to contacts being lost during measurements and heating taking place at the copper - silver junction. The resolution of this problem arose from the combination of the two processes. The first sinter was carried out for 2 hours at 930°C, then the samples were cooled, another layer of paint was applied, and then they were sintered for a second time at 500°C. Using this method we were able to produce samples with contact resistances as low as 10^{-8} Ωcm^{-2}.

9.5 Sample Mounting

The substrate material used in this investigation was G.E. Fibre Glass. This material was chosen because its thermal contraction was very similar to that of bulk YBCO. It may be noted that the coefficient for the substrate is slightly larger than for YBCO. This is preferable to the reverse situation as YBCO is much stronger under compression than under extension.

Several methods of attaching the sample onto the substrate and attaching copper contacts to the sample were studied. As the samples are expected to carry currents in excess of 40000 Acm^{-2}, it is essential that the contacts between the copper current leads and the YBCO are carefully designed. If the copper contacts are too large then the greatly differing thermal contractions could cause the brittle YBCO to break. On the other hand, if the copper is not thick enough or the area of contact large enough then resistive heating could cause a quench in the superconductor resulting in its destruction. Another important factor to be considered is the method of affixing the contacts. During the soldering process it is imperative that no stresses are transferred to the YBCO. It is also vital that the sample should not be heated to any great extent as inhomogeneities in the oxygen annealing conditions or cracks resulting from differential thermal contraction could result.

It is for the above reasons that the following procedure was carried out when making copper YBCO contacts. Firstly the YBCO sample is adhered to the substrate using eco-bond epoxy resin. By carrying this out first we reduce the risk of the sample being damaged. Next, copper pads are bonded to the substrate on either side of the sample. These pads are positioned alongside the silver current injection pads and are slightly thicker than the sample. Braided current leads are soldered using high temperature solder onto the ends of these pads. The other end of the pads is tinned with low temperature

solder. A small copper bridge can then be soldered at low temperature between the copper and the YBCO with no mechanical stresses and relatively little heating. The bridge is itself tinned with low temperature solder which forms a low resistance contact with the silver.

Contacts for voltage measurements were made either by directly low temperature soldering copper wires onto the silver voltage pads or by stretching copper wire across the voltage pads and painting silver over them. The first method produces low resistance, low noise contacts, but the soldering process can destroy the pad and the contact degrades with time. The second method produces reliable, easy contacts which are slightly more noisy.

9.6 Data Aquisition

A P.C. operating lab view software was used to control a Hewlet Packard current source and to collect voltage measurements form a nano-volt meter. Lab view allowed the automated acquisition of I-V curves whilst the angle of the applied field could be adjusted manually by rotating the dewar within it's aluminium collar.

9.7 Experimental Results

Shown in Fig.9.3 is a plot of current against angle using a voltage criteria of $2\mu Vcm^{-1}$ in a magnetic field of 0.45T taken from an intermediate quality sample. There are four peaks visible in this plot. The highest, at 238°, corresponds to the intrinsic pinning and is observed when the applied magnetic field is parallel to the ab plane. This kind of pinning arises when the flux vortices are held by the pinning potential found between the crystal layers along the c axis. This phenomenon results from the c axis interalayer spacings in YBCO being only around twice the size of the coherence length of the material, which

causes the order parameter between the layers to become sufficiently depressed and to act as a pinning site[6].

Two further peaks may be observed as shoulders to this first peak. Measurements were taken at 0.5° intervals in this region so that this phenomenon could be examined more closely. When H_a is parallel to the ab plane, the flux lines can kink and become locked in to the layered structure[7]. As the sample is rotated away from the angle of the field being parallel to the ab plane the fluxons will remain locked in the potential well present between the superconducting layers. Thus a restoring torque will result which apposes the rotation of the vortices. This will effectively reduce the pinning potential between the layers, encouraging flux motion and causing the sharp drop in J_c observed in the figure. The shoulders on either side of the peak indicate the angle at which the vortices are no longer locked between the layers hence the effect of the restoring torque and field concenteation has been reduced.

The value of J_c tails off from the two secondary peaks as this kinking becomes less pronounced and the component of the Lorentz force in the c direction becomes smaller.

The smallest peak, observed at 90° degrees away from the highest, corresponds to the in-plane pinning mechanisms such as twin boundaries[8-12]. Twin boundaries provide planar pinning sites which attract flux lines and prevent motion in the ab plane. At H_a perpendicular to the ab plane the flux lines will be locked between the planes. As the angle is rotated towards H_a the flux lines will kink and zig-zag through the lower energy twin regions. At larger angles the effect of the twins will be lost and the flux line distribution will be collinear[13].

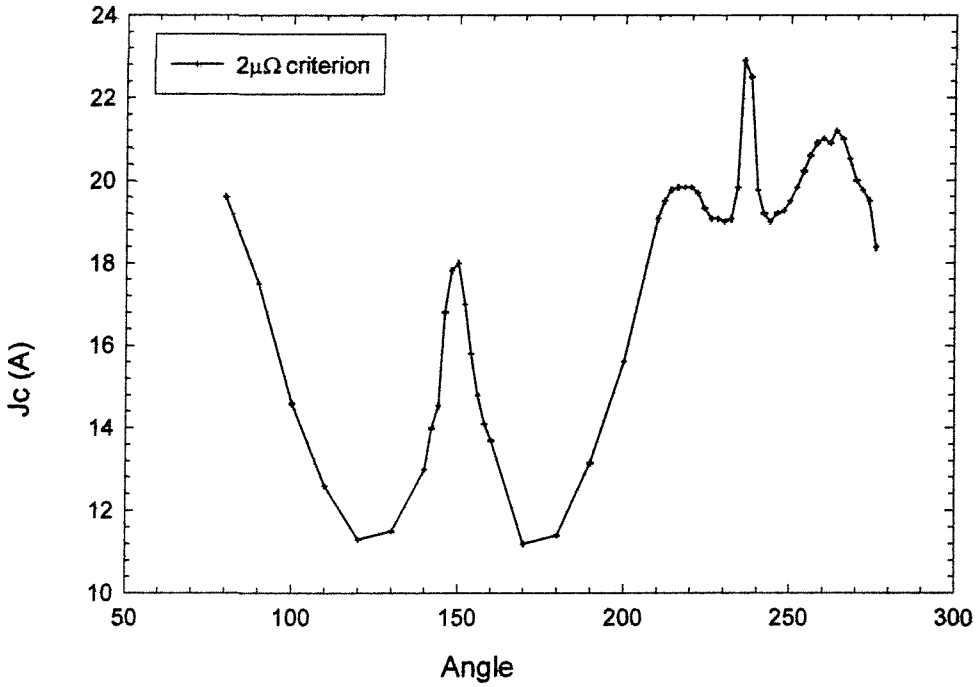

Fig 9.3 Angular dependence of Jc with a 2μV criterion in single grain YBCO in the presence of a 0.45T magnetic field (Sample 1).

Shown in Fig 9.4 is the voltage - angle dependence for a given current. Examination reveals that this figure illustrates the same properties as those seen in Fig 9.3 i.e. there is a reduction in the voltage measured at a given current when the angle of the applied magnetic field is parallel to the ab plane (230°) and when the field is parallel to the c axis (320°), both of which imply enhanced pinning. Another similar plot can be seen in Fig 9.5. In this instance the sample in question was of slightly higher quality, so measurements were taken with an applied magnetic field of 1.2T as apposed to 0.45T for the results presented in Fig 9.4. In Fig. 9.5, the extreme dip measured at 50° appears when the field is parallel with the ab plane. In this measurement the sharp increase in voltage between the peak and the shoulder features is extreme, implying that the torque effect becomes more important at higher fields or is more pronounced in higher quality samples or a combination of both. The in plane pinning characteristics however do not appear to have changed greatly.

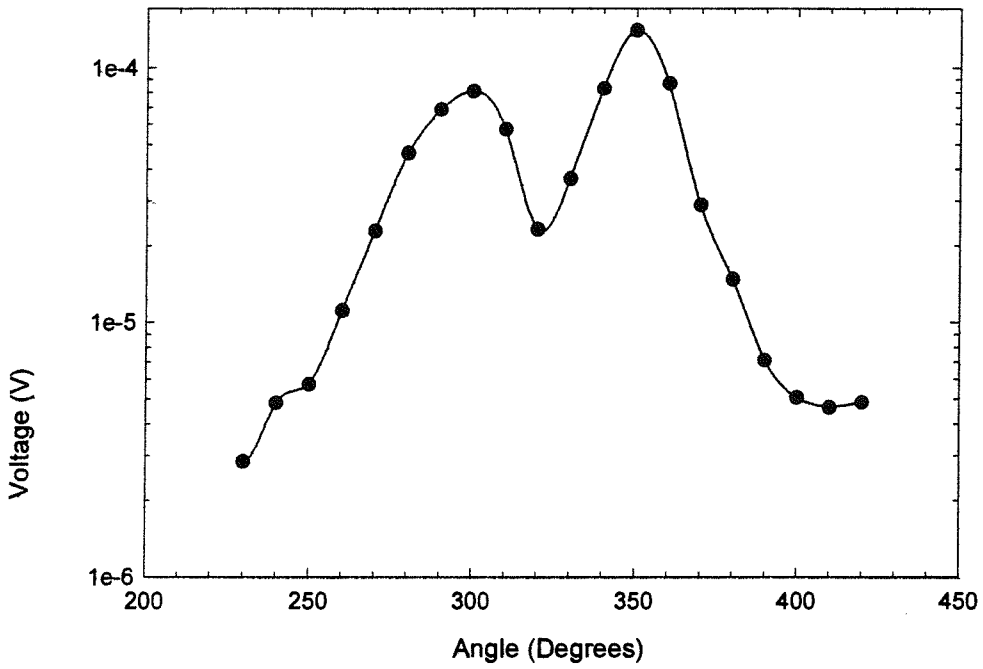

Fig 9.4 Voltage - angle plot of sample at 77K in an applied magnetic field of 0.45T.

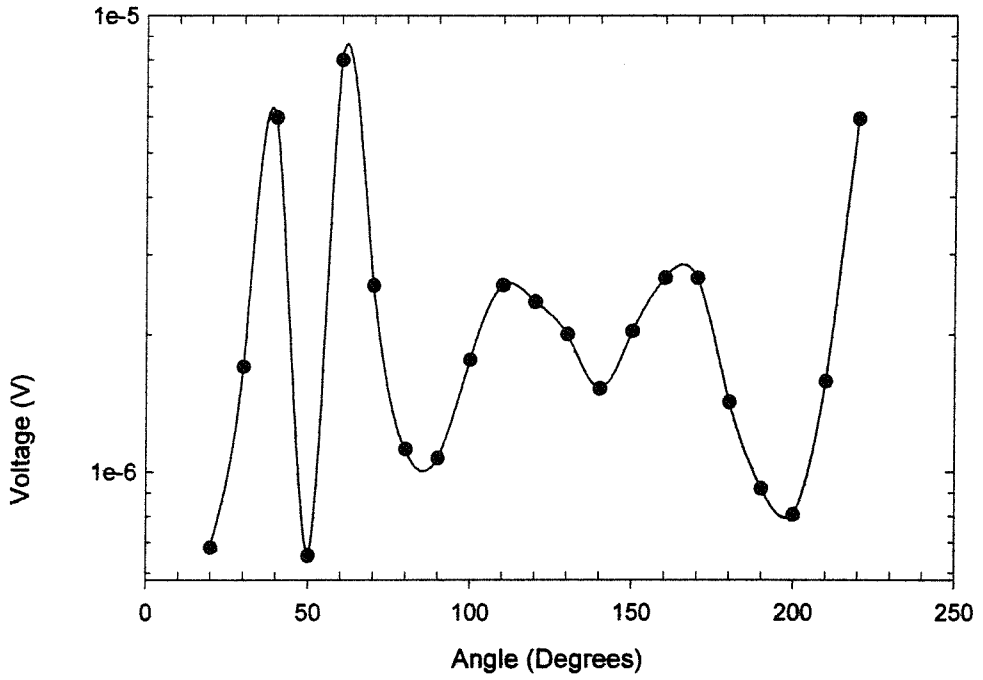

Fig 9.5 Voltage - angle plot for sample at 77K in an applied magnetic field of 1.2T

In order to investigate this behaviour further a large number of voltage – angle measurements were taken for a range of fixed currents. Fig 9.6 and 9.8 reproduce the data collected in the form of polar plots. Again, the samples used were of differing quality, with Fig 9.8 showing the data for the higher quality sample gathered at a higher field.

It is apparent from Fig 9.6 that the lower quality sample does not exhibit clearly the characteristic shoulders seen so clearly in Fig 9.3. However, the lowest current reading shows an increase in measured voltage at the point where one would expect the lowest voltage to be measured. This would imply that there is a very narrow peak and shoulder effect which has not been picked up due to the angular resolution of this plot (10°). It is interesting to note that as the value of the fixed current is increased, the effect of the intrinsic pinning becomes less significant where as the in-plane pinning mechanisms are not greatly affected. It can be seen from Current – Voltage measurements (shown in Fig 9.7) that the I-V curves taken to illustrate this diverge considerably. This is a strong indication of differing pinning mechanisms.

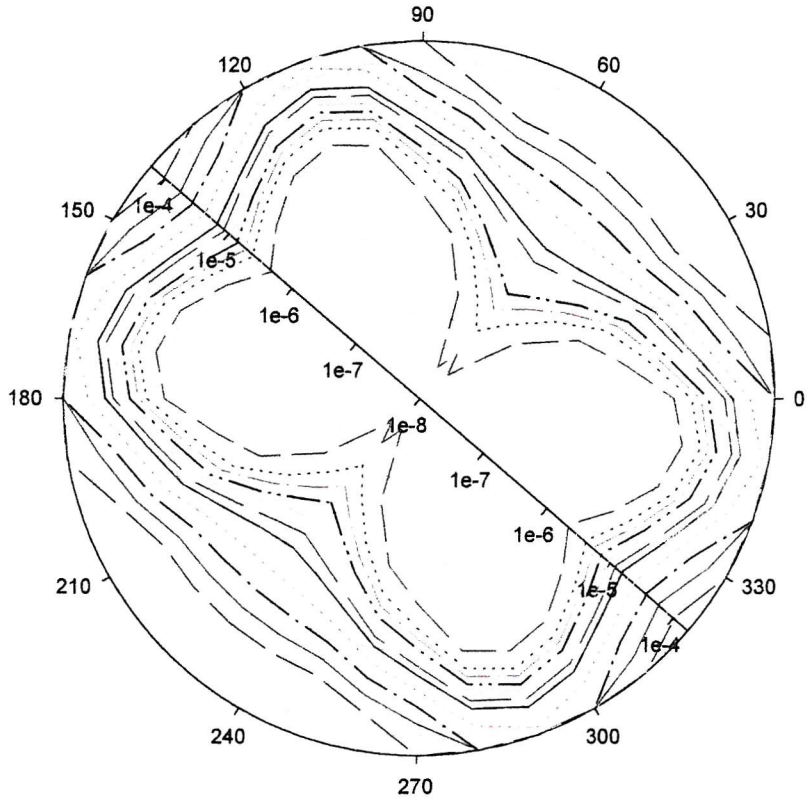

Fig 9.6 An iso-current polar plot illustrating variation in measured voltage with angle of applied magnetic field (0.45 T) for a range of currents (20 –50 Amps)

The material measured in Fig 9.8 clearly displays the peak-shoulder characteristic. As with the previous example, the relationship between applied current and measured voltage varies with the angle of applied field. The I-V curves reproduced in Fig. 9.9 clearly illustrates this. The relationship between current and voltage is of the type:

$$V \propto I^n \qquad \text{eq 9.1}$$

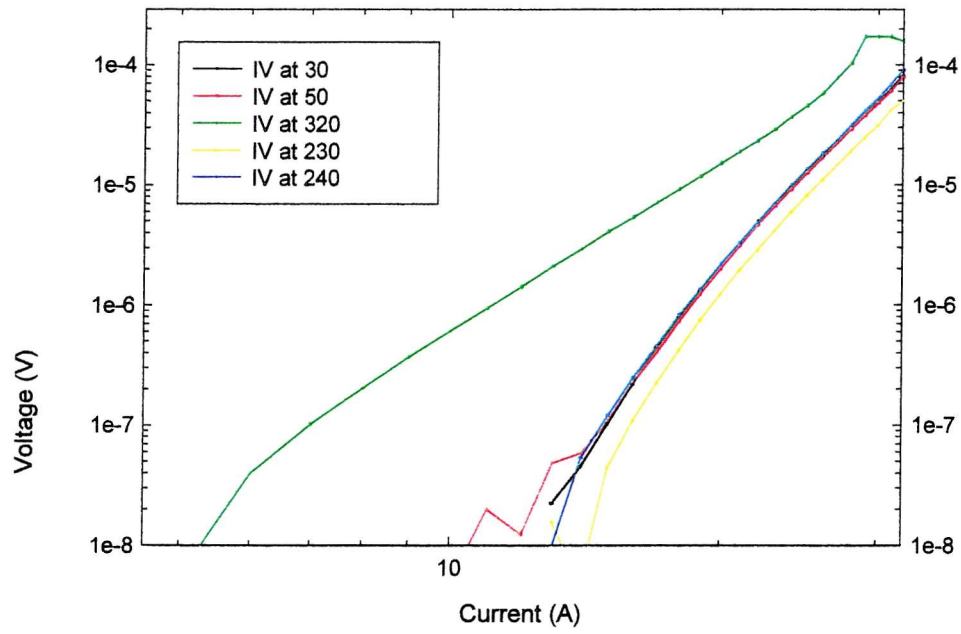

Fig 9.7 IV Curves illustrating the divergence resulting from differing pinning mechanisms.

It can be seen from Fig 9.9 that the measurements taken when the applied magnetic field is close to parallel to the ab plane show that the value of n remains constant whilst the value of J_c is highly angular dependent. Measurements taken when the applied field is perpendicular to the ab plane indicate that the value of n differs greatly from the parallel value and the angular dependence of J_c is less critical.

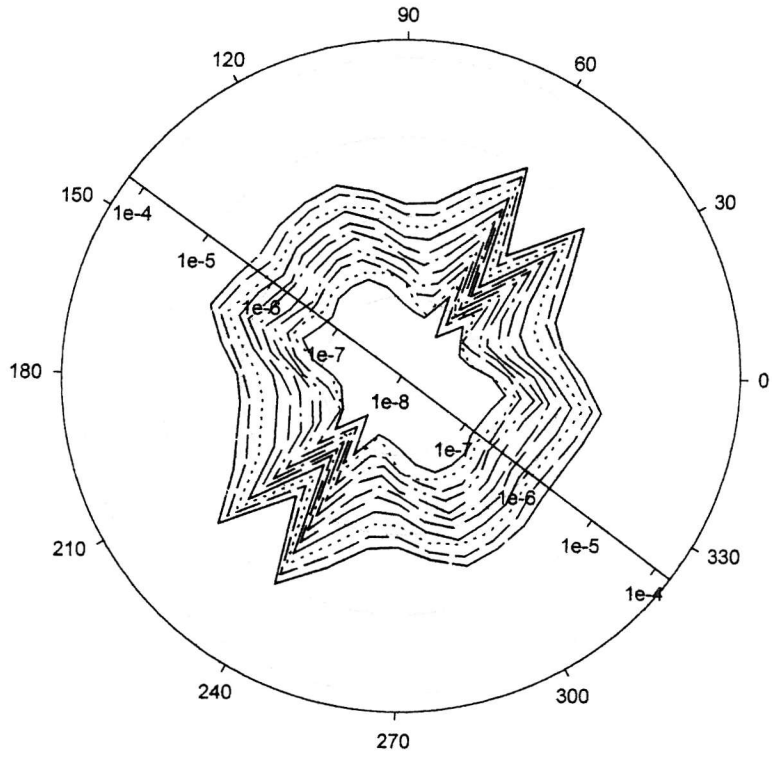

9.8 An iso-current polar plot illustrating variation in measured voltage with angle of applied magnetic field (0.45 T) for a range of currents (25 – 50 A)

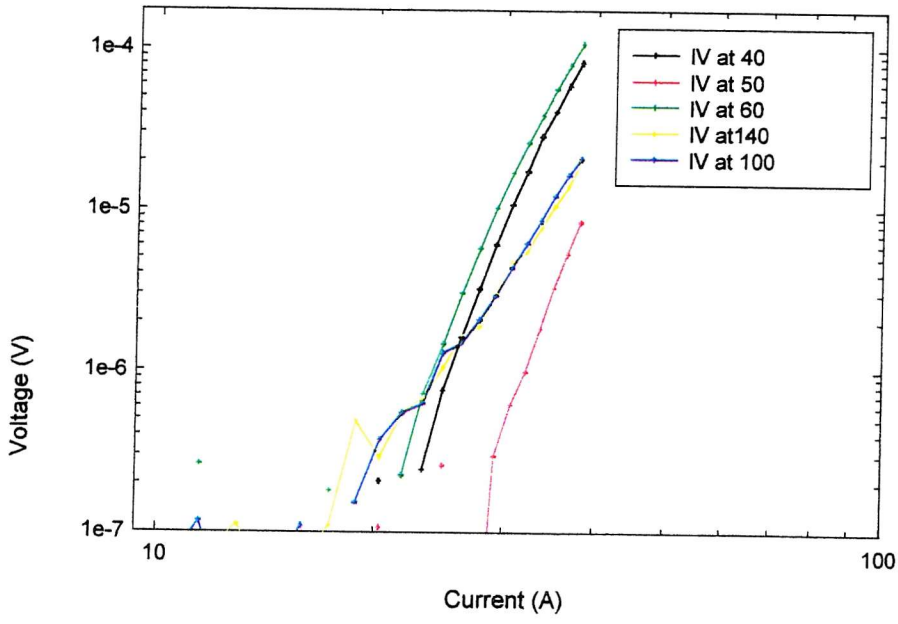

Fig 9.9 IV curves illustrating the cross over between the differing pinning mechanisms.

It is interesting to note that the sample with the highest value of J_c (80000 Acm^{-2} at 0.45 T using the $1\mu cm^{-1}$ criterion) shows very little difference between the I-V curves when the applied field is parallel or perpendicular to the ab plane. In fact, the IV curve with the best response is that taken with the field perpendicular to the ab plane. This is illustrated in Fig 9.10, which presents the IV curves for a wide range of angles. Fig. 9.11 is a "close up " of the region where H_a is close to parallel to the ab plane and clearly demonstrates the way in which the IV shifts to left without n changing appreciably.

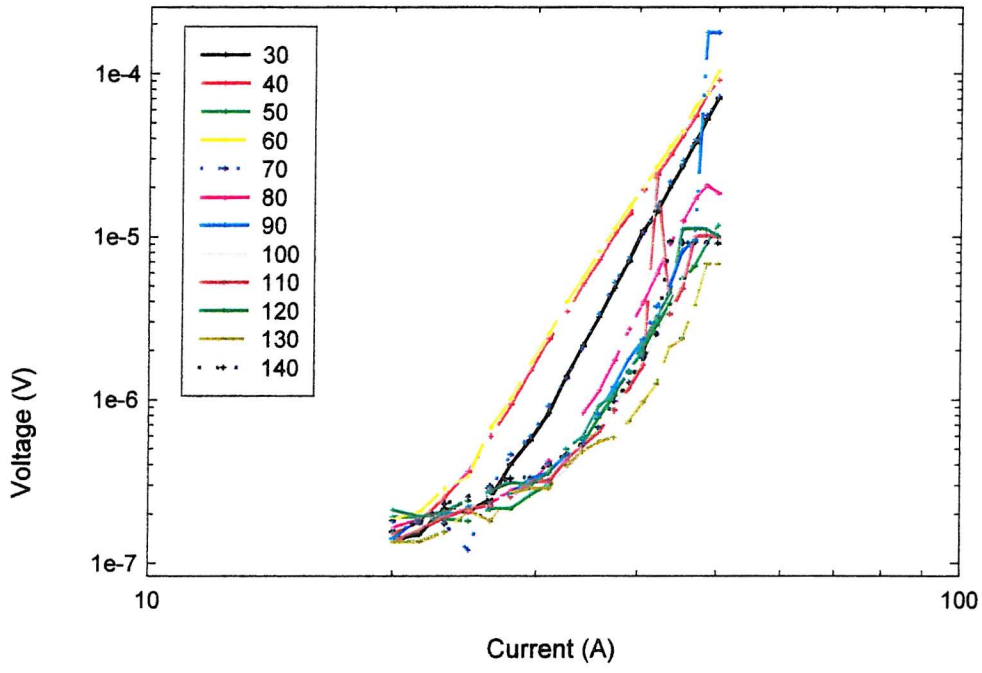

Fig 9.10 IV of high J_c sample for a wide range of angles in a field of 1.2T

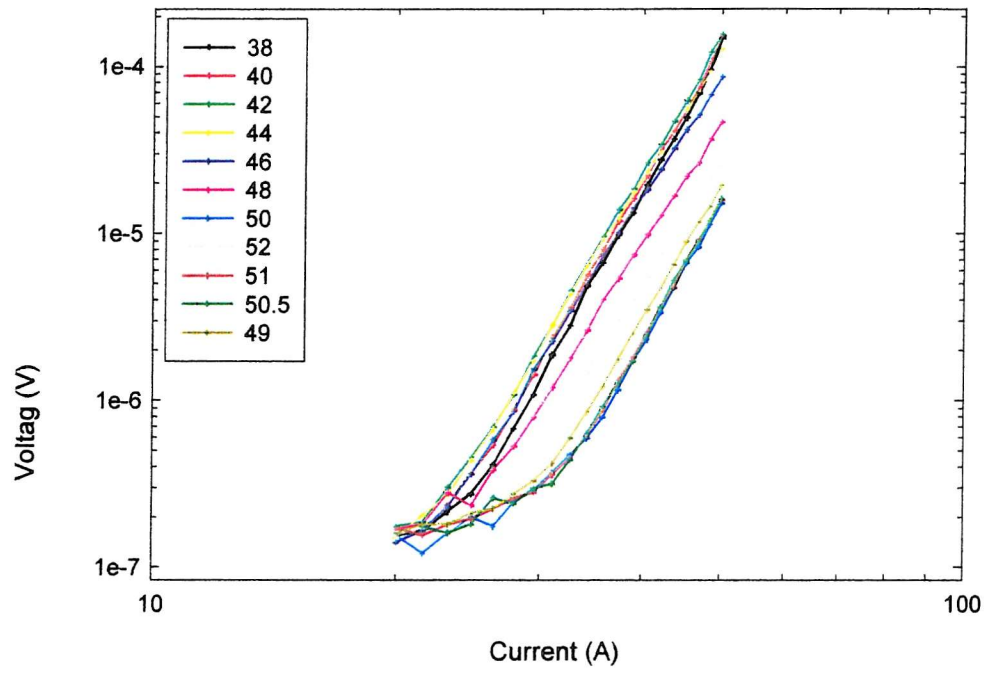

Fig 9.11 Close up of the H_a || ab region in Fig 9.11.

The high Jc and unusually high in plane pinning observed in this sample has been attributed to the atypical microstructure of this sample. This sample appeared particularly dense when polished and examined. More uniquely however, the sample displayed an unusual twinning structure not previously observed in this study. This is illustrated in Fig 9.12. The light and dark regions in this picture correspond to regions of unidirectional twinning. A similar effect has been observed in Nd123[14,15] and has been attributed to the stresses caused by Nd422 inclusions during processing/oxygenation. This feature would seem to enhance the in plane pinning properties of the material considerably but is not normally observed in bulk YBCO. It is possible that Y211 inclusions only have this effect on particularly dense samples.

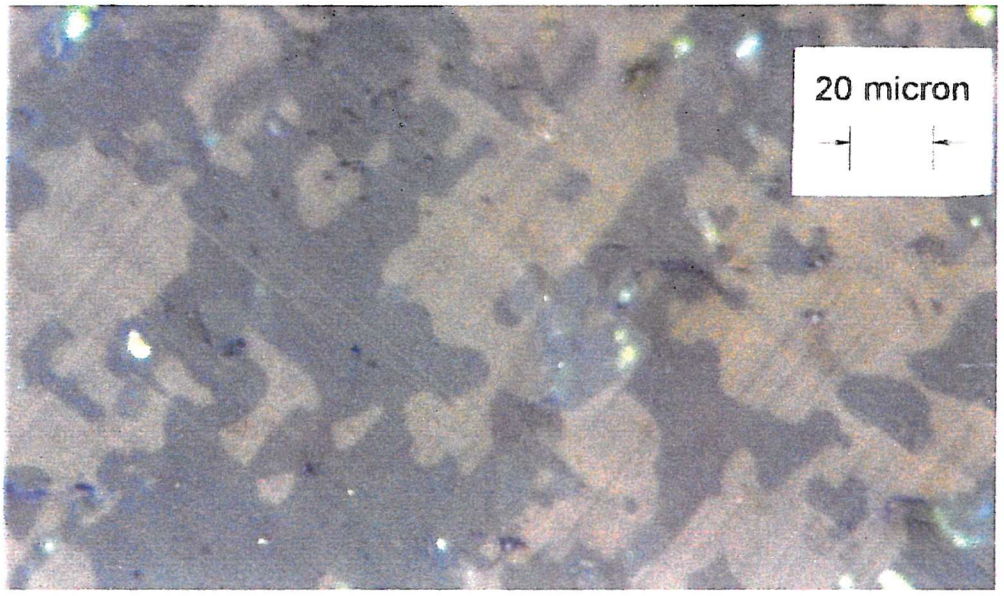

Fig 9.12 Twin structure in MTG bulk YBCO sample.

9.8 Conclusion

In this chapter a method for analysing the superconducting properties of bulk YBCO has been presented. This apparatus has then been used to gather information on the relationship between J_c and the angle of applied magnetic fields relative to the ab plane. Critical currents in the range of 80000 Acm^{-2} at 0.45T have been measured and an unusual in plane pinning feature examined.

9.9 References

1. M. Morita, S. Takebayashi, M. Tanaka, K. Kimura, K. Miyamoto and K. Sawano, *Adv. Supercond. Sci. Technol.* Vol. **3**, 733 (1991)

2. W. Lo, D. A. Cardwell, C. D. Dewhurst and S. -L. Dung, *J. Mater. Res.* Vol. **11**, 786 (1996)

3. S. Marinel, J. Wang, I. Monot, M. P. Delamare, J. Provost and G. Desgardin, *Supercond. Sci. Technol.* Vol. **10**, 147 (1997)

4. W. Lo, D. A. Cardwell, S. –L. Dung and R. G. Barter, *J. Matter. Sci.* Vol. **30**, 3995 (1995)

5. D. Shi, D. Qu, S. Sagar and K. Lahiri, *Appl. Phys. Lett.* Vol. **70**, 3606 (1997)

6. P. Chaddah and G. Ravi Kumar, *Phase Transition*, **19** (1989)

7. D. Feinberg and C. Villard, *Phy. Rev. Lett.* **65** (1993)

8 L. Ya Vinnikov, *Solid State Commun.* **67**, (1998)

9. C. A. Duran, *Nature* (London) **357**, (1989)

10. V. K. Vlasko-Vlasov, *Phys. Rev. Lett.*, **72** (1994)

11. H. Kupfer, *Phys. Rev.* **B 54** (1996)

12. A. A. Zhukov, *Phys. Rev.* **B 52** (1995)

13 A. A. Zhukov, G. K. Perkins, J. V. Thomas and A. D. Caplin, *Physical Review B*, Vol. **56**, No. 6 (1997)

14. M. Murikami, N. Sakai, T. Higuchi and S. I, Yoo, Supercond. Sci. Technol. **9** (1996) 1015-1032

15. P. Diko, H. Kojo, M. Murikami, *Physica C*, **276** (1997)

Chapter 10: Conclusion

10.1 Summary

Since the discovery of the Y123[1] there has been a great deal of activity centered on being able to meet the requirements of potential applications. In order to meet the requirements of industry, issues of size, shape and quality have to be addressed.

A large step was taken towards this goal when it first became possible to eliminate the grain boundary. As can be seen in Chapter 3, using the seeded melt textured growth technique[2] it is possible to produce large, single grain samples with a high degree of reproducibility. The scanning Hall probe data clearly illustrate the advantage of single grain material with respect to trapped field and free current circulation. Although it would seem possible to continually increase the size of the samples produced in this manner, it may be that there is an upper limit imposed by the slow rate of crystalisation and the rocking of the grain orientation which occurs at large distances away from the seed.

Microstructural enhancements to improve the critical current of the material via enhanced flux pinning were discussed in Chapters 4 and 5. The observations in Chapter 4 illustrate how it is possible to reduce the mean size of the Y211 inclusions within the bulk using a novel powder preparation technique involving a plasma spray to homogenize the starting materials. This is desirable as the critical current is inversely proportional to the size of the Y211[3] particles. Powder prepared in this manner produced YBCO with an extremely good microstructure, showing a fine, even distribution of Y211 inclusions within the Y123 bulk. It would be interesting should more powder of this type become available to produce samples suitable for magnet/I.V. measurements. In chapter 5, a new kind of pinning center is artificially introduced into the material by irradiation with thermal neutrons. The superconducting properties of the material were greatly enhanced, but the hoped for added pinning resulting from the fragmentation of the lithium dopant did not occur[4]. In fact, the effects of the lithium dopant were entirely negative.

Compositional improvements to Sm123 were examined in chapter 6. The superconducting properties of this material depend highly on the level of Sm/Ba substitution within the crystal[5]. In Chapter 6 it has been shown that the degree of substitution may be controlled by post processing after melt growth in a reduced oxygen atmosphere. Is these results could be carried forward with larger bulk samples the melt processing of Sm123 and Nd123 would be made much easier as a controlled atmosphere during growth would not be necessary.

In order to tackle the problem of sample size and shape from a different angle, a study into a method of joining sing grains of YBCO without a grain boundary was undertaken. The results of this, presented in Chapter 7, illustrate that by using a powder/liquid phase infiltration method it is possible to re-join severed single grain samples. The new material formed in the interface shows good alignment and a superior microstructure[6]. This kind of process could facilitate samples of any size/shape, increasing the possibility of practical applications enormously. Continuation of this work would ideally allow the production of large rejoined samples prepared from high quality YBCO bulk suitable for transport and magnetic measurements.

Chapters 8 and 9 concentrate on the characterization of the superconducting properties of YBCO. The data presented in Chapter 8 provides useful information on a fundamental level about the nature of flux pinning in the ab plane and allows comparisons to be drawn between measurements taken using single crystal samples. Chapter 9 focuses on the transport properties of melt textured YBCO at 77K and the dependence of this on the angle of applied magnetic field. These experiments reflect more closely the conditions expected in high current applications and raises issues on the problems of injecting large currents into bulk YBCO.

10.2 References

1. J. G. Bednorz and K. A. Muller, *Z. Phys.* B, **64**, 189-193 (1986)

2. M. Morita, S. Takebayashi, M. Tanaka, K. Kimura, K. Miyamoto and K. Sawano, *Adv. Supercond. Sci. Technol.* Vol. **3**, 733 (1991)

3. M. Murikami, S. Gooh, H. Fujimoto, K. Kamguchi, N. Koshizuka and S. Tanaka, *Supercond. Sci. Technol.*, **4** (1991)

4. S. J. Manton, C. Bedux, Y. Yang, K. Deligiannis, P.A.J. deGroot, *Mater. Sci. Eng.* B, **B53** (1998)

5. D. I. Grigorashev, E. A. Trofimenko, N. N. Oleynikov and Yu D Tretyakov, *IOP Publishing Ltd.* (1997)

6. S. J. Manton, C. Beduz and Y. Yang, *IEE Trans. Appl. Supercond.* Vol, **9** No. 2 (1999)